Paramagnetic defects in hydrogenated amorphous silicon: an advanced Electron Paramagnetic Resonance study

Im Fachbereich Physik der Freien Universität Berlin
zur Erlangung der Würde eines
Doktors der Naturwissenschaften (Dr. rer. nat.)
eingereichte Dissertation

vorgelegt von

Diplom-Physiker
Matthias Fehr
aus München

Institut für Experimentalphysik der Freien Universität Berlin
2011

Erstgutachter:	Prof. Dr. R. Bittl
Zweitgutachter:	Prof. Dr. B. Rech
Tag der Disputation:	11.04.2011

Summary

This thesis presents a detailed study of paramagnetic defects in hydrogenated amorphous silicon (a-Si:H). The defect states act as recombination centers for excess charge carriers and limit the efficiency of thin-film solar cells based on a-Si:H materials. The defect density drastically increases by light irradiation of the solar cell, which is a well-known degradation effect (Staebler Wronski effect - SWE). This effect is the major limitation of solar cells based on a-Si:H. In order to understand the process which leads to the generation of the defects states, detailed knowledge of the microscopic origin of the defect states is mandatory. In this work, the paramagnetic defects present after deposition (native defects) and after degradation with light (light-induced defects) are investigated with electron paramagnetic resonance (EPR). This technique measures the g-value of the defects and hyperfine interaction with magnetic nuclei in their vicinity and therefore allows to map out the wave function of the defects. Native defects in a-Si:H are localized coordination defects, which were attributed to threefold-coordinated silicon atoms (dangling bonds). A measurement of the EPR spectrum of native defects at various microwave frequencies (multifrequency EPR) is presented in this work and allows a precise determination of the g-values and the hyperfine interactions. The values obtained by the experiment are compared to theoretical density-functional theory calculations of dangling bonds to test if the microscopic origin of native coordination defects can be ascribed to dangling bonds. Defect states generated by light in the SWE are investigated by EPR measurements at high-field (Q-Band). Due to the increased resolution of these experiments, a new type of light-induced defect state could be observed, which exhibits different g-values and a faster primary-echo decay as compared to native coordination defects. In order to perform these advanced EPR experiments on fully-processed thin-film solar cells, electrically detected magnetic resonance (EDMR) is used with its superior sensitivity. A novel EDMR microwave pulse sequence is presented and tested on µc-Si:H solar cells to detect weak hyperfine interactions.

Zusammenfassung

Die vorliegende Arbeit ist eine detailierte Studie von paramagnetischen Defekten in hydrogenisiertem amorphen Silizium (a-Si:H). Die Defektzustände sind Rekombinationszentren für Überschussladungsträger und limitieren die Effizienz von a-Si:H Solarzellen. Die Defektdichte erhöht sich stark bei Bestrahlung der Solarzelle mit Licht durch einen bekannten Degradationseffekt (Staebler-Wronski Effekt - SWE). Dieser Effekt schränkt das Potential von a-Si:H Solarzellen stark ein. Um den Generationsprozess der Defekte besser zu verstehen ist eine Studie der mikroskopischen Struktur der Defekte unerlässlich. In der vorliegenden Arbeit werden die paramagnetischen Defekte nach der Materialdeposition (native Defekte) und nach Lichtdegradation (lichtinduzierte Defekte) mittels Elektronen-Paramagnetischer Resonanz (EPR) untersucht. Diese Technik misst den g-Wert und die Hyperfeinwechselwirkung magnetischer Nuklide in der Defektumgebung und erlaubt es die Defektwellenfunktion genau zu bestimmen. Native Defekte in a-Si:H sind lokalisierte Koordinationsdefekte, welche dreifach-koordinierten Siliziumatomen zu geordnet wurden („dangling bonds“). In dieser Arbeit wird eine Messung des EPR Spektrums nativer Defekte bei verschiedenen Mikrowellenfrequenzen präsentiert, welche es erlaubt die g-Werte und Hyperfeinwechselwirkungen präzise zu bestimmen. Die experimentellen Werte wurden mit Dichtefunktionaltheorie Rechnungen von „dangling bond“ Defekten verglichen um zu überprüfen ob die mikroskopische Struktur dieser Defekte tatsächlich „dangling bond“ Defekten zugeordnet werden kann. Lichtinduzierte Defekte des SWE wurden mittels Hochfeld-EPR (Q-Band) untersucht. Durch die erhöhte Auflösung dieser Experimente konnte gezeigt werden, dass lichtinduzierte Defekte andere g-Werte und einen schnelleren Echozerfall als native Koordinationsdefekte aufweisen. Um die entwickelten EPR Techniken auch auf Dünnschichtsolarzellen anzuwenden wurde elektrisch detektierte Magnetresonanz (EDMR) eingesetzt um die Empfindlichkeit zu steigern. Eine neuartige EDMR Mikrowellenpulssequenz wurde entwickelt und getestet an µc-Si:H Solarzellen um schwache Hyperfeinwechselwirkungen auszumessen.

Contents

1 Introduction

Direct conversion of solar radiation into electricity by the photovoltaic effect is one of the most promising technologies to maintain the energy supply of today's civilization and to contribute to the solution of global warming, air pollution and energy security problems on a renewable basis [1,2]. Photovoltaic power generation is based on solar panels, which are composed of a number of cells containing a semiconducting material. Although solar cells are superior to traditional power generation based on nuclear fission or fossil fuels in terms of environmental hazards and complexity [2], they constitute only a very minor share of today's global energy production (< 1 % in 2008) [3]. The main reason for this are the production costs and the moderate efficiency of the present technology [4]. In order to further improve the competitiveness of solar cells versus traditional energy sources, a further increase of the cell efficiencies and/or a reduction of manufacturing costs are mandatory.

The most important materials for current solar-cell mass production are various morphologies of silicon (among them: crystalline and amorphous), cadmium-telluride and copper indium selenide/sulfide [4]. Traditionally silicon solar cell are fabricated from mono- or multicrystalline materials and wafer-based crystalline silicon is still the dominating material on the market [4]. Major problems of this technology are the rather high fabrication costs and the energy required for the production of the wafers (about 50 % of the costs for a crystalline silicon solar cell are ascribed to the wafer substrate) [5]. These problems can be solved by using thin disordered films of silicon, which have a larger absorption coefficient due to the lack of k-conservation rule in the optical transition. In addition, thin silicon films can be deposited on inexpensive substrates (glass, stainless steel, etc.) to reduce fabrication costs below those of wafer-based silicon solar cells [6]. However, the major disadvantage of thin film silicon solar cells is their low efficiency [7]. The disordered nature of thin silicon films does not only improve the light absorption, but also induces localized defect centers in the band gap which act as recombination centers

or traps for excess charge-carriers. The effect of these centers to degrade the solar cell efficiency becomes even more pronounced upon irradiation of the cell with light. Staebler and Wronski were the first to discover that the photoconductivity of hydrogenated amorphous silicon (a-Si:H), which determines the efficiency of a-Si:H based solar cells, severely degrades by irradiation with intense light [8, 9]. This light-induced degradation effect is now notoriously known as the Staebler-Wronski effect (SWE). When taking no precautions in preventing the SWE, the magnitude of the light-induced degradation can be very large ($\approx$ 20 - 30 % of the initial cell efficiency) [10, 11]. The magnitude of the SWE can be reduced by using thinner absorption layer in a-Si:H pin solar cells (typically 300 nm) [12]. This, however, also reduces the amount of absorbed photons and limits the ultimate cell efficiency. In order to avoid loosing part of the incident light and at the same time limit the magnitude of the SWE, complicated tandem or even triple solar cells with several homo- and hetero junctions were developed. In view of these severe limitation that the SWE imposes upon the development of thin film silicon solar cells, a deeper understanding of this effect is clearly desirable. It is well-known that the SWE is a collection of several reversible changes in the a-Si:H material and the light-induced degradation of the solar cell efficiency cannot be traced back to a single origin [13]. However, the dominant effect of the degradation is a large increase in the concentration of paramagnetic localized gap states as discovered by electron-paramagnetic resonance (EPR) [14]. These states reduce the lifetime of excess charge carriers and thereby degrade the cell characteristics. There is considerable agreement in the research community that the atomistic structure of these paramagnetic defect states with $g = 2.0055$ are three-fold coordinated Si atoms, so called dangling-bonds (DBs). There is, however, no consensus in the community as far as the mechanism behind the generation of DBs by light is concerned. A number of well-developed theories are available in the literature, which propose different microscopic defect reactions leading to the reversible increase of the DB concentration. In order to test these theories experimentally, a mere measurement of the defect quantity and its energetic location in the band gap by, for example, sub-gap absorption measurements, photoconductivity spectroscopy or deep-level transient spectroscopy is not sufficient. More information on the microscopic nature of defects can be obtained by EPR. Important details that can be addressed by this technique are the de-

fect density, spatial defect distribution, defect wave function and correlations to impurity atoms such as hydrogen, phosphorous or boron.

This thesis presents a detailed experimental and theoretical study of the microscopic structure of the native and light-induced paramagnetic defect states in a-Si:H, which exhibit a well-known EPR spectrum centered at a g-value of $g = 2.0055$ [15]. Highly-developed pulse and c.w. EPR measurements were carried out to study details of the defect states to reveal their microscopic origin and to test available theories accounting for the generation of the defect states during the deposition process or by light soaking. The obtained EPR spectra were analyzed by advanced fitting routines, implemented in MATLAB® (The Mathworks, Natick, MA, USA). The experimental studies are combined with *ab-initio* density-functional theory (DFT) calculations to translate the experimentally obtained EPR parameters into a structural picture on the atomic level. The DFT calculations were performed by Christoph Freysoldt and Gernot Pfanner at the Max-Planck Institut für Eisenforschung in Düsseldorf (Germany). The results of the calculations were analyzed in detail in this thesis in order to compare them with experimental results. To investigate the hyperfine interactions of localized defect states in thin-film solar cells, a novel microwave pulse sequence was developed in this work to combine pulsed electrically detected magnetic resonance (EDMR) with electron-spin echo envelope modulation (ESEEM) techniques.

In the following a brief overview of the thesis structure and the content of the individual chapters is given:

Theory of EPR and EDMR The basics of EPR and EDMR which are necessary for an understanding of the experiments applied in this thesis are provided in chapter 2. The fundamentals of how the electronic structure of paramagnetic defects is linked to the observable EPR parameters, that is, the g-tensor and the hyperfine interactions, is presented. In addition, we give a detailed introduction on how the EPR parameters can be extracted from the measured EPR spectra by eye or by complicated fitting procedures. The fundamental theory of spin-dependent conductivity in semiconductors is discussed and theoretical expressions for pulse EDMR measurements are derived. In addition, a detailed theoretical treatment of the EDMR-ESEEM pulse sequence within the density matrix formalism is presented to provide the basis for a correct interpretation of the experimental results presented in chapter 6.

Materials and Methods Chapter 3 provides a short overview of the samples and the experimental methods applied in this thesis. Device-grade thin-film solar cells were fabricated at the Forschungszentrum Jülich and investigated by EDMR techniques. Since the sensitivity of EPR is not sufficient to directly probe defects in fully-processed solar cells, the a-Si:H layer were deposited on Al-foil which was subsequently etched away to obtain powder samples with a larger mass. The powder samples were investigated in different material states (as-deposited state, light-soaked state and thermally annealed state) to determine the microscopic properties of native and light-induced defect states. The samples are investigated by c.w. and pulse EPR techniques. The primary-echo pulse sequence was used to study the EPR spectrum and transversal relaxation properties of native and light-induced defects. ESEEM and Davies ENDOR pulse sequences were applied to measure the unresolved hyperfine interactions of the paramagnetic defects with magnetic nuclei in their environment.

The microscopic nature of native coordination defects in a-Si:H The microscopic nature of the dominant localized defect center in a-Si:H is of importance for a detailed understanding of the origin of these defects in the deposition process and during light soaking. Various theoretical models of the generation process of both native and light-induced defects rely upon the hypothesis that the defect centers are electronic states of threefold-coordinated Si atoms, so-called dangling bonds (DBs) [16–18]. This hypothesis was confirmed by EPR measurements of the hyperfine interaction of these centers with surrounding ^{29}Si nuclei in the host lattice [19]. In chapter 4, a detailed measurement of the EPR spectra at various microwave frequencies is presented, which allows a reliable determination of the EPR parameters of coordination defects in a-Si:H. The experimental results for the EPR parameters are then compared with DFT calculations of the parameters of various atomistic DB models. While there is a quantitative agreement for the g-tensor principal values between experiment and theory, the hyperfine interaction values deviate significantly. In the next chapter, the advanced EPR techniques, which were successfully applied to native coordination defects, are used study light-induced defects.

Structural differences between light-induced and native defects in a-Si:H It is commonly believed that the defect centers in as-deposited a-Si:H and light-soaked a-Si:H are identical [14]. This hypothesis is based on the observation that there is no

significant change of the EPR spectrum after light soaking. However, the present study revealed a variety of new results about the microscopic nature of defect centers in as-deposited a-Si:H. It is therefore mandatory to extend the investigations to light-induced defects to see if the newly employed experimental techniques are able to resolve yet undiscovered features of light-induced defects. In chapter 5, a detailed study of the EPR spectrum as determined by pulse EPR techniques at high field (Q-Band) is presented, which shows that the EPR spectrum indeed changes upon light soaking, that is, the light-induced defects exhibit a different EPR spectrum than native defects in as-deposited a-Si:H. It is most important to apply high-field EPR since the differences in the EPR spectra are small and not resolvable at lower microwave frequencies. In addition to a change in the EPR spectra a much more pronounced change in the transversal spin relaxation properties, as determined by a primary-echo pulse sequence, is observed. It is shown that light-induced defects exhibit a faster primary-echo decay at low temperature than native defects. The difference in the relaxation times enables one to disentangle the highly overlapping EPR spectra. A detailed analysis of the EPR spectrum of light-induced defects shows that the defects exhibit a slightly smaller g-value compared to native defects and a different, more symmetric, EPR line shape. In addition to the EPR spectrum, the anomalous primary-echo decay of light-induced defects is analyzed and possible microscopic processes inducing the echo decay are discussed.

Several models of the microscopic mechanism behind the light-induced generation of defects in a-Si:H rely on a hydrogen-mediated defect reaction [20]. The final metastable state of this defect reaction is a DB defect intimately correlated with a hydrogen atom (for a detailed discussion of the various SWE models refer to chapter 5). The nuclear spin of the hydrogen atom and the paramagnetic DB defect interact via the hyperfine interaction, an interaction which is conveniently determined by EPR techniques. Due to strong inhomogeneous broadening of the EPR resonance line shape, the determination of hyperfine interactions with hydrogen atoms requires Electron-spin echo envelope modulation (ESEEM) or Electron-nuclear double resonance (ENDOR) techniques [21]. A measurement of the hydrogen distribution around light-induced defects by ESEEM was attempted earlier [22]. In section 5.3, a detailed investigation of the hydrogen distribution around native and light-induced defects using ESEEM and ENDOR is presented.

Investigation of defects in thin-film silicon solar cells Despite the analytic power of EPR techniques to obtain microscopic information about paramagnetic defect centers in solar cell materials, the low sensitivity of the EPR technique makes it impossible to directly investigate thin-film silicon solar cells of device-grade, which commonly contain only a few paramagnetic defects. Hence, most EPR experiments are carried out on thicker films or on powder samples of the intrinsic absorber material. It is, however, unknown if the paramagnetic defects in films or powders are identical to those present in fully-processed solar cells. A convenient solution for this problem is the electrical detection of magnetic resonance (EDMR) by measuring changes in the dark- or photocurrent upon exposure to microwave irradiation. The sensitivity of this technique (10^4 spins/G) is orders of magnitudes larger than the sensitivity of conventional EPR (10^{12} spins/G) and is therefore applicable to solar cells. An additional advantage of EDMR is the selection of paramagnetic centers contributing the the final EDMR signal. In conventional EPR all paramagnetic centers contribute to the signal in an equal manner, while EDMR shows only those centers which are involved in charge-carrier transport or recombination pathways and therefore automatically selects those centers important for the electrical cell properties. However, the analytic power of EPR relies on the application of pulse techniques. In adapting pulse EPR experiments for the application in pulse EDMR experiments a number of experimental difficulties have to be overcome. Pulse EDMR techniques are therefore much less developed. It is especially desirable to develop a reliable pulse EDMR experiment similar to ESEEM or ENDOR techniques capable of detecting unresolved hyperfine interactions of defect states in solar cells. Chapter 6 presents a proof-of-principle implementation of a pulsed EDMR-ESEEM experiment applied to various defect states in a device-grade p-i-n µc-Si:H thin-film solar cell.

Conclusion and future work The final chapter of this thesis provides a detailed summary of the experimental and theoretical results about native and light-induced defects in a-Si:H as well as localized defect states in µc-Si:H thin-film solar cells and gives a conclusion about the obtained results in the light of the established theories of the SWE. Finally future experiments are discussed which can help to further investigate and clarify problems encountered in this work.

2 Theory of EPR and EDMR

The central point in this thesis is the analysis of the structure of paramagnetic defect states on a microscopic level. The microscopic structure includes the electronic structure, that is the spin-density or wave function of the electron occupying the defect state, and it includes the atomic structure, that is the arrangement of atoms (for example Si or H) of the defect and in its vicinity. The electronic and the atomic structure are tightly linked by the fundamentals of quantum mechanics. The electronic and atomic structure of the paramagnetic defect states are encoded in the gyromagnetic ratio - the g-value - and the hyperfine interactions of the unpaired electron. EPR is one of the few techniques capable of determining these values experimentally and can therefore provide a detailed picture of the defect state on a microscopic level. This chapter provides the theoretical basis to link the electronic and atomic structure of the defect to its EPR parameters and gives a detailed introduction on how these parameters can be determined from the experimental EPR spectra. The theoretical expressions are a necessary basis for the upcoming analysis of native and light-induced defects in a-Si:H described in chapter 4 and 5. In addition, the theoretical principles described here provide the basis for the understanding and interpretation of EDMR-ESEEM experiments, presented in chapter 6.

2.1 EPR of paramagnetic defects in a-Si:H

The unpaired electrons of paramagnetic defect centers studied in this thesis are S = 1/2 spin systems which are in most cases sufficiently dilute (defect density $N_s < 10^{18}$ cm^{-3}, average distance between two spins is > 100 Å) to treat each electron spin as isolated, that is, the different electron spins do not interact with each other. The spin of the electron will interact with an externally applied magnetic field $\boldsymbol{B}_0$ via the Zeeman interaction, which splits the degenerated ground state doublet into two ($m_S = \pm 1/2$)

levels (cf. Fig. 2.1). Considering the entire spin ensemble (typically $> 10^{12}$ defect centers) the populations of the two levels in thermal equilibrium is not equal and transitions can be induced by irradiation of the sample with electromagnetic radiation of the right frequency. EPR is therefore basically an absorption technique, which measures transition energies between different levels of a paramagnetic center. In addition to the external magnetic field, the presence of magnetic nuclei induces a shift of energy levels of the spin system by hyperfine interaction. In general, the energy states of the ground state of a paramagnetic center with an effective spin $S = 1/2$ and m nuclei with nuclear spins $I = 1/2$ are described by the static spin Hamiltonian [23]

$$\mathcal{H}_0 = \mathcal{H}_{\mathrm{EZ}} + \mathcal{H}_{\mathrm{HFI}} + \mathcal{H}_{\mathrm{NZ}} \tag{2.1}$$

where $\mathcal{H}_{\mathrm{EZ}}$ denotes the electron Zeeman interaction, $\mathcal{H}_{\mathrm{HFI}}$ denotes the hyperfine interaction between electron spin S and nuclear spins I and $\mathcal{H}_{\mathrm{NZ}}$ denotes the nuclear Zeeman interaction.

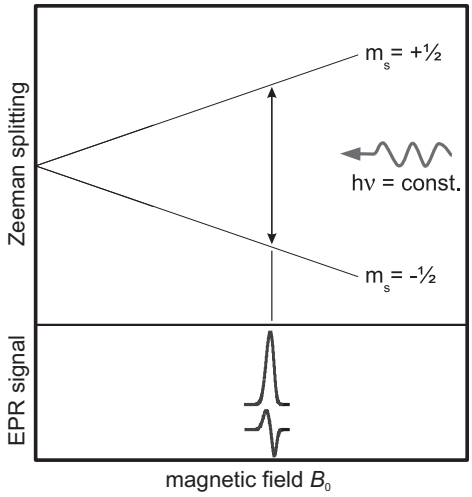

Figure 2.1: Splitting of the energy levels by the Zeeman interaction of the electron spin and the external magnetic field. upper part: Energy level diagram; lower part: Corresponding pulse (absorption) and c.w. (derivative) EPR spectra.

2.1.1 Electron Zeeman interaction

The interaction between electron spin and external magnetic field $\boldsymbol{B}_0$ expressed in an arbitrary coordinate system is given by the electron Zeeman term in the spin Hamiltonian

$$\mathcal{H}_{\mathrm{EZ}} = \mu_{\mathrm{B}} \boldsymbol{B}_0 \boldsymbol{g} \boldsymbol{S} / \hbar. \tag{2.2}$$

where μ_{B} is the Bohr magneton, the electron spin vector operator $\boldsymbol{S}$ and the orientation-dependent gyromagnetic ratio given by a 3x3 matrix, $\boldsymbol{g}$. Please note that a direct detection of the entries of this matrix is usually not possible and requires a special experimental setup [24]. What one rather observes in conventional EPR experiments is a symmetric second-rank tensor, the g-tensor, given by $\sqrt{\boldsymbol{g}\boldsymbol{g}^T}$. In order to avoid confusion, we will in the following only make use of the g-tensor for an interpretation of EPR spectra and denote this quantity by $\boldsymbol{g}$. The symmetric g-tensor can be characterized by three (real) tensor eigenvalues (g_x, g_y and g_z) and three Euler angles setting the orientation of the g-tensor principal axes in a molecular coordinate system. For cubic symmetry we find an isotropic g-tensor with $g_x = g_y = g_z$, for axial symmetry $g_x = g_y = g_{||}$ and $g_z = g_\perp$ and for rhombic symmetry $g_x \neq g_y \neq g_z$. Examples of EPR spectra for these three cases averaged over all possible orientations (powder pattern) are shown in Fig. 2.2.

For paramagnetic centers embedded in solids or organic systems, the orbital momentum of the unpaired electron is quenched ($\boldsymbol{L} = 0$). In this case, both the anisotropy of the g-tensor and shifts from the free-electron g-value $g_{\mathrm{e}} = 2.0023...$ arise from a mixture of the ground state and other excited states by the spin-orbit coupling

$$\mathcal{H} = \lambda \boldsymbol{L} \boldsymbol{S} \tag{2.3}$$

where λ is the spin-orbit coupling constant. Second-order perturbation treatment of the spin-orbit coupling and the external magnetic field gives [26]

$$g_{\alpha,\beta} = g_{\mathrm{e}} \delta_{\alpha\beta} + 2 \sum_{n \neq p} \frac{\langle \psi_p | \lambda L_\alpha | \psi_n \rangle \langle \psi_n | L_\beta | \psi_p \rangle}{\epsilon_p - \epsilon_n} \tag{2.4}$$

where ψ_p is the wave function of the ground state and ψ_n are the wave functions of the n^{th} excited state, with the corresponding energies ϵ_p and ϵ_n.

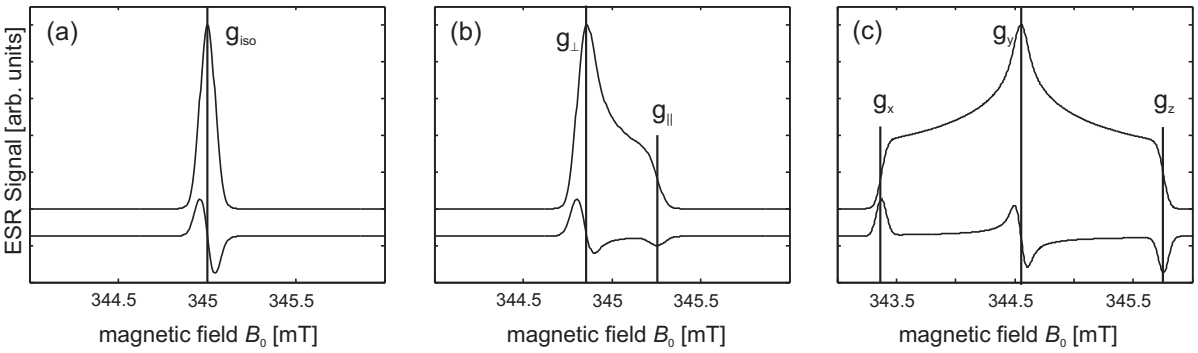

Figure 2.2: Simulation of EPR powder spectra for g-tensors of different symmetry. The EPR spectra are plotted as absorption lines (upper curves) and derivative spectra (lower curves) for (a) isotropic, (b) axial (using data obtained for DBs in a-Si:H, cf. chapter 4) and (c) rhombic symmetry. The principle values of the g-tensor for orientations of the magnetic field along the canonical directions are indicated. Simulations are carried out with the numerical simulation package easyspin [25] using the following parameters ν_{mw} = 9.7 GHz, g_{iso} = 2.0055, $g_\perp$ = 2.0065, $g_{||}$ = 2.0040, g_x = 2.0150, g_y = 2.0081, g_z = 2.0011, Gaussian line broadening ΔB_{pp} = 0.1 mT.

2.1.2 Nuclear Zeeman interaction

The nuclear spin I couples to the external magnetic field $\boldsymbol{B}_0$ by the nuclear Zeeman interaction given by

$$\mathcal{H}_{NZ} = \mu_N g_n \boldsymbol{B}_0 \boldsymbol{I}/\hbar \tag{2.5}$$

where μ_N is the nuclear magneton, g_n is the nuclear g-value and $\boldsymbol{I}$ is the nuclear spin vector operator. The magnetic moment of nuclei is about three orders of magnitude smaller than the magnetic moment of a free electron.

2.1.3 Hyperfine interaction

The hyperfine interaction between the electron spin S and the nuclear spin I given by

$$\mathcal{H}_{HFI} = \boldsymbol{S}\boldsymbol{A}\boldsymbol{I} \tag{2.6}$$

is one of the most important sources of information in EPR spectroscopy. Here the hyperfine interaction tensor is denoted by $\boldsymbol{A}$. The hyperfine interaction term in the Hamiltonian can be written as a sum of the isotropic *Fermi contact interaction* and the anisotropic electron-nuclear dipole-dipole interaction

$$\mathcal{H}_{\mathrm{HFI}} = \boldsymbol{SAI} = A_{\mathrm{iso}}\boldsymbol{SI} + \boldsymbol{SA}_{\mathrm{dip}}\boldsymbol{I} \tag{2.7}$$

where the isotropic hyperfine interaction is given by

$$A_{\mathrm{iso}} = \frac{2}{3}\frac{\mu_0}{\hbar}\mu_{\mathrm{B}} g_{\mathrm{e}} \mu_{\mathrm{N}} g_{\mathrm{n}} |\psi_0\,(0)\,|^2 \tag{2.8}$$

where $|\psi_0\,(0)\,|^2$ is the electron spin density at the nucleus. The electron-nuclear dipole-dipole interaction is given by

$$\boldsymbol{A}_{\mathrm{dip}} = \frac{\mu_0}{4\pi\hbar}\mu_{\mathrm{B}} g_{\mathrm{e}} \mu_{\mathrm{N}} g_{\mathrm{n}} \langle\psi_0| \frac{3r_i r_j - \delta_{ij} r^2}{r^5} |\psi_0\rangle. \tag{2.9}$$

where $\boldsymbol{r}$ is the vector between the electron spin and the nuclear spin. Hyperfine interaction between electron spin and nuclear spin induces a further splitting of the energy level as depicted in Fig. 2.3. In case of a nuclear spin with $I = 1/2$, each $m_S = \pm 1/2$ energy level is split into two $m_I = \pm 1/2$ levels. The selection rules for transitions induced by microwave irradiation demand that only the electron spin quantum number can be changed ($\Delta m_S = \pm 1$), while the nuclear spin quantum number remains unchanged ($\Delta m_I = 0$). Fig. 2.3 shows that in this case two allowed transitions arise, which are split by the hyperfine interaction.

In case of an isotropic hyperfine interaction tensor $\boldsymbol{A}$ and a vanishing electron-nuclear dipole interaction, the EPR spectrum is given by a doublet structure (cf. Fig. 2.4a). If the anisotropic part of the hyperfine interaction exhibits axial symmetry, the hyperfine interaction tensor can be expressed as

$$\boldsymbol{A} = \begin{pmatrix} A_\perp & & \\ & A_\perp & \\ & & A_{||} \end{pmatrix} \tag{2.10}$$

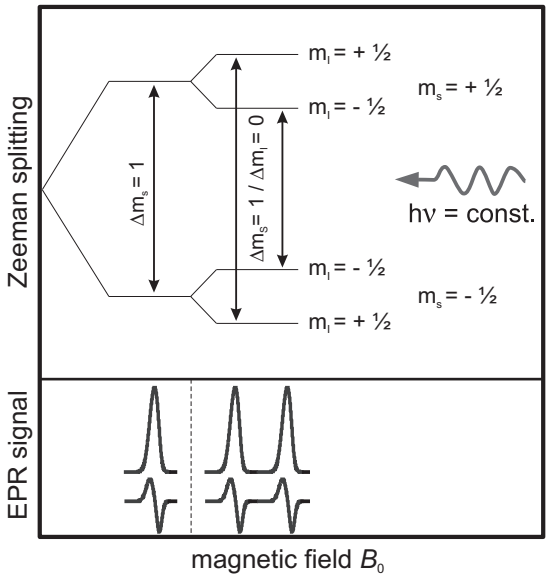

Figure 2.3: Splitting of the energy levels by the Zeeman interaction and hyperfine interaction ($I = 1/2$) for a specific orientation. Microwave irradiation induces only spin flip transition of electron spins (selection rules are indicated in the figure). upper part: Energy level diagram; lower part: Corresponding pulse (absorption) and c.w. (derivative) EPR spectra.

where

$$A_{\perp} = A_{\mathrm{iso}} - A_{\mathrm{dip}} \tag{2.11}$$

$$A_{\parallel} = A_{\mathrm{iso}} + 2A_{\mathrm{dip}} \tag{2.12}$$

and the EPR spectrum averaged over all possible orientations (powder pattern) is given by a so-called Pake-pattern (cf. Fig. 2.4b).

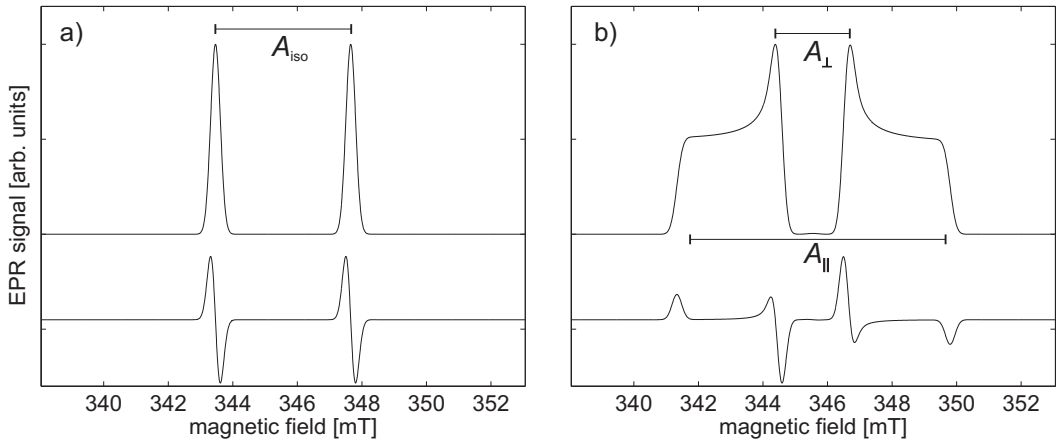

Figure 2.4: Simulations of X-Band EPR powder spectra of a paramagnetic center with $g = 2.0055$ and isotropic or anisotropic hyperfine interactions. upper traces: pulse (absorption) EPR spectra; lower trace: c.w. (derivative) EPR spectra. a) isotropic hyperfine interaction with $A_{\mathrm{iso}} = 117.7$ MHz; b) anisotropic hyperfine interaction with $A_{\mathrm{iso}} = 117.7$ MHz and $A_{\mathrm{dip}} = 60$ MHz ($A_{\parallel} = 237.7$ MHz and $A_{\perp} = 57.7$ MHz).

If the electron spin density is sufficiently concentrated at a specific site and the distance to the nucleus of interest is large one can approximate the electron spin as a point dipole. In the principal coordinate system of the hyperfine tensor, Eq. 2.9 then takes the simplified form

$$\boldsymbol{A}_{\mathrm{dip}} = \frac{\mu_0}{4\pi\hbar}\frac{\mu_{\mathrm{B}} g_{\mathrm{e}} \mu_{\mathrm{N}} g_{\mathrm{n}}}{R_{\mathrm{M}}^3} \begin{pmatrix} -1 & & \\ & -1 & \\ & & 2 \end{pmatrix}, \tag{2.13}$$

where R_{M} is the distance between the two point dipoles.

2.2 The resonance phenomenon

The various interactions of the electron spin as discussed in the above section generate a multi-level quantum system. Transitions between the different energy levels can be induced by electromagnetic radiation. If the frequency of the incident radiation matches the difference in energy between the levels, the system starts to absorb radiation and is said to be in resonance. One can therefore map all allowed transitions ($\Delta m_S = \pm 1$ or $\Delta m_I = \pm 1$) by sweeping the frequency of the electromagnetic radiation over a certain range at a fixed magnetic field monitoring the absorption of the sample. However, most EPR measurements are performed in the exact reverse way due to instrumental limitations. The frequency is held at a fixed value while the external magnetic field is swept. Since the magnetic moment of the electron is much larger than the moment of nuclei, the energy needed for a transition involving an electron spin is much higher than in the case of transitions involving nuclear spins (nuclear magnetic resonance - NMR). While NMR is typically performed using electromagnetic radiation in the radiofrequency range, EPR operates in the microwave range. EPR experiments can be carried out at various microwave frequencies, which are divided into frequency bands. An overview of the most commonly applied microwave frequencies is given in Table 2.1.

Band	band range [GHz]	typical EPR frequency [GHz]	Typical magnetic field @ $g = 2$ [mT]
S	2.6 - 4	3.0	110
X	8.2 - 12.4	9.5	340
Q	33 - 50	36	1300
W	75 - 100	95	3400
	263	263	9400

Table 2.1: Overview of microwave frequency bands and typical magnetic field for paramagnetic states with $g = 2$.

The time-dependent perturbation of the microwave radiation which induces transitions between the energy levels can be expressed as an oscillatory Hamiltonian

$$\mathcal{H}_1 = \mu_B 2\boldsymbol{B}_1 \cos(\omega t)\, \boldsymbol{g}\boldsymbol{S}/\hbar \tag{2.14}$$

with $\boldsymbol{B}_1$ denoting the vector of the linearly polarized oscillating magnetic field of the microwave radiation. After transformation of Eq. 2.14 into the rotating frame, $\mathcal{H}_1$ is time-independent and only the right-hand polarized magnetic field with amplitude B_1 can be resonant with the precession of the electron spins [21]. In cases where the magnetic quantum numbers of the electron spin (m_S) and nuclear spin (m_I) are good quantum numbers only transitions flipping the electron spin $\Delta m_S = \pm 1$ are allowed. As for electron spins, transitions flipping nuclear spins $\Delta m_I = \pm 1$ are allowed by electromagnetic radiation in the radiofrequency range. Due to state mixing by anisotropic HFI, the magnetic quantum numbers m_S and m_I may no longer be good quantum numbers, in which case forbidden transitions of the type ($\Delta m_S = \pm 1$; $\Delta m_I = \pm 1$) become partially allowed. These transitions are still referred to as forbidden, since their transition amplitude is usually much smaller than in case of allowed transitions. Excitation of forbidden transitions is the basis for many advanced pulse EPR experiments. Especially experiments which exploit the modulation of the echo-envelope by anisotropic HFI are based on non-zero transition amplitudes of forbidden transitions.

2.3 Broadening of EPR resonance lines

The resonance lines observed in an EPR experiment can be broadened in the frequency domain by homogeneous broadening and inhomogeneous broadening. Line width and broadening mechanisms are tightly linked to spin relaxation processes, which are discussed in more detail in sec. 2.6.

2.3.1 Homogeneous broadening

An ensemble of spin systems where each individual spin system composed of electron and nuclear spins is identical to the others, meaning that, they exhibit the same spin Hamiltonian and experience the same local fields, is called a spin packet. The EPR resonance line of such a spin packet is given by a homogeneous line and its shape is described by a Lorentzian function (cf. Fig. 2.5a). The width of the homogeneous line is given by $\Gamma_{\mathrm{hom}} = 2/T_{\mathrm{m}}$, where T_{m} is the phase-memory time. Homogeneous broadening can be induced by fluctuations of local fields or by spin-lattice relaxation limiting the

lifetime of the excited state of the spin system. Please refer to sec. 2.6 for further information about the important relaxation mechanisms, which determine T_m.

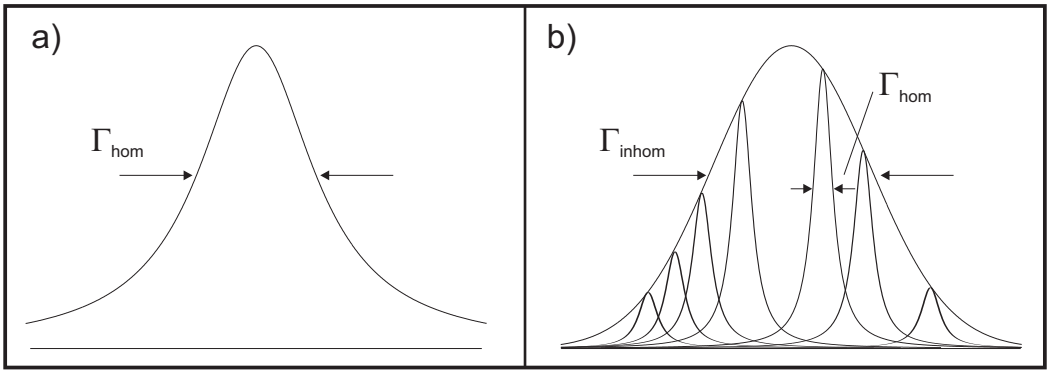

Figure 2.5: Broadening of EPR resonance lines. a) Homogeneous broadening with line width Γ_{hom}. b) Inhomogeneous broadening of the EPR resonance line by a distribution of homogeneously broadening lines with different resonance frequencies (total inhomogeneous line width Γ_{inhom}).

2.3.2 Inhomogeneous broadening

Inhomogeneously broadened EPR resonance lines are a superposition of spin packets, where each spin packet has a different resonance frequency (cf. Fig. 2.5b). The inhomogeneously broadened line shape is often a Gaussian function since the frequencies of the spin packets are usually normally distributed. In solid-state systems, inhomogeneous broadening is often much stronger than homogeneous broadening and the line width can be as large as 1 mT.

In the following we will discuss the various inhomogeneous broadening mechanisms in detail since they are important for understanding the EPR spectra of paramagnetic defects (DBs) in a-Si:H (cf. chapter 4 and 5). Due to the disordered nature of amorphous materials the defect wave function and environment varies from site to site. This variation can induce a change of the principal values of the g-tensor or a modulation of the HFI. Each defect site therefore exhibits a different resonance frequency which leads to inhomogeneous broadening of the EPR line. Fig. 2.6 shows an illustrative example of how a distribution of g-values (denoted by g-strain) can lead to a loss of spectral resolution. If g-strain is absent and the g-value is exactly defined (g = 2.0055), the HFI between

the electron spin of a paramagnetic center with a nearby nuclear spin will be completely resolved in the EPR spectrum. Considering the same spin system in a disordered solid, we have to take into account that the g-value is distributed (g-strain). In that case (cf. right hand side of Fig. 2.6) the EPR spectrum is excessively broadened and the HFI is no longer resolved. In addition to broadening by a distribution of g-values and HFIs (g- and A-strain) the EPR line can also be broadened by orientational disorder and unresolved HFIs.

Orientational disorder broadens the EPR resonance lines in case where Zeeman interaction or HFI are anisotropic. Then, the different spins in a larger spin ensemble exhibit different resonance frequencies due to a different orientation in the sample. In case all orientations are equally probable the arising resonance line is called a powder pattern.

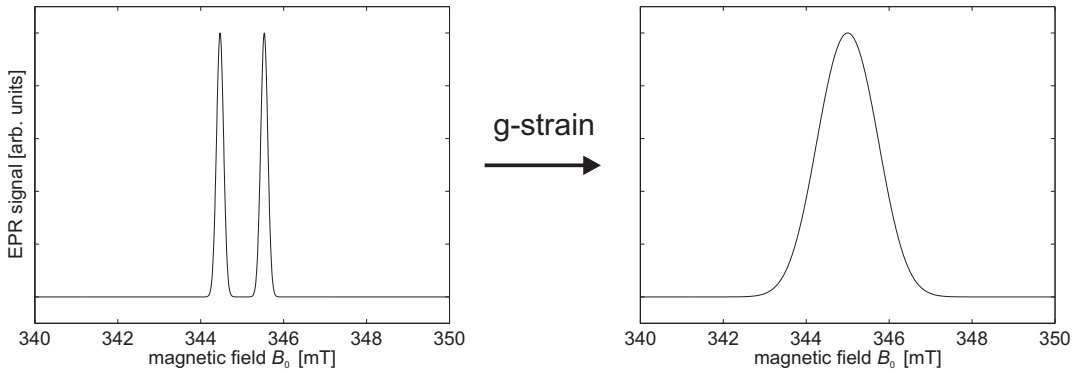

Figure 2.6: Inhomogeneous broadening induced by a distribution of g-values (g-strain). left: EPR spectrum of a paramagnetic center (g = 2.0055) with a resolved HFI of A_{iso} = 30 MHz. right: adding g-strain (Gaussian distribution with FWHM of 0.008) completely disguises the resolved HFI pattern.

Another case of inhomogeneous broadening are unresolved HFIs. If the HFIs of a spin system are sufficiently small the hyperfine multiplet may contain a large number of overlapping resonance lines. In that case the HFIs are no longer resolved in the EPR spectrum and contribute to inhomogeneous line broadening.

We have seen that the resolution of EPR spectra is limited and thus EPR parameters (g-tensor principal values or HFIs) of interest are not always accessible. To increase the resolution of inhomogeneously broadened EPR spectra, multifrequency EPR techniques (cf. chapter 4) or advanced techniques such as ESEEM or ENDOR (cf. sec. 5.3) can be applied.

2.4 S = 1/2 and I = 1/2 model system

The spin systems investigated in this thesis are in most cases composed of one electron spin $S = 1/2$ and a single nuclear spin $I = 1/2$. The spin Hamiltonian of this model system is given by

$$\mathcal{H}_0 = \Omega_S S_z + \omega_I I_z + \boldsymbol{SAI} \tag{2.15}$$

and can be diagonalized analytically. This model system will be discussed in more detail since it provides the basis for an understanding of coherent spin dynamics of advanced EPR and EDMR techniques like the primary-echo pulse sequence, two-pulse ESEEM and pulse Davies ENDOR. The spin Hamiltonian can be simplified by neglecting non-secular terms in S_x and S_y and is given by [21]

$$\mathcal{H}_0 \approx \Omega_S S_z + \omega_I I_z + A S_z I_z + B S_z I_x \tag{2.16}$$

where $\Omega_S = g\mu_B B_0/\hbar$ is the resonance frequency of spin S, $A = A_{zz}$ and $B = \sqrt{A_{zx}^2 + A_{zy}^2}$ are the secular and the pseudo-secular HFI between S and I while ω_I is the free-nuclear precession frequency of spin I. For an axially symmetric hyperfine tensor the coefficients A and B are related to the principal values $A_{||}$ and $A_\perp$ of the hyperfine tensor and the isotropic and dipolar hyperfine interaction A_{iso} and A_{dip} by [21]

$$A = A_{||}\cos^2\theta + A_\perp \sin^2\theta = A_{\text{iso}} + A_{\text{dip}}\left(3\cos^2\theta - 1\right) \tag{2.17}$$

and

$$B = \left(A_{||} - A_\perp\right)\sin\theta\cos\theta = 3A_{\text{dip}}\sin\theta\cos\theta \tag{2.18}$$

where θ is the angle between the vector of the external magnetic field and the electron-nuclear axis.

$\mathcal{H}_0$ can be diagonalized with the unitary transformation

$$\mathcal{H}_0 \xrightarrow{\xi I_y + \eta 2 S_z I_y} \mathcal{H}_0^d \tag{2.19}$$

with the angles $\eta = (\eta_\alpha - \eta_\beta)/2$, $\xi = (\eta_\alpha + \eta_\beta)/2$ and

$$\begin{aligned} \eta_\alpha &= \arctan\left(\tfrac{-B}{A+2\omega_I}\right) \\ \eta_\beta &= \arctan\left(\tfrac{-B}{A-2\omega_I}\right) \end{aligned} \tag{2.20}$$

The diagonal form of the spin Hamiltonian then takes the following form

$$\mathcal{H}_0^d = \Omega_S S_z + \frac{\omega_+}{2} I_z + \frac{\omega_-}{2} 2 S_z I_z$$

with $\omega_+ = \omega_{12} + \omega_{34}$ and $\omega_- = \omega_{12} - \omega_{34}$, where

$$\begin{aligned} \omega_{12} &= \left(\omega_I + \tfrac{A}{2}\right)\cos\eta_\alpha - \tfrac{B}{2}\sin\eta_\alpha \\ \omega_{34} &= \left(\omega_I - \tfrac{A}{2}\right)\cos\eta_\beta + \tfrac{B}{2}\sin\eta_\beta \quad . \end{aligned} \tag{2.21}$$

By $\omega_\alpha = |\omega_{12}|, \omega_\beta = |\omega_{34}|$ we denote the absolute values of the ENDOR frequencies

$$\begin{aligned} \omega_\alpha &= \sqrt{\left(\omega_I + \frac{A}{2}\right)^2 + \frac{B^2}{4}} \\ \omega_\beta &= \sqrt{\left(\omega_I - \frac{A}{2}\right)^2 + \frac{B^2}{4}} \end{aligned} \tag{2.22}$$

For the four energy eigenvalues we obtain

$$\begin{aligned} |1\rangle : \epsilon_1 &= \frac{\Omega_S}{2} + \frac{\omega_{12}}{2}, \\ |2\rangle : \epsilon_2 &= \frac{\Omega_S}{2} - \frac{\omega_{12}}{2}, \\ |3\rangle : \epsilon_3 &= -\frac{\Omega_S}{2} + \frac{\omega_{34}}{2}, \\ |4\rangle : \epsilon_4 &= -\frac{\Omega_S}{2} - \frac{\omega_{34}}{2}, \end{aligned} \tag{2.23}$$

For the four eigenstates in the Cartesian product basis we find

$$
\begin{aligned}
|1\rangle &= \cos\left(\frac{\eta_\alpha}{2}\right)|\uparrow_S\uparrow_I\rangle - \sin\left(\frac{\eta_\alpha}{2}\right)|\uparrow_S\downarrow_I\rangle,\\
|2\rangle &= \sin\left(\frac{\eta_\alpha}{2}\right)|\uparrow_S\uparrow_I\rangle + \cos\left(\frac{\eta_\alpha}{2}\right)|\uparrow_S\downarrow_I\rangle,\\
|3\rangle &= \cos\left(\frac{\eta_\beta}{2}\right)|\downarrow_S\uparrow_I\rangle - \sin\left(\frac{\eta_\beta}{2}\right)|\downarrow_S\downarrow_I\rangle,\\
|4\rangle &= \sin\left(\frac{\eta_\beta}{2}\right)|\downarrow_S\uparrow_I\rangle + \cos\left(\frac{\eta_\beta}{2}\right)|\downarrow_S\downarrow_I\rangle.
\end{aligned}
\tag{2.24}
$$

In Fig. 2.7a) and b) the theoretically obtained results are illustrated in an energy level diagram and a schematic EPR spectrum.

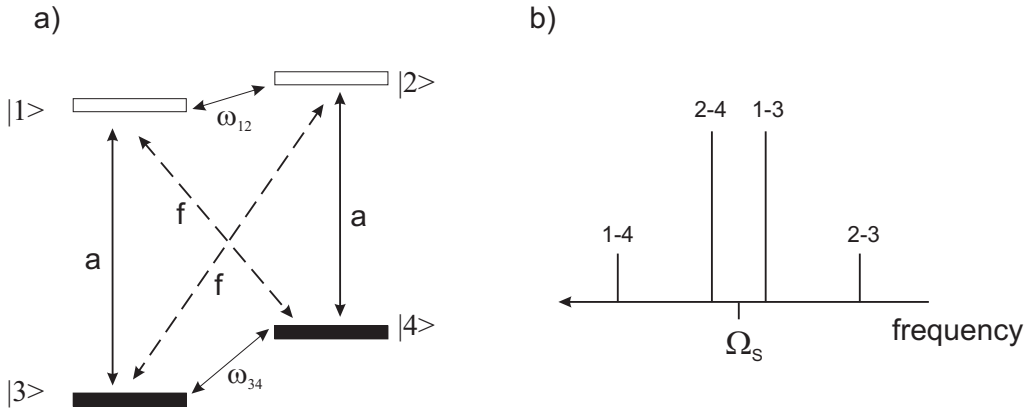

Figure 2.7: Energy level diagram (a) and corresponding transition frequencies in a schematic EPR spectrum (b) for a $S = 1/2$, $I = 1/2$ spin system with $\omega_I < 0$ and $A, B > 0$ in case of weak-coupling $|A| < |2\omega_I|$. Allowed transitions are denoted by a, forbidden transitions by f. The transition probabilities for allowed and forbidden transitions are sketched by the length of the columns in b).

2.5 Pulse EPR

This section provides a short overview of the EPR microwave pulse sequences applied in this thesis.

Two-pulse electron spin echo Exciting the spin system with a short microwave pulse to generate transversal magnetization from longitudinal polarization is the most simple

EPR pulse sequence. The decay of the transversal magnetization is, however, quite fast due to a dephasing of the different spin-packets of an inhomogeneously broadened EPR resonance line. The signal decay is most often too fast to be observed due to finite spectrometer dead time, inherent to every EPR experiment. However, dephasing of spin packets can be reversed by applying an additional microwave pulse after time τ flipping the electron spins by an angle π. As a consequence the spin packets refocus to form an electron spin echo. The complete pulse sequence generating this so-called primary echo is shown in Fig. 2.8. The two-pulse sequence can be used for various purposes. The echo intensity is a direct measure of the longitudinal magnetization and by recording echo intensity versus external magnetic field, the EPR spectrum of the spin system can be obtained. However, in contrast to the EPR spectrum obtained by c.w. EPR techniques the EPR spectrum determined by the field-swept echo (FSE) detected technique is subject to transversal relaxation effects and can depend on the pulse delay time τ [21]. The transversal relaxation can be investigated in more detail by recording the echo intensity as a function of the pulse delay time τ. The time constant and the function of the decay of the primary echo contain important information about the relaxation mechanism. A detailed overview of transversal relaxation mechanisms is presented in sec. 2.6.

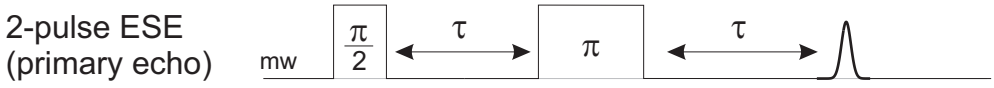

Figure 2.8: Two-pulse ESE sequence to generate a primary echo. This sequence is used to measure the field-swept echo detected EPR spectrum (fixed τ), the transversal relaxation properties by the primary-echo decay (incrementing τ) and ESEEM modulations on the primary-echo decay (incrementing τ).

Electron-spin-echo envelope modulations The two-pulse sequence and the decay of the primary echo can also be used to measure HFIs by electron-spin-echo envelope modulations (ESEEM). If the HFI is anisotropic, the echo decay is modulated with nuclear frequencies. In case of the above discussed model system of a single electron spin $S =$

1/2 coupled to a nuclear spin $I = 1/2$, it can be shown that the echo modulation function is given by

$$I_{2p}(\tau) = 1 - \frac{k}{4}(2 - 2\cos\omega_\alpha\tau - 2\cos\omega_\beta\tau + \cos\omega_+\tau + \cos\omega_-\tau) \quad (2.25)$$

where $k = \sin^2 2\eta$ is the modulation amplitude. The oscillation frequencies ω_α, ω_β, ω_+, and ω_- can be obtained from the time domain echo decay by Fourier transformation. This result is applied in sec. 5.3 to investigate the distribution of H atoms in the vicinity of paramagnetic defects in a-Si:H.

Pulse Davies-ENDOR A different technique to measure HFIs is given by electron-nuclear double resonance (ENDOR), a combination of a nuclear magnetic resonance and EPR experiment. The pulse version of the ENDOR technique applied in this work is the Davies ENDOR sequence $\pi - \mathrm{RF} - \pi/2 - \tau - \pi - \tau - \mathrm{echo}$, where the radiofrequency pulse inducing nuclear transitions is indicated by RF [27]. The pulse sequence and the spin dynamics in case of the $S = 1/2$, $I = 1/2$ model system are illustrated in more detail in Fig. 2.9. It is assumed that the HFI is isotropic in which case the eigenstates ($|1\rangle$, $|2\rangle$, $|3\rangle$ and $|4\rangle$) are given by the Cartesian product basis. The initial π-pulse is applied selectively on transition 1-3 and inverts populations of the spin transition. The population difference on this transition can be detected by a two-pulse ESE sequence. If the frequency of the rf-pulse is non-resonant $\nu_{\mathrm{rf}} \neq \nu_{\mathrm{res}}$ with the nuclear spin transition 1-2 (case b in Fig. 2.9) the populations are unchanged and remain inverted. The detected echo signal is then fully inverted. If the rf-pulse is resonant $\nu_{\mathrm{rf}} = \nu_{\mathrm{res}}$ with 1-2 (case a in Fig. 2.9) spin populations are transferred from $|1\rangle$ to $|2\rangle$. In this case the detected echo signal is less inverted or, in the ideal case, equal to zero. The difference between the non-resonant case and the resonant case then constitutes the measured ENDOR signal. It is important to note that in case of a non-selective initial EPR π-pulse both transitions (1-3 and 2-4) are inverted and no ENDOR signal can arise. The Davies ENDOR sequence therefore has a natural blind spot (Davies hole) for nuclei with a very weak HFI since the transitions of such a spin system are easily inverted. The excitation bandwidth of the initial inversion pulse has to be chosen with great care.

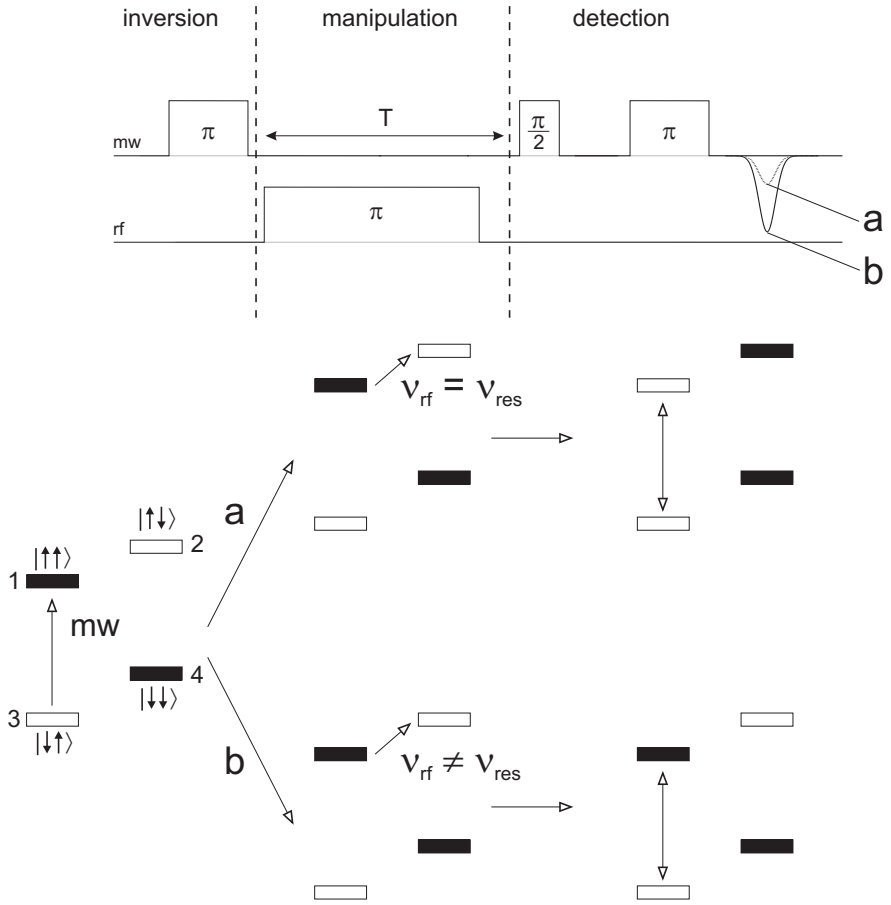

Figure 2.9: Pulse Davies-ENDOR sequence to measure the ENDOR spectrum (varying rf frequency). There is no ENDOR response in case of non-selective inversion pulse. For details see text.

2.6 Spin relaxation

In the preceding section we discussed static interactions within the spin system described by the spin Hamiltonian. However, the spin system cannot be treated as an isolated quantum system since it interacts with its environment. Dynamic changes in the environment, for example lattice vibrations or particle diffusion, lead to a time-dependent perturbation of the spin system and cause a relaxation of excited spin populations (longitudinal relaxation) or a relaxation of spin coherence (transversal or phase relaxation).

2.6.1 Longitudinal relaxation

Relaxation of the macroscopic magnetization oriented in parallel to the quantization axis is denoted by longitudinal relaxation and is generally connected to a transfer of energy from the spin system to the environment changing the magnetic quantum number m_S or m_I of the spin system. The mechanism of longitudinal relaxation is thermal motion of atoms surrounding the spin system. In solids, thermal motion is described by lattice vibrations, such as phonons in crystals or low-energy excitations in glasses. In this particular case, the energy transfer between the spin system and the lattice is referred to as spin-lattice relaxation. The dominant microscopic mechanism behind this energy transfer is a modulation of the Zeeman or hyperfine interactions by the lattice vibrations [28]. Longitudinal relaxation is strongly temperature dependent, since motional degrees of freedom are frozen out at lower temperatures and therefore no longer contribute to the relaxation. The characteristics of the temperature dependence can often be exploited to identify the microscopic mechanism behind the longitudinal relaxation.

In the following we briefly discuss the most relevant processes for spin-lattice relaxation in solids. The simplest process which leads to a spin-flip is a *direct process* where one phonon is absorbed or emitted by the spin system. The density of states of lattice vibrations in the Debye approximation is given by

$$\rho(\omega) \propto \omega^2 \tag{2.26}$$

and is in general quite small at the usually employed EPR microwave frequencies. A more efficient process is the *Raman* process, where one phonon of energy ω_1 is absorbed to excite the spin system to a virtual level and a second phonon of frequency ω_2 is

emitted with $|\omega_2 - \omega_1|$ equal to the EPR microwave frequency. This process is much more efficient in the high-temperature limit (T > 100 K) and often dominates the spin-lattice relaxation since it makes use of the complete phonon spectrum. If the virtual level happens to be an excited state of the spin system, the process is called an Orbach process [29]. There are several theoretical and experimental studies of spin-lattice relaxation of ions, defects or impurities in crystalline solids or semiconductors which predict distinct temperature dependencies for the direct, Raman and Orbach spin-relaxation processes [28–30]. The different processes may also exist simultaneously and dominate the spin-lattice relaxation in different temperature regimes. In that case a very complicated overall temperature dependence can arise, e.g. for phosphorous donors in crystalline silicon [31]. We will, however, not discuss these temperature dependencies in detail, since all of these studies make use of the Debye model, an approximation which is grossly incorrect in the case of low-temperature glasses or non-crystalline substances such as a-Si:H [32]. The anomalous low-temperature behavior of the heat capacity and thermal conductivity of these substances suggest the presence of additional low-energy modes. Since the origin of these modes is mostly unknown it becomes difficult to predict theoretically spin-lattice relaxation times for non-crystalline systems like a-Si:H.

2.6.2 Transversal relaxation

In contrast to longitudinal relaxation, transversal relaxation does not rely on a transfer of energy from the spin system to the environment. Transversal relaxation arises due to loss of the phase relation between electron spins which are prepared in a coherent superposition of eigenstates. The perturbation of the environment induces a fluctuating local magnetic field, which leads to a random change of precession frequency and phase relation between the individual electron spins. As a consequence, the coherent superposition is destroyed although the spin system has not yet returned back to thermal equilibrium. This process is referred to as decoherence. In solids, the decay of the transversal magnetization is often not universal and depends very much on the employed EPR pulse sequence measuring the transversal relaxation. The most important microwave pulse sequence is the primary-echo sequence ($\pi/2 - \tau - \pi -$ echo) refocusing the transversal magnetization. An empirical parameter which is often used to analyze the decay of the primary-echo is the phase-memory time constant T_m. However, the decay is not always

mono-exponential and complicated decay functions may arise. There are many mechanisms causing transversal relaxation, which we will briefly describe in the following. To summarize the most important contributions for transversal relaxation, the decay of the primary echo (pulse delay τ) can be written in the following form

$$I_e(\tau) = I_e(0) \exp[-2\tau/T_m] \exp[-\sum_j \left(2\tau/T_{SD}^j\right)^{n_j}] \tag{2.27}$$

where the first term includes the phase-memory time T_m and the second term accounts for spectral diffusion processes. WithT_{SD}^j we denote the characteristic time and with n_j the exponent describing the spectral diffusion process j. Here we have explicitly separated the T_m processes from spectral diffusion processes since T_m represents an intrinsic limit for the transversal relaxation, while spectral diffusion processes can often be avoided by using appropriate microwave pulse sequences [33].

Phase-memory time T_m The intrinsic phase-memory time T_m is a summary of exponential decay time constants

$$\frac{1}{T_m} = \frac{1}{2T_1} + \frac{1}{T_2} \tag{2.28}$$

where $2T_1$ is life-time broadening time constant and T_2 is the spin-spin relaxation time constant. We see that longitudinal relaxation also induces transversal relaxation since the coherence is lost upon a spin flip of the electron. The spin-lattice relaxation time constant T_1 or the life-time of a longitudinal excitation is therefore the ultimate limit for T_m. However, in most cases the life-time contribution is outweighed by an energy conserving flip-flop process involving two electron spins, where the energy of the first spin is transferred to the second. This process is more efficient in relaxing the phase of the electron spins and is denoted by spin-spin relaxation T_2.

Spectral diffusion resulting from electron-electron spin-spin dipolar interactions The most important processes limiting the decay of the primary echo in solids is spectral diffusion due to electron-electron or electron-nuclear dipole-dipole interactions [34]. These processes also majorly influence the primary-echo decay of defects in a-Si:H (cf. sec. 5.2). The spectral diffusion mechanism is active if only a part of the EPR spectrum

is excited in a microwave pulse sequence. The spin populations are divided into two parts: the excited electron spins are referred to as A-spins (observer position) and the unexcited (electron or nuclear) spins are denoted by B-spins. Unexcited B-spins cause a phase relaxation of A-spins by the spectral diffusion mechanism, which works in the following way. The dipolar interaction between B-spins and A-spins shifts the resonance frequency of A-spins. These shifts fluctuate in time when B-spins carry out random spin flips by either spin-lattice relaxation or spin diffusion (flip-flops). A-spins therefore start to diffuse through the EPR spectrum. Since this is a random process, the phase relation between different A-spins is destroyed, and spectral diffusion cannot be refocused in a primary echo experiment. If spin-flip frequency of the B-spins W_B is high compared to inverse pulse delay time τ of the microwave pulse sequence ($W_B\tau > 1$), the primary echo decay is given by [34]

$$I_e(2\tau) = \exp\left[-\frac{\mu_0 2\sqrt{\pi}}{9\sqrt{3}\hbar} g_A g_B \mu_B^2 C_B \left(\tau/W_B\right)^{1/2}\right] \tag{2.29}$$

where C_B is the concentration of B-spins and g_A and g_B are the g-values of A- and B-spins. We see that the decay is not mono-exponential and the characteristic exponent for this spectral diffusion process is $n = 1/2$. It is important to point out that B-spins can either be electron spins of the same sort as A-spins, for example a different population in a strongly inhomogeneously broadened line, or of different kind with a completely different EPR spectrum. The latter case was observed for H atoms (A-spins) in glassy matrices of sulfuric acid containing transition metal ions acting as B-spins [35]. The transition metal ions are in some cases not visible in the EPR spectrum due to their short spin-lattice relaxation time T_1 but strongly influence the primary-echo decay of the H-atoms (A-spins).

Spectral diffusion resulting from electron-nuclear dipole-dipole interactions In most solid-state systems which contain a large percentage of magnetic nuclei the primary-echo decay is limited by spectral diffusion resulting from electron-nuclear dipole-dipole interactions. This also applies to defects in a-Si:H (cf. sec. 5.2). Nuclear spins such as ^{1}H or ^{29}Si act as B-spins and modulate the resonance frequency of A-spins (electron spins) by electron-nuclear dipole-dipole hyperfine interaction. The reorientation of nuclear spins is induced by nuclear spin-spin relaxation (spin diffusion) [36]. A theoretical

description of the resulting primary-echo decay is complex and depends on the specific spin system [37]. However, in most cases the decay can be approximated by a stretched exponential function

$$I_e(2\tau) = \exp[-(2\tau/T_{SD})^n] \tag{2.30}$$

with $2 \leq n \leq 3$ and T_{SD} denoting the spectral diffusion characteristic time [36]. The process is temperature independent since the reorientation of the nuclear spins is induced by spin-spin relaxation and not by spin-lattice relaxation [36]. A well-studied spin system where the nuclear-spin induced spectral diffusion dominates the primary-echo decay is given by phosphorous impurities in crystalline silicon [38]. Here n and T_{SD} vary strongly in dependence of the ^{29}Si concentration of the samples and are found to be anisotropic, that is, the values depend on the relative orientation between the external magnetic field and the crystallographic axes.

Instantaneous diffusion The transversal magnetization in a primary-echo experiment can also decay by dipolar spin-spin interactions between pairs of A-spins [34, 35]. If one of the electron spins is excited by the microwave pulse and flipped by a certain angle, the other electron spin will experience a change in the local magnetic field which changes the spin resonance frequency leading to spectral diffusion. This effect is known as instantaneous diffusion and manifests itself by a flip-angle dependence of the primary echo decay. The echo decay function including these dipolar interactions is given by [34]

$$I_e(2\tau) = \exp\left[-\frac{\mu_0\pi}{9\sqrt{3}\hbar} g_A^2 \mu_B^2 C_A \left\langle \sin^2\frac{\beta(\omega)}{2}\right\rangle_{g(\omega)} \cdot 2\tau\right] \tag{2.31}$$

where β is the flip angle by which the A spins with resonance frequency ω are turned, C_A is the concentration of A-spins and $\langle ... \rangle_{g(\omega)}$ indicates averaging over the EPR spectrum. Eq. 2.31 predicts that if the concentration C_A is sufficiently high, the spins will interact via strong spin dipolar interaction and the echo decay is well described by an exponential decay with a strong flip-angle dependence. This dependence can be tested experimentally by decreasing the microwave power but keeping the pulse length constant to obtain a smaller flip angle.

Spectral diffusion by frequent A-spin flips Eq. 2.31 and 2.29 are valid if A-spins flip only infrequently, that is, their spin-flip frequency W_A is small ($W_A\tau < 1$). If their spin-flip frequency is high ($W_A\tau > 1$) A-spins start to contribute to their own primary-echo decay via spectral diffusion due to dipolar coupling between them. The expressions for the primary-echo decay are lengthy and shall not be discussed here in detail [34]. It is, however, important to note that frequent spin flips of A-spins tend to disguise the instantaneous diffusion, since the additional spin flip due to microwave pulses is no longer significant on a background of many spin flips. This is important when analyzing the flip-angle dependence of the primary-echo decay of defects in a-Si:H (cf. sec. 5.2). Again the random spin flips are either induced by spin-lattice relaxation or spin diffusion (flip-flops). If the process is induced by spin-lattice relaxation, W_A and the primary-echo decay will exhibit a strong temperature dependence [34]. In case reorientation of the A-spins is induced by spin-spin relaxation (flip-flops), the primary-echo decay time constants are temperature independent.

2.7 EDMR of paramagnetic states in µc-Si:H solar cells

In the above section we showed that EPR spectroscopy is a powerful tool to investigate the electronic and microscopic structure of paramagnetic defect centers in solar cell materials. However, EPR is not directly applicable to fully-processed solar cells due to its low sensitivity. In contrast to EPR, electrical detection of magnetic resonance (EDMR) exhibits a superior sensitivity down to single spin level [39]. The basic principle of EDMR relies on the observation that transport and recombination processes of charge carriers in solar cells depend on the spin state of paramagnetic defects or impurities participating in these processes. Microwave irradiation of the solar cell changes spin states and therefore influences the (photo-) conductivity, which then constitutes the measured observable. Despite the superior sensitivity of EDMR, pulse EDMR experiments which allow to exploit the full potential of the technique are poorly developed due to a number of experimental difficulties in the current detection. This section together with chapter 6 give a detailed introduction to a novel pulse EDMR-ESEEM (ED-ESEEM) technique, which allows to determine small HFIs of paramagnetic defects or impurities in thin-film solar cells which are otherwise not resolvable in the EDMR spectrum. The purpose of this theoretical

section is twofold. First a detailed introduction to spin-dependent conductivity in µc-Si:H solar cells on the basis of the well-established spin pair theory of Kaplan, Solomon and Mott (KSM) is presented [40]. Secondly, a detailed theoretical treatment of spin dynamics of the novel ED-ESEEM sequence is given, which was developed in the present thesis. A thorough treatment of this problem is necessary to correctly interpret the experimental ED-ESEEM spectra presented in chapter 6.

2.7.1 Spin-dependent hopping transport in µc-Si:H p-i-n solar cells

In order to investigate the microscopic structure of paramagnetic defects in µc-Si:H p-i-n solar cells, we first need a detailed understanding of the working principle and charge-carrier transport processes of the solar cell. The working principle relying on a separation of e-h pairs by internal electric fields is shortly described in Fig. 2.10.

Spin-dependent processes involving paramagnetic defects of interest are described within the framework of the KSM spin pair model [40]. Transport of charge carriers in doped and undoped a-Si:H or µc-Si:H at low temperature (T = 10 K) can occur by charge-carrier hopping between localized states in the band tails of disordered materials [41–43]. In phosphorus doped a-Si:H, the involved localized states are conduction band tail states (denoted by e-centers in the following) and neutral fourfold coordinated phosphorus donors P_4^0 (cf. Fig. 2.10). Both of these states are paramagnetic in n-type a-Si:H [44]. In intrinsic µc-Si:H, charge-carrier hopping between shallow paramagnetic states below the conduction band edge (CE-centers) can contribute to the conductivity [45].

In contrast to extended state conduction, hopping relies on tunneling transitions between localized states. However, only those localized states which are part of a percolation path through the sample contribute to the current [42]. Let us assume that there is one part of such a percolation path where an electron has to transfer from an e-center (state A) to a P_4^0 donor (state B) where the latter is already occupied by an electron (cf. Fig. 2.11). In that case an exclusive spin pair in an intermediate state is formed, since the transition probability for electron A tunneling onto state B forming a doubly-occupied state is higher than tunneling onto any other state. The two electrons of the spin pair can either occupy the same state or dissociate. The tunneling transition is spin conserving due to the low spin-orbit coupling of Si [46]. If the two electron spins

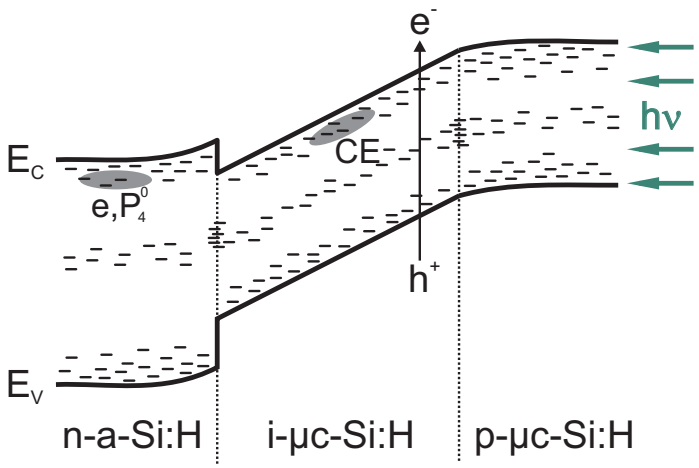

Figure 2.10: Schematic band diagram and working principle of a µc-Si:H p-i-n thin film solar cell. The solar cell is illuminated through the p-layer and light is absorbed in the intrinsic µc-Si:H layer generating excess charge carriers (e^- and h^+). The separation of e-h pairs occurs by the internal electric field generated by the doped a-Si:H and µc-Si:H layers. At low temperatures (T = 10 K) charge-transport pathways through the solar cell are among others hopping transport between paramagnetic states close to the conduction band. In the n-type a-Si:H layer these are conduction-band tail states (e-centers) and neutral phosphorus donors P_4^0. In the intrinsic µc-Si:H absorber layer, charge-carrier hopping occurs under the participation of CE-centers.

in the intermediate state exhibit the same spin state ($m_S = \pm 1/2$) the final state will be a spin triplet ($S = 1$). The Pauli principle, however, requires that the doubly occupied state is a spin singlet ($S = 0$) and blocks the transport (cf. upper case in Fig. 2.11).

Using microwave irradiation resonant with electron spin of state B ($\nu_{mw} = \nu_B$) flips the spin (cf. lower case in Fig. 2.11) and induces a transition from the triplet spin state to a mixed state with higher singlet content. For spin pairs in the singlet state tunneling transition of the electron A onto state B is allowed and state B will be doubly occupied. In a further spin-independent step the electrons dissociate by hopping of one charge carrier onto a neighboring unoccupied state. The overall effect of microwave irradiation is to enhance the conductivity of the sample.

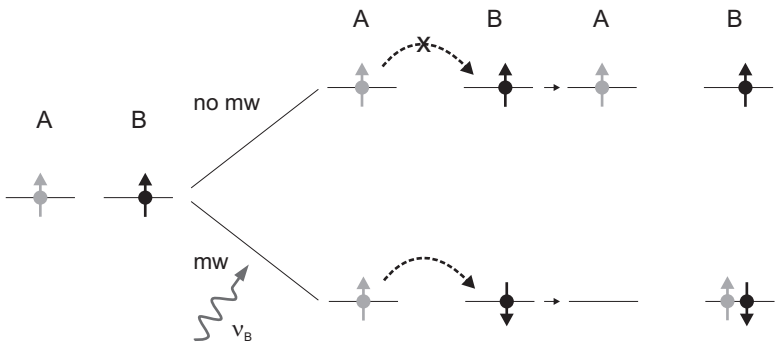

Figure 2.11: Spin-dependent hopping conductivity in the KSM spin-pair model. Two electron spins occupying two localized states A and B form a spin pair. The spin state ($m_S = \pm 1/2$) is indicated by grey or black arrows. Without microwave irradiation the charge carrier transport remains blocked while in the case of microwave irradiation resonant to spin B ($\nu_{mw} = \nu_B$) charge carrier transport becomes allowed.

The spin pair consisting of two electron spins with $S_{1,2} = 1/2$ gives rise to four energy eigenstates sketched in Fig. 2.12. There are two triplet states with parallel alignment of the electron spins $|T+\rangle = |\uparrow\uparrow\rangle$ and $|T-\rangle = |\downarrow\downarrow\rangle$. The two other states $|2\rangle$ and $|3\rangle$ are mixed states of singlet $\frac{1}{\sqrt{2}}(|\uparrow\downarrow\rangle - |\downarrow\uparrow\rangle)$ and triplet states [47]. Initially the four eigenstates in the intermediate state are equally populated since the generation rate is spin-independent. However, the transition rate from the intermediate state to the final doubly-occupied singlet state is highly spin-dependent. The rate coefficients from the triplet states r_T (cf. Fig. 2.12) are much smaller than from states $|2\rangle$ and $|3\rangle$. In the steady-state when there is a continuous generation and dissociation of spin pairs,

a highly non-equilibrium state is formed. In case $r_{2,3} \gg r_T$, the $|2\rangle$ and $|3\rangle$ states are completely depopulated due to their small lifetime and a surplus of triplet states remains. The non-equilibrium state of the spin pair is therefore a spin-correlated state. By inducing transitions between eigenstates of the intermediate state by microwave irradiation the overall transition rate to the final doubly-occupied singlet state increases. As a consequence the total photocurrent flowing through the thin-film solar cell changes and constitutes the observable in c.w. EDMR and pulse EDMR measurements.

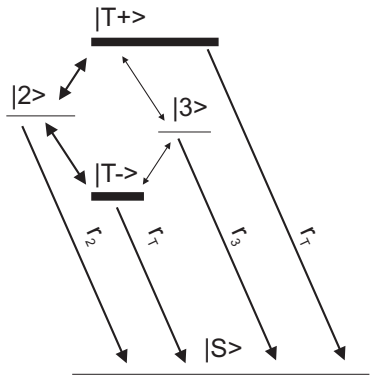

Figure 2.12: Energy level diagram of an electron spin pair. The final doubly-occupied state is denoted by the singlet state at the bottom ($S = 0$). Rate coefficients of transitions from intermediate to final state are indicated by $r_{2,3,T}$.

Quantitatively, spin pair populations in steady state within the product operator-formalism are well-described by a triplet precursor density matrix

$$\sigma_{SS}^{T} = \frac{1}{2}\left(S_1^{\alpha}S_2^{\alpha} + S_1^{\beta}S_2^{\beta}\right) = \frac{1}{2}\left(\frac{1}{2} + 2S_{1z}S_{2z}\right). \tag{2.32}$$

The product operator-formalism provides a convenient way to calculate the evolution of the spin system, which is equivalent to an explicit calculation of the matrix entries in the established density-matrix formalism [21, 48]. If we now apply a microwave pulse (flip-angle ϕ) to electron spin S_1 a transition from triplet to singlet states is induced. The evolution of the density matrix under application of the S_{1x} operator describing a rotation of S_1 can be calculated using the Liouville equation

$$\frac{\partial\sigma}{\partial t} = -\frac{i}{\hbar}[\mathcal{H}, \sigma]$$

and is given by [21]

$$\sigma_{SS}^{T} \xrightarrow{\phi S_{1x}} \sigma^{*} \tag{2.33}$$

where we abbreviated unitary transformations $V = UXU^{\dagger}$ with the unitary operator $U = e^{-i\phi\hat{O}}$ by $X \xrightarrow{\phi\hat{O}} V$. We have already seen that microwave manipulation of spin systems leads to an observable change of the photocurrent. It was shown by Boehme and Lips [49] that the transient change of the photocurrent is determined by the deviation of the triplet population from its steady-state value

$$\begin{aligned} \Delta I_{ph}(t) \propto \sigma_{SS}^{T_+} - \sigma^{T*} &= \mathrm{Tr}[\sigma_{SS}^{T} S_1^{\alpha} S_2^{\alpha}] - \mathrm{Tr}[\sigma^{*} S_1^{\alpha} S_2^{\alpha}] \\ &= \mathrm{Tr}\left[\frac{1}{2}\left(\frac{1}{2} + 2S_{1z}S_{2z}\right)\left(\frac{1}{4} + \frac{1}{2}S_{1z} + \frac{1}{2}S_{2z} + S_{1z}S_{2z}\right)\right] \\ &\quad -\mathrm{Tr}\left[\sigma^{*}\left(\frac{1}{4} + \frac{1}{2}S_{1z} + \frac{1}{2}S_{2z} + S_{1z}S_{2z}\right)\right] \end{aligned} \tag{2.34}$$

Since the single electron spin polarization S_{1z} or S_{2z} is negligible in our case (B_0= 0.35 T, T = 10 K), the observable transient current response is solely determined by longitudinal two-spin order $S_{1z}S_{2z}$ in the final state

$$\Delta I_{\mathrm{ph}}(t) \propto 1 - \mathrm{Tr}\left[\sigma^{*} S_{1z} S_{2z}\right]. \tag{2.35}$$

It is therefore possible to read out the spin state of the system after the microwave pulse as shown by Rabi oscillation measurements on the above discussed µc-Si:H thin-film solar cells [50].

2.7.2 ED-ESEEM of paramagnetic defects in thin-film solar cells

In the following we present an analytical treatment of the novel ED-ESEEM pulse sequence. The calculation is carried out for a correlated electron-spin pair coupled to one or two nuclear spins. It is shown that the anisotropic HFI between the selectively excited electron spin and a nuclear spin can cause an oscillation of the primary spin echo response as observed by pulse EDMR. The characteristic oscillation frequencies are linked to HFIs.

The above presented concept to read out the electron spin state can be generalized to determine the density matrix after a series of microwave pulses and delay times, as for example in case of a two-pulse ESE sequence, which can also be applied to measure

ESEEM. The two-pulse ESE sequence consists of two microwave pulses with a flip angle of $\pi/2$ and π, separated delays τ_1 and τ_2. The microwave pulse sequence generates a primary echo at time $\tau_2 = \tau_1$ (cf. Fig. 2.13). In order to determine the spin state at the time of echo formation with pulse EDMR an additional $\pi/2$ read-out pulse to project the transversal magnetization to longitudinal magnetization has to be added. The following current transient then serves as the observable in a pulse EDMR experiment (cf. Fig. 2.13).

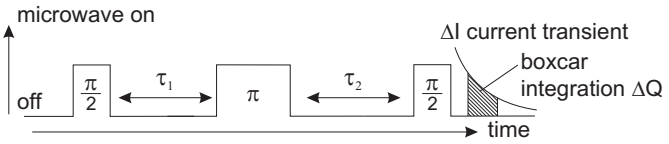

Figure 2.13: Primary spin-echo microwave pulse sequence. The primary echo is generated at time $\tau_2 = \tau_1$ and is projected to longitudinal polarization by an additional $\pi/2$ - pulse for detection via the following current transient, whose amplitude depends on the spin-density matrix.

The evolution of the density matrix during the two-pulse ESE sequence can be calculated by a series of transformations where we assume that S_1 is excited selectively

$$\sigma_{SS}^{T} \xrightarrow{\frac{\pi}{2}S_{1x}} \xrightarrow{U} \xrightarrow{\mathcal{H}_0^d\tau} \xrightarrow{-U} \xrightarrow{\pi S_{1x}} \xrightarrow{U} \xrightarrow{\mathcal{H}_0^d\tau} \xrightarrow{-U} \xrightarrow{\frac{\pi}{2}S_{1x}} \sigma^*(2\tau) \tag{2.36}$$

with U describing the transformation from the Cartesian product basis to the eigenbasis of the spin system and $\mathcal{H}_0^d$ denoting the diagonal spin Hamiltonian. With Eq. 2.35 we obtain the following result for the change of the photocurrent at time of echo formation ($\tau_1 = \tau_2$)

$$\Delta I_{ph}^{echo}(2\tau) \propto 1 - \mathrm{Tr}\left[\sigma^*(2\tau) S_{1z} S_{2z}\right] = 1 + I_{2p}(\tau) \tag{2.37}$$

where $I_{2p}(\tau)$ denotes the intensity of the primary echo as observed by the pulse EDMR sequence. The intensity of the echo is subject to electron-spin echo envelope modulations (ESEEM) as a function of the pulse delay τ, if the electron spin S_1 exhibits anisotropic HFI with a nearby magnetic nucleus. In the following, a detailed theoretical treatment of the echo intensity is given to derive a quantitative expression for $I_{2p}(\tau)$ as a function of

the HFIs. This is important for a quantitative analysis of the experimental ED-ESEEM spectra presented in chapter 6.

We have seen that the paramagnetic states in µc-Si:H thin-film solar cells form spin pairs which influence the photocurrent. The paramagnetic states of the spin pairs interact with various magnetic nuclei present in the solar cell layers by HFI. Highly abundant nuclei are ^{29}Si, ^{31}P and ^{1}H introduced by intentional doping. A measurement of the HFIs of these nuclei yields a detailed picture of the microscopic structure of the paramagnetic defects. One of the main contribution to the spin-dependent conductivity in µc-Si:H thin-film solar cells is given by correlated spin pairs consisting of e-centers and P_4^0 donors. This spin pair will serve as a model system in the following to analyze the energy eigenvalues and eigenstates. The theoretical treatment is, however, quite general and can also be applied to CE-centers and other paramagnetic states forming spin pairs in semiconductors. In chapter 6 we will see that a measurement of the two-pulse EDMR ESE decay on the e-center/P_4^0 spin pair transitions shows oscillations due to HFI with magnetic nuclei. In the following we will discuss how the frequencies of the oscillations are linked to the HFIs and, in the case of phosphorus, decide which kind of ^{31}P nuclei give rise to the observed ESEEM pattern. Before we analyze the microwave pulse sequence and the evolution of the density matrix, it is necessary to discuss the spin Hamiltonian of the e-center/P_4^0 spin pair coupled to nuclear spins. In general there is a multitude of nuclei in the vicinity of the spin pair. However, the complex problem can be reduced to two simpler cases:

1. There is one additional nucleus in the vicinity of the spin pair (cf. Fig. 2.14a),
2. There are no additional nuclei in the vicinity of the spin pair. In that case both electron spins are coupled to the nuclear spin of the P_4^0 donor (cf. Fig. 2.14b).

Both cases are shown schematically in Fig. 2.14. In the following we will investigate the eigenstates and spin transitions in these two cases and denote the electron spin of the e-center by S_1 , the electron spin of the P_4^0 donor by S_2. Similarly, the nuclear spin of the P_4^0 donor is denoted by I_2 and nuclear spins of other atoms in the vicinity of S_1 (e.g. ^{29}Si, ^{31}P or ^{1}H) are denoted by I_1. In the first case it is assumed that the electron spin of the e-center is not coupled to the nuclear spin of the P_4^0 donor since this is already covered by the second case. Please note that the HFI between S_2 and I_2, denoted by $A_{\mathrm{iso}}^{\mathrm{P}}$ is very large ($A_{\mathrm{iso}}^{\mathrm{P}} \approx 800$ MHz) [44].

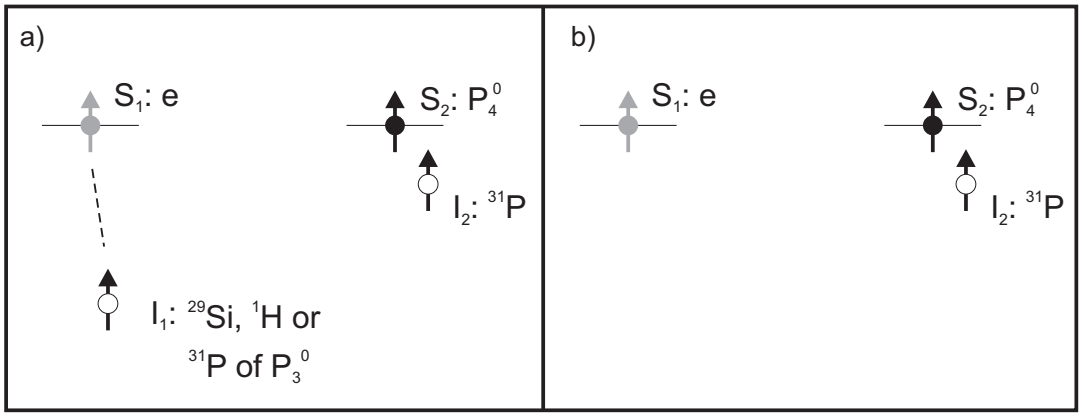

Figure 2.14: Schematic HFIs of e-center/P_4^0 spin pair. Electrons are denoted by full circles and nuclei by open circles. The electron spin of the e-center (grey) is denoted by S_1 and the electron spin of the P_4^0 donor (black) is denoted by S_2. The nuclear spin of the P_4^0 donor is denoted by I_2 and nuclear spins of other atoms (e.g. ^{31}P of a diamagnetic P_3^0 state) are denoted by I_1. a) e-center/P_4^0 spin pair with S_1 coupled to an additional nucleus (e.g. ^{29}Si, ^{1}H or ^{31}P). b) Isolated e-center/P_4^0 spin pair. Both electron spins are coupled to the nuclear spin of the P_4^0 donor.

2.7.2.1 Energy levels and transitions of an e-center/P_4^0 spin pair coupled to an additional nuclear spin

The spin Hamiltonian of a correlated e-center (electron spin S_1) and P_4^0 (electron spin S_2) spin pair with one nuclear spin $I_1 = 1/2$ coupled to $S_1 = 1/2$ via an anisotropic hyperfine interaction tensor $\boldsymbol{A}$ and one nuclear spin $I_2 = 1/2$ coupled to $S_2 = 1/2$ via an isotropic hyperfine interaction $A_{\mathrm{iso}}^{\mathrm{P}}$ is given by [21]

$$\begin{aligned}\mathcal{H}_0 &= \Omega_{S_1} S_{1z} + \Omega_{S_2} S_{2z} + (\omega_{\mathrm{dd}} - J)\, 2S_{1z}S_{2z} - (J + \omega_{\mathrm{dd}}/2)\left(S_1^+ S_2^- + S_1^- S_2^+\right) \\ &\quad + AS_{1z}I_{1z} + BS_{1z}I_{1x} + \omega_{I_1} I_{1z} + A_{\mathrm{iso}}^{\mathrm{P}} S_{2z}I_{2z} + \omega_{I_2} I_{2z} \end{aligned} \tag{2.38}$$

where $\Omega_{S_i} = g_i \mu_B B_0/\hbar$ is the resonance frequency of spin S_i, ω_{dd} and J denote dipolar and exchange electron-electron coupling while ω_{I_i} denotes the free nuclear Larmor precession frequency of nuclear spin I_i. $A = A_{zz}$ and $B = \sqrt{A_{zx}^2 + A_{zy}^2}$ are the secular and the pseudo-secular hyperfine interaction between S_1 and I_1 as defined in section 2.4.

For a weakly coupled spin pair

$$\Delta\Omega = |\Omega_{S_1} - \Omega_{S_2}| \gg |J + \omega_{\mathrm{dd}}/2| \tag{2.39}$$

the flip-flop term $\left(S_1^+ S_2^- + S_1^- S_2^+\right)$ in eq. 2.38 can be neglected and we obtain a simplified form of the spin Hamiltonian [21]

$$\begin{aligned}\mathcal{H}_0^{\mathrm{w}} &= \Omega_{S_1} S_{1z} + \Omega_{S_2} S_{2z} + (\omega_{\mathrm{dd}} - J)\, 2 S_{1z} S_{2z} \\ &\quad + A S_{1z} I_{1z} + B S_{1z} I_{1x} + \omega_{I_1} I_{1z} + A_{\mathrm{iso}}^{\mathrm{P}} S_{2z} I_{2z} + \omega_{I_2} I_{2z}.\end{aligned} \tag{2.40}$$

At first sight the assumption of a weakly coupled spin pair seems to be unjustified, due to the rather small difference of Zeeman energies of the investigated paramagnetic centers. This difference is typically below 20 MHz for X-Band frequencies (9 GHz, 0.35 T, $g \approx 2$), hence intermediate electron-electron couplings render the weak-coupling condition (cf. Eq. 2.39) invalid. Nevertheless we give two reasons why the assumption of a weakly coupled spin pair is valid in most cases considered in this work.

1. In correlated spin pairs the transition probability from any state to states with a certain singlet content is strongly suppressed as the electron-electron coupling exceeds the difference in resonance frequencies of the individual spins [47]. Since the EDMR signal is proportional to this transition probability, only weakly-coupled spin-pairs are visible in EDMR. This is also in accordance with coherent Rabi-oscillations measured by pulsed EDMR [50, 51].

2. If the individual spins of a spin pair exhibit similar g-values and one of the spins is strongly coupled to a nuclear spin via isotropic hyperfine interaction (e.g.: e-centers and P_4^0-donors in n-type a-Si:H) its resonance frequency is shifted. In this case we can restrict the discussion to one nuclear sublevel of I_2 (e.g. $m_{I_2} = +\frac{1}{2}$) and combine the $A_{\mathrm{iso}}^{\mathrm{P}} S_{2z} I_{2z}$ term with the electron spin Zeeman term in Eq. 2.40 to introduce a new effective spin Hamiltonian

$$\mathcal{H}_0^{\mathrm{eff}} = \Omega_{S_1} S_{1z} + \Omega_{S_2} S_{2z} + (\omega_{dd} - J)\, 2 S_{1z} S_{2z} + A S_{1z} I_{1z} + B S_{1z} I_{1x} + \omega_{I_1} I_{1z} \tag{2.41}$$

where $\Omega_{S_2} = g_2 \mu_B B_0/\hbar + A_{\mathrm{iso}}^{\mathrm{P}}/2$. If $A_{\mathrm{iso}}^{\mathrm{P}}$ is sufficiently large, the weak-coupling condition (cf. Eq. 2.39) will be fulfilled.

$\mathcal{H}_0^{\mathrm{w}}$ can be diagonalized with the unitary transformation

$$\mathcal{H}_0^{\mathrm{w}} \xrightarrow{\xi I_{1y}+\eta 2 S_{1z} I_{1y}} \mathcal{H}_0^{\mathrm{d}} \tag{2.42}$$

with the angles $\eta = (\eta_\alpha - \eta_\beta)/2$, $\xi = (\eta_\alpha + \eta_\beta)/2$ and

$$\begin{aligned} \eta_\alpha &= \arctan\left(\tfrac{-B}{A+2\omega_{I_1}}\right) \\ \eta_\beta &= \arctan\left(\tfrac{-B}{A-2\omega_{I_1}}\right) \quad . \end{aligned} \tag{2.43}$$

The diagonal form of the spin Hamiltonian then takes the following form

$$\begin{aligned} \mathcal{H}_0^{\mathrm{d}} &= \Omega_{S_1} S_{1z} + \Omega_{S_2} S_{2z} + (\omega_{dd} - J)\, 2 S_{1z} S_{2z} \\ &\quad + \frac{\omega_+}{2} I_{1z} + \frac{\omega_-}{2} 2 S_{1z} I_{1z} + A_{\mathrm{iso}}^{\mathrm{P}} S_{2z} I_{2z} + \omega_{I_2} I_{2z} \end{aligned} \tag{2.44}$$

with $\omega_+ = \omega_{12} + \omega_{34}$ and $\omega_- = \omega_{12} - \omega_{34}$, where

$$\begin{aligned} \omega_{12} &= \left(\omega_{I_1} + \tfrac{A}{2}\right) \cos\eta_\alpha - \tfrac{B}{2} \sin\eta_\alpha \\ \omega_{34} &= \left(\omega_{I_1} - \tfrac{A}{2}\right) \cos\eta_\beta + \tfrac{B}{2} \sin\eta_\beta \quad . \end{aligned} \tag{2.45}$$

By $\omega_\alpha = |\omega_{12}|, \omega_\beta = |\omega_{34}|$ we denote the absolute values of the ENDOR frequencies

$$\begin{aligned} \omega_\alpha &= \sqrt{\left(\omega_{I_1} + \frac{A}{2}\right)^2 + \frac{B^2}{4}} \\ \omega_\beta &= \sqrt{\left(\omega_{I_1} - \frac{A}{2}\right)^2 + \frac{B^2}{4}} \end{aligned} \tag{2.46}$$

For the 16 energy eigenvalues we obtain

$$
\begin{aligned}
|\,1+\rangle, |\,1-\rangle : \epsilon_{1+,1-} &= \frac{\Omega_{S_1}+\Omega_{S_2}}{2} + \frac{(\omega_{\mathrm{dd}}-J)}{2} \pm \frac{A^{\mathrm{P}}_{\mathrm{iso}}}{4} \pm \frac{\omega_{I_2}}{2} + \frac{\omega_{12}}{2} \\
|\,2+\rangle, |\,2-\rangle : \epsilon_{2+,2-} &= \frac{\Omega_{S_1}+\Omega_{S_2}}{2} + \frac{(\omega_{\mathrm{dd}}-J)}{2} \pm \frac{A^{\mathrm{P}}_{\mathrm{iso}}}{4} \pm \frac{\omega_{I_2}}{2} - \frac{\omega_{12}}{2} \\
|\,3+\rangle, |\,3-\rangle : \epsilon_{3+,3-} &= \frac{\Omega_{S_1}-\Omega_{S_2}}{2} - \frac{(\omega_{\mathrm{dd}}-J)}{2} \mp \frac{A^{\mathrm{P}}_{\mathrm{iso}}}{4} \pm \frac{\omega_{I_2}}{2} + \frac{\omega_{12}}{2} \\
|\,4+\rangle, |\,4-\rangle : \epsilon_{4+,4-} &= \frac{\Omega_{S_1}-\Omega_{S_2}}{2} - \frac{(\omega_{\mathrm{dd}}-J)}{2} \mp \frac{A^{\mathrm{P}}_{\mathrm{iso}}}{4} \pm \frac{\omega_{I_2}}{2} - \frac{\omega_{12}}{2} \\
|\,5+\rangle, |\,5-\rangle : \epsilon_{5+,5-} &= \frac{-\Omega_{S_1}+\Omega_{S_2}}{2} - \frac{(\omega_{\mathrm{dd}}-J)}{2} \pm \frac{A^{\mathrm{P}}_{\mathrm{iso}}}{4} \pm \frac{\omega_{I_2}}{2} + \frac{\omega_{34}}{2} \\
|\,6+\rangle, |\,6-\rangle : \epsilon_{6+,6-} &= \frac{-\Omega_{S_1}+\Omega_{S_2}}{2} - \frac{(\omega_{\mathrm{dd}}-J)}{2} \pm \frac{A^{\mathrm{P}}_{\mathrm{iso}}}{4} \pm \frac{\omega_{I_2}}{2} - \frac{\omega_{34}}{2} \\
|\,7+\rangle, |\,7-\rangle : \epsilon_{7+,7-} &= \frac{-\Omega_{S_1}-\Omega_{S_2}}{2} + \frac{(\omega_{\mathrm{dd}}-J)}{2} \mp \frac{A^{\mathrm{P}}_{\mathrm{iso}}}{4} \pm \frac{\omega_{I_2}}{2} + \frac{\omega_{34}}{2} \\
|\,8+\rangle, |\,8-\rangle : \epsilon_{8+,8-} &= \frac{-\Omega_{S_1}-\Omega_{S_2}}{2} + \frac{(\omega_{\mathrm{dd}}-J)}{2} \mp \frac{A^{\mathrm{P}}_{\mathrm{iso}}}{4} \pm \frac{\omega_{I_2}}{2} - \frac{\omega_{34}}{2}
\end{aligned}
\tag{2.47}
$$

where the plus and minus signs refer to the orientation of I_2 ($m_{I_2} = \pm 1/2$). For the eigenstates in the Cartesian product basis we find

$$
\begin{aligned}
|\,1+\rangle &= \cos\left(\frac{\eta_\alpha}{2}\right) |{\uparrow_{S_1}}{\uparrow_{S_2}}{\uparrow_{I_1}}\rangle\, |{\uparrow_{I_2}}\rangle - \sin\left(\frac{\eta_\alpha}{2}\right) |{\uparrow_{S_1}}{\uparrow_{S_2}}{\downarrow_{I_1}}\rangle\, |{\uparrow_{I_2}}\rangle \\
|\,2+\rangle &= \sin\left(\frac{\eta_\alpha}{2}\right) |{\uparrow_{S_1}}{\uparrow_{S_2}}{\uparrow_{I_1}}\rangle\, |{\uparrow_{I_2}}\rangle + \cos\left(\frac{\eta_\alpha}{2}\right) |{\uparrow_{S_1}}{\uparrow_{S_2}}{\downarrow_{I_1}}\rangle\, |{\uparrow_{I_2}}\rangle \\
|\,3+\rangle &= \cos\left(\frac{\eta_\alpha}{2}\right) |{\uparrow_{S_1}}{\downarrow_{S_2}}{\uparrow_{I_1}}\rangle\, |{\uparrow_{I_2}}\rangle - \sin\left(\frac{\eta_\alpha}{2}\right) |{\uparrow_{S_1}}{\downarrow_{S_2}}{\downarrow_{I_1}}\rangle\, |{\uparrow_{I_2}}\rangle \\
|\,4+\rangle &= \sin\left(\frac{\eta_\alpha}{2}\right) |{\uparrow_{S_1}}{\downarrow_{S_2}}{\uparrow_{I_1}}\rangle\, |{\uparrow_{I_2}}\rangle + \cos\left(\frac{\eta_\alpha}{2}\right) |{\uparrow_{S_1}}{\downarrow_{S_2}}{\downarrow_{I_1}}\rangle\, |{\uparrow_{I_2}}\rangle \\
|\,5+\rangle &= \cos\left(\frac{\eta_\beta}{2}\right) |{\downarrow_{S_1}}{\uparrow_{S_2}}{\uparrow_{I_1}}\rangle\, |{\uparrow_{I_2}}\rangle - \sin\left(\frac{\eta_\beta}{2}\right) |{\downarrow_{S_1}}{\uparrow_{S_2}}{\downarrow_{I_1}}\rangle\, |{\uparrow_{I_2}}\rangle \\
|\,6+\rangle &= \sin\left(\frac{\eta_\beta}{2}\right) |{\downarrow_{S_1}}{\uparrow_{S_2}}{\uparrow_{I_1}}\rangle\, |{\uparrow_{I_2}}\rangle + \cos\left(\frac{\eta_\beta}{2}\right) |{\downarrow_{S_1}}{\uparrow_{S_2}}{\downarrow_{I_1}}\rangle\, |{\uparrow_{I_2}}\rangle \\
|\,7+\rangle &= \cos\left(\frac{\eta_\beta}{2}\right) |{\downarrow_{S_1}}{\downarrow_{S_2}}{\uparrow_{I_1}}\rangle\, |{\uparrow_{I_2}}\rangle - \sin\left(\frac{\eta_\beta}{2}\right) |{\downarrow_{S_1}}{\downarrow_{S_2}}{\downarrow_{I_1}}\rangle\, |{\uparrow_{I_2}}\rangle \\
|\,8+\rangle &= \sin\left(\frac{\eta_\beta}{2}\right) |{\downarrow_{S_1}}{\downarrow_{S_2}}{\uparrow_{I_1}}\rangle\, |{\uparrow_{I_2}}\rangle + \cos\left(\frac{\eta_\beta}{2}\right) |{\downarrow_{S_1}}{\downarrow_{S_2}}{\downarrow_{I_1}}\rangle\, |{\uparrow_{I_2}}\rangle
\end{aligned}
\tag{2.48}
$$

To obtain the $|-\rangle$ eigenfunctions replace $|\uparrow_{I_2}\rangle$ by $|\downarrow_{I_2}\rangle$. The energy level diagram is shown in Fig. 2.15. Transition frequencies are shown in Fig. 2.17 and will be discussed in sec. 2.7.2.3.

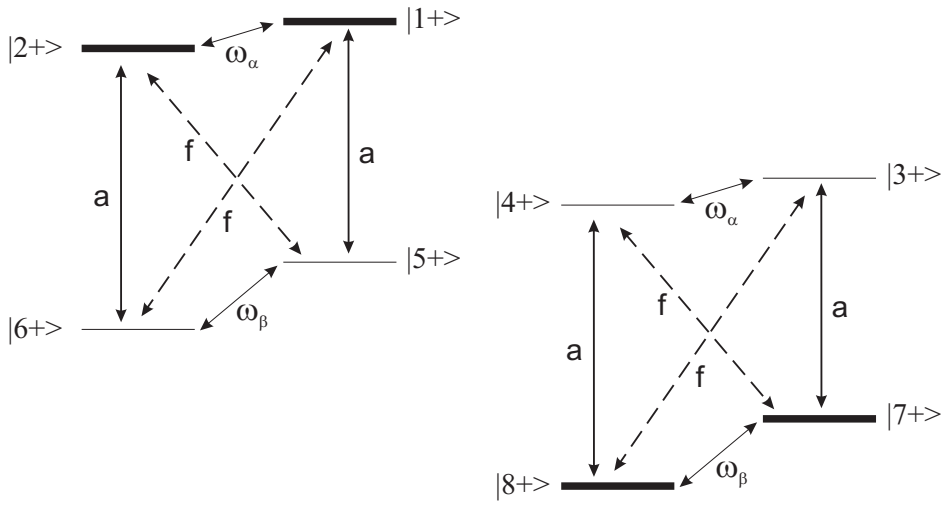

Figure 2.15: Energy level diagram of e-center/P_4^0 spin pair coupled to an additional nuclear spin. Allowed and forbidden transitions of S_1 are shown by solid and dashed arrows, respectively. Transitions of S_2 are not shown for better overview. Energy levels are shown for $|\uparrow_{I_2}\rangle$, energy levels with $|\downarrow_{I_2}\rangle$ can be derived in an analogous way.

2.7.2.2 Energy levels and transitions of an isolated e-center/P_4^0 spin pair

In the following we evaluate eigenenergies and eigenstates of a correlated electron-spin pair where both electron spins are coupled to one and the same ^{31}P nuclear spin of the P_4^0 donor state, that is $I_1 = I_2$. The spin Hamiltonian for such a spin system can be derived from Eq. 2.40 and is given by

$$\begin{aligned}\mathcal{H}_0^{\mathrm{w}} &= \Omega_{S_1} S_{1z} + \Omega_{S_2} S_{2z} + (\omega_{\mathrm{dd}} - J)\, 2 S_{1z} S_{2z} \\ &\quad + A S_{1z} I_z + B S_{1z} I_x + \omega_I I_z + A_{\mathrm{iso}}^{\mathrm{P}} S_{2z} I_z \end{aligned} \tag{2.49}$$

$\mathcal{H}_0^{\mathrm{w}}$ can be diagonalized with the unitary transformation

$$\mathcal{H}_0^{\mathrm{w}} \xrightarrow{\xi I_y+\eta 2S_{1z}I_y+\phi 4S_{1z}S_{2z}I_y+\theta 2S_{2z}I_y} \mathcal{H}_0^{\mathrm{d}} \tag{2.50}$$

with the angles $\eta = (\eta_\alpha - \eta_\beta)/2$, $\xi = (\eta_\alpha + \eta_\beta)/2$,$\phi = (\eta_\phi - \eta_\theta)/2$,$\theta = (\eta_\phi + \eta_\theta)/2$ where

$$\begin{aligned} \eta_{\alpha,\phi} &= \tfrac{1}{2}\left[\arctan\left(\tfrac{-B}{A+A^{\mathrm{P}}_{\mathrm{iso}}+2\omega_I}\right) \pm \arctan\left(\tfrac{-B}{A-A^{\mathrm{P}}_{\mathrm{iso}}+2\omega_I}\right)\right] \\ \eta_{\beta,\theta} &= \tfrac{1}{2}\left[\arctan\left(\tfrac{-B}{A-A^{\mathrm{P}}_{\mathrm{iso}}-2\omega_I}\right) \pm \arctan\left(\tfrac{-B}{A+A^{\mathrm{P}}_{\mathrm{iso}}-2\omega_I}\right)\right] \quad . \end{aligned} \tag{2.51}$$

The diagonal form of the spin Hamiltonian then takes the following form

$$\begin{aligned} \mathcal{H}_0^{\mathrm{d}} &= \Omega_{S_1}S_{1z} + \Omega_{S_2}S_{2z} + (\omega_{dd} - J)\,2S_{1z}S_{2z} \\ &\quad + \frac{\omega_{1+}}{2}I_z + \frac{\omega_{1-}}{2}2S_{1z}I_z + \frac{\omega_{2+}}{2}2S_{2z}I_z + \frac{\omega_{2-}}{2}4S_{1z}S_{2z}I_z \end{aligned} \tag{2.52}$$

with the nuclear frequencies $\omega_{12}, \omega_{34}, \omega_{56}$ and ω_{78}, and

$$\begin{aligned} \omega_{1+} &= \frac{1}{2}(\omega_{12} + \omega_{34} + \omega_{56} + \omega_{78}) \\ \omega_{1-} &= \frac{1}{2}(\omega_{12} + \omega_{34} - \omega_{56} - \omega_{78}) \\ \omega_{2+} &= \frac{1}{2}(\omega_{12} - \omega_{34} + \omega_{56} - \omega_{78}) \\ \omega_{2-} &= \frac{1}{2}(\omega_{12} - \omega_{34} - \omega_{56} + \omega_{78}) \quad . \end{aligned} \tag{2.53}$$

The eight energy eigenvalues are

$$
\begin{aligned}
|1\rangle : \epsilon_1 &= \frac{\Omega_{S_1} + \Omega_{S_2}}{2} + \frac{(\omega_{dd} - J)}{2} + \frac{\omega_{12}}{2} \\
|2\rangle : \epsilon_2 &= \frac{\Omega_{S_1} + \Omega_{S_2}}{2} + \frac{(\omega_{dd} - J)}{2} - \frac{\omega_{12}}{2} \\
|3\rangle : \epsilon_3 &= \frac{\Omega_{S_1} - \Omega_{S_2}}{2} - \frac{(\omega_{dd} - J)}{2} + \frac{\omega_{34}}{2} \\
|4\rangle : \epsilon_4 &= \frac{\Omega_{S_1} - \Omega_{S_2}}{2} - \frac{(\omega_{dd} - J)}{2} - \frac{\omega_{34}}{2} \\
|5\rangle : \epsilon_5 &= \frac{-\Omega_{S_1} + \Omega_{S_2}}{2} - \frac{(\omega_{dd} - J)}{2} + \frac{\omega_{56}}{2} \\
|6\rangle : \epsilon_6 &= \frac{-\Omega_{S_1} + \Omega_{S_2}}{2} - \frac{(\omega_{dd} - J)}{2} - \frac{\omega_{56}}{2} \\
|7\rangle : \epsilon_7 &= \frac{-\Omega_{S_1} - \Omega_{S_2}}{2} + \frac{(\omega_{dd} - J)}{2} + \frac{\omega_{78}}{2} \\
|8\rangle : \epsilon_8 &= \frac{-\Omega_{S_1} - \Omega_{S_2}}{2} + \frac{(\omega_{dd} - J)}{2} - \frac{\omega_{78}}{2}
\end{aligned}
\tag{2.54}
$$

with the eigenfunctions

$$
\begin{aligned}
|1\rangle &= \cos\left(\frac{\eta_\alpha + \eta_\phi}{2}\right) |\uparrow_{S_1}\uparrow_{S_2}\uparrow_I\rangle - \sin\left(\frac{\eta_\alpha + \eta_\phi}{2}\right) |\uparrow_{S_1}\uparrow_{S_2}\downarrow_I\rangle \\
|2\rangle &= \sin\left(\frac{\eta_\alpha + \eta_\phi}{2}\right) |\uparrow_{S_1}\uparrow_{S_2}\uparrow_I\rangle + \cos\left(\frac{\eta_\alpha + \eta_\phi}{2}\right) |\uparrow_{S_1}\uparrow_{S_2}\downarrow_I\rangle \\
|3\rangle &= \cos\left(\frac{\eta_\alpha - \eta_\phi}{2}\right) |\uparrow_{S_1}\downarrow_{S_2}\uparrow_I\rangle - \sin\left(\frac{\eta_\alpha - \eta_\phi}{2}\right) |\uparrow_{S_1}\downarrow_{S_2}\downarrow_I\rangle \\
|4\rangle &= \sin\left(\frac{\eta_\alpha - \eta_\phi}{2}\right) |\uparrow_{S_1}\downarrow_{S_2}\uparrow_I\rangle + \cos\left(\frac{\eta_\alpha - \eta_\phi}{2}\right) |\uparrow_{S_1}\downarrow_{S_2}\downarrow_I\rangle \\
|5\rangle &= \cos\left(\frac{\eta_\beta + \eta_\theta}{2}\right) |\downarrow_{S_1}\uparrow_{S_2}\uparrow_I\rangle - \sin\left(\frac{\eta_\beta + \eta_\theta}{2}\right) |\downarrow_{S_1}\uparrow_{S_2}\downarrow_I\rangle \\
|6\rangle &= \sin\left(\frac{\eta_\beta + \eta_\theta}{2}\right) |\downarrow_{S_1}\uparrow_{S_2}\uparrow_I\rangle + \cos\left(\frac{\eta_\beta + \eta_\theta}{2}\right) |\downarrow_{S_1}\uparrow_{S_2}\downarrow_I\rangle \\
|7\rangle &= \cos\left(\frac{\eta_\beta - \eta_\theta}{2}\right) |\downarrow_{S_1}\downarrow_{S_2}\uparrow_I\rangle - \sin\left(\frac{\eta_\beta - \eta_\theta}{2}\right) |\downarrow_{S_1}\downarrow_{S_2}\downarrow_I\rangle \\
|8\rangle &= \sin\left(\frac{\eta_\beta - \eta_\theta}{2}\right) |\downarrow_{S_1}\downarrow_{S_2}\uparrow_I\rangle + \cos\left(\frac{\eta_\beta - \eta_\theta}{2}\right) |\downarrow_{S_1}\downarrow_{S_2}\downarrow_I\rangle
\end{aligned}
\tag{2.55}
$$

where

$$
\begin{aligned}
\omega_{12} &= (\omega_I + \frac{A + A^{\mathrm{P}}_{\mathrm{iso}}}{2})\cos(\eta_\alpha + \eta_\phi) - \frac{B}{2}\sin(\eta_\alpha + \eta_\phi) \\
\omega_{34} &= (\omega_I + \frac{A - A^{\mathrm{P}}_{\mathrm{iso}}}{2})\cos(\eta_\alpha - \eta_\phi) - \frac{B}{2}\sin(\eta_\alpha - \eta_\phi) \\
\omega_{56} &= (\omega_I - \frac{A - A^{\mathrm{P}}_{\mathrm{iso}}}{2})\cos(\eta_\beta + \eta_\theta) + \frac{B}{2}\sin(\eta_\beta + \eta_\theta) \\
\omega_{78} &= (\omega_I - \frac{A + A^{\mathrm{P}}_{\mathrm{iso}}}{2})\cos(\eta_\beta - \eta_\theta) + \frac{B}{2}\sin(\eta_\beta - \eta_\theta). \qquad (2.56)
\end{aligned}
$$

The energy levels are shown in Fig. 2.16. The transition frequencies are shown in Fig. 2.17 and will be discussed in the next section.

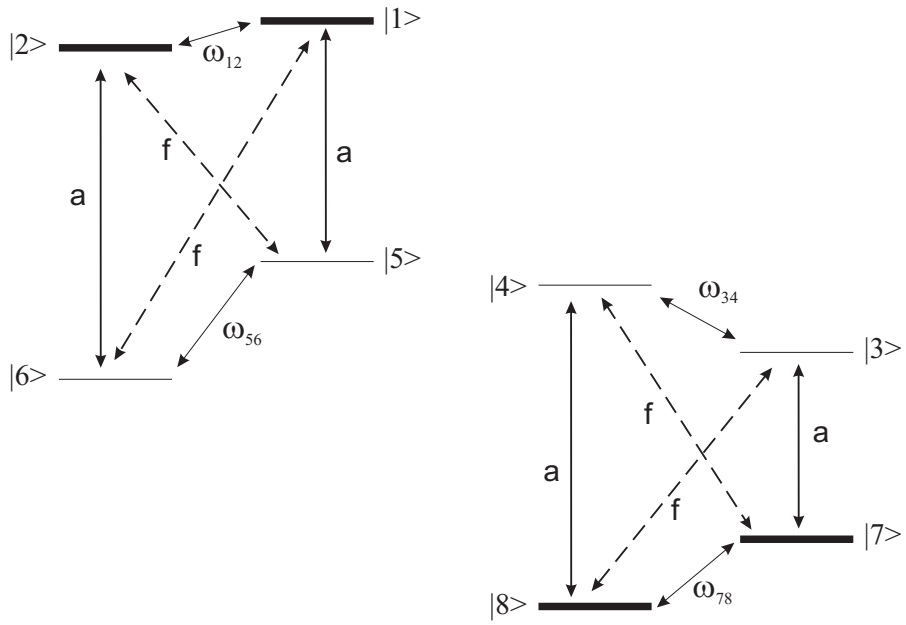

Figure 2.16: Energy level diagram of an isolated e-center/P_4^0 spin pair. Only allowed (a) and forbidden (f) transitions of S_1 are shown. The energy level diagram is drawn for $|A| < |2\omega_I|$ and $0 < \omega_{\mathrm{dd}}$, J, A, $B < A^{\mathrm{P}}_{\mathrm{iso}}$, $g_1 \approx g_2$, $\omega_I < 0$, as it is expected for isolated e-center/P_4^0 spin pairs.

2.7.2.3 ESEEM detected by pulse EDMR

In the preceding section we discussed eigenstates and spin transitions of an e-center/P_4^0 spin pair in a thin-film solar cell. The two electron spins are coupled to magnetic nuclei in their vicinity and a measurement of these HFIs yields a detailed microscopic picture of the spin density distribution of the paramagnetic defects or impurities. The HFIs can be determined since they induce oscillations of the primary-echo intensity generated by a modified two-pulse ESE sequence $\pi/2 - \tau - \pi - \tau - \text{echo}(\pi/2)$. In order to determine a relation between oscillation frequencies and HFIs, the observable change of the photocurrent at the time of echo formation has to be evaluated. This can be done by using Eq. 2.36 and Eq. 2.37 derived in sec. 2.7.2.

Before we discuss the result of this calculation, the spin transitions of an isolated e-center/P_4^0 spin pair and an e-center/P_4^0 spin pair coupled to an additional nuclear spin have to be compared. The transition frequencies in the form of a schematic EDMR spectrum are shown in Fig. 2.17. In both cases the large $A_{\text{iso}}^{\text{P}}$ between S_2 and I_2 is much larger than the difference in g-value of both spin partners and the allowed spin flip transitions of S_1 are well separated from those of S_2 and can be excited selectively. Fig. 2.17 a) shows the transition frequencies of an e-center/P_4^0 spin pair where S_1 is coupled to an additional nuclear spin. In that case the forbidden transitions of S_1 and the additional nuclear spin are close to the allowed transitions of S_1. Using a strong microwave pulse it is possible to excite forbidden and allowed transitions of S_1 without selecting transitions of S_2. The simultaneous excitation of forbidden and allowed transitions is a prerequisite for ESEEM [21]. By solving Eq. 2.36 and Eq. 2.37 we obtain for this particular case the following echo modulation formula $I_{2p}(\tau)$

$$I_{2\text{p}}(\tau) \;=\; 1 - \frac{k}{4}\left(2 - 2\cos\omega_\alpha\tau - 2\cos\omega_\beta\tau + \cos\omega_+\tau + \cos\omega_-\tau\right) \qquad (2.57)$$

with the modulation amplitude $k = \sin^2 2\eta$. This result is identical to the well-known two-pulse echo-modulation function in conventional EPR-ESEEM [21]. Since the involved nuclear frequencies ω_α and ω_β contain the HFIs between S_1 and I_1, the spin density distribution of the excited spin S_1 can be determined.

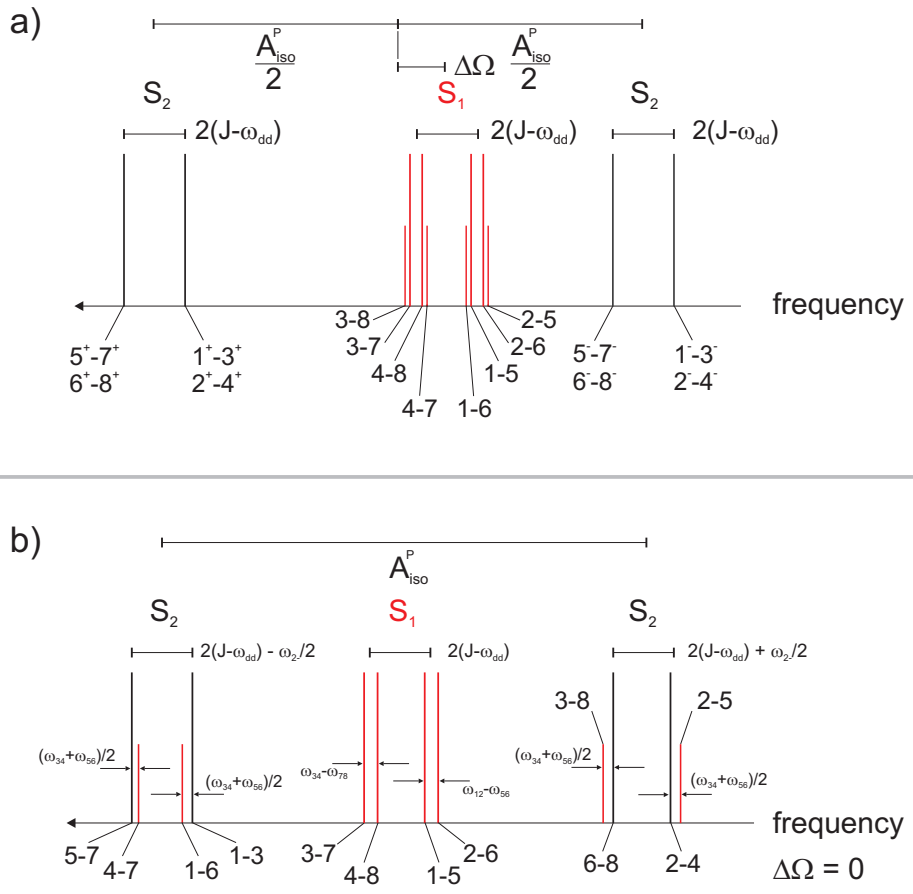

Figure 2.17: Schematic EDMR spectrum with allowed and forbidden transitions of a correlated spin pair. Transition amplitudes of allowed and forbidden transitions are indicated by the length of the vertical lines. Spin-flip transitions of S_1 are shown in red, transitions of S_2 are shown in black. Transitions between eigenstates $|i\rangle$ and $|j\rangle$ are denoted by $i-j$ and the brackets are omitted for better readability. Parameters: B_0 = 0.35 T ω_{dd} = 0 MHz, J = 50 MHz, A^P_{iso} =800 MHz, A = 20 MHz. a) spin pair coupled to an additional nuclear spin. Parameters of the spin system: , g_1 = 2.0044, g_2 = 2.02, B = 15 MHz, ω_{I_1} = 15 MHz, ω_{I_2} = 6 MHz. b) Isolated spin pair with one nuclear spin coupled to both electron spins. Forbidden transitions of S_2 are not shown. Parameters of the spin system: $g_1 = g_2$ = 2.0044, B = 3 MHz, ω_I = 15 MHz.

In case of an isolated e-center/P_4^0 spin pair with one nuclear spin coupled to both electron spins the situation is much more complex. The forbidden transitions of S_1 are now well separated from allowed S_1 transitions, since flip of a nuclear spin requires a large amount of energy (A_{iso}^{P}) (cf. Fig. 2.17b). It is therefore impossible to excite S_1 and S_2 selectively and the theoretical treatment of the pulse sequence becomes complicated. However, in the particular case of an e-center/P_4^0 spin pair with a large A_{iso}^{P} between S_2 and I_2 a simultaneous excitation of allowed and forbidden transitions is impossible due to the limited experimental excitation bandwidth of conventional microwave pulses (10 $ns^{-1} \approx 100$ MHz) and ESEEM does not arise. These findings can be generalized to any situation where the nucleus of interest exhibits an anisotropic HFI to the excited electron spin but is also strongly coupled to another non-excited electron spin. In other words, nuclear spins which are part of a non-excited paramagnetic center (strong HFI) do not give rise to ESEEM.

3 Materials and Methods

In the following chapter, details of the sample preparation protocols, the EPR measurement routines and the applied DFT methods are summarized.

3.1 Materials

Application of EPR and EDMR techniques to investigate defect states in thin-film silicon solar cells requires special sample preparation protocols since thin-film silicon solar modules and even lab-scale cells are too large in size to be placed in EPR resonators. The area of the cell has to be reduced to 1x1 mm^2 by laser scribing or by photolithography due to the small size of the resonators. For EDMR a special contacting scheme was developed to connect the small cell with the external current detection circuit. Solar cells with an area of 1x1 mm^2 and a thickness of the layer of about 1 μm do not contain enough defect states to meet the sensitivity requirements of EPR. To investigate the different layers (e.g. the absorber layer, i-layer in p-i-n solar cells) of the solar cell structure by EPR, it is mandatory to isolated the layers from the cell and to prepare separate films of these layers on adopted substrates. This is usually done by depositing only the layer of interest on a large (10 x 10 cm^2) area and then collecting the material in powder form. By this technique the sample mass can be increased by four orders of magnitude. To investigate degradation effects of the solar cell materials by light, the samples have to be illuminated by a standardized degradation protocol.

3.1.1 a-Si:H powder samples

Undoped a-Si:H samples were deposited at Forschungszentrum Jülich with Plasma-enhanced Chemical Vapor Deposition (PECVD) at 185 °C from gas mixture of silane and hydrogen on a 10 cm x 10 cm Al foil substrate [52, 53]. The silane concentration

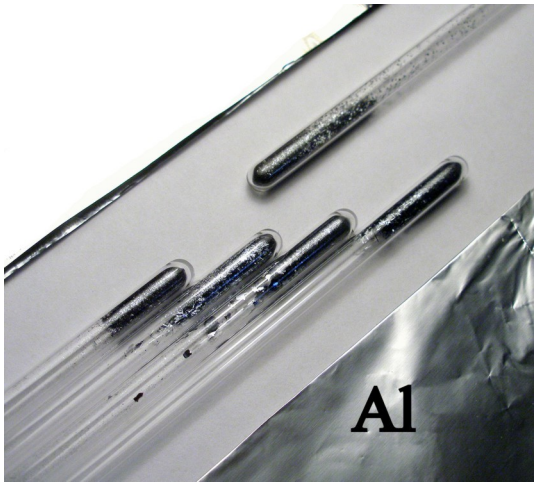

Figure 3.1: Sample preparation: The a-Si:H thin film were deposited on Al-foil. After etching with diluted hydrochloric acid, the a-Si:H powder samples were collected and sealed in EPR quartz tubes. Photo courtesy of Forschungszentrum Jülich.

defined by the ratio of the process gas flow $SC = SiH_4/(SiH_4 + H_2)$ was varied from 10 to 100% to obtain material of different electronic quality [54]. A selection of a-Si:H samples investigated in this thesis is given in Table 3.1. The different initial defect density of the samples in the as-deposited state reflects the fact that the samples exhibit different electronic quality. However, as will be analyzed in detail in chapter 4 and 5, the EPR parameters of the different a-Si:H samples are only minor affected by a variation of the deposition conditions.

It is known that a-Si:H typically contains 10 at. % hydrogen [10, 55]. The films were removed from the substrate by diluted hydrochloric acid and the flakes were collected in EPR quartz tubes. To provide thermal contact of the sample with the coolant during low-temperature measurements and to avoid oxidation, the EPR quartz tubes are filled with 0.5 bar He gas and sealed afterwards.

3.1.2 Light soaking and thermal annealing

Light soaking was performed while the films were still on the Al-foil substrate to guarantee a homogeneous degradation of the a-Si:H sample. After light soaking the samples were removed from the substrate as described above. Degradation was performed with a

a-Si:H sample	$SiH_4/(SiH_4 + H_2)$	as-deposited N_s [cm^{-3}]	light soaked N_s [cm^{-3}]
A (08B455)	100 %	$3.2 \cdot 10^{16}$	-
B (08B191)	10 %	$\approx 10^{15}$	$4.6 \cdot 10^{16}$
C (09C345)	100 %	$4.3 \cdot 10^{16}$(annealed)	$5.3 \cdot 10^{16}$

Table 3.1: Undoped a-Si:H powder samples studied in this thesis. $SiH_4/(SiH_4 + H_2)$ indicates the precursor gas dilution with H_2. Typical errors for the defect density are 30 % [56]. For completeness, the laboratory name of the samples is listed in parenthesis.

conventional sun simulator under AM1.5 and 50°C substrate temperature for 400h - 1000h at Forschungszentrum Jülich.

In order to reverse the SWE, the powder samples were thermally annealed at 200 °C for 2h in a furnace. The powder samples are annealed inside sealed EPR quartz tubes, which are filled with 0.5 bar He gas. In the case of device-grade samples prepared with a silane concentration of SC = 10 %, the defect density decreases by about a factor of 10. In case of sample C (non-device grade sample - high deposition rate) the defect density decreases only by $1 \cdot 10^{16} cm^{-3}$ during annealing. H effusion from the samples at 200 °C is therefore negligible since annealing decreases the defect density for all samples.

3.1.3 µc-Si:H thin-film silicon solar cells

Thin-film silicon p-i-n solar cells were deposited at the Forschungszentrum Jülich using PECVD on Corning glass [52, 57, 58]. The cells consist of a layer stack with 150 nm ZnO:Al TCO, boron-doped p-µc-Si:H, 1 µm intrinsic µc-Si:H absorber, phosphorus-doped n-a-Si:H emitter, ZnO and silver as a back contact. The phosphorus and boron dopant concentration is estimated to be 1.5 at. % and 0.2 at. %, respectively. The solid-phase hydrogen concentration in µc-Si:H and a-Si:H is known to be about 10 at. % [10, 55].

The deposited solar cells and the metallic contact are patterned by laser scribing to achieve a solar cell area of about 1x1 mm^2 (cf. Fig. 3.2). The contact leads are prepared in long stripes to contact the solar cell outside of the EPR resonator.

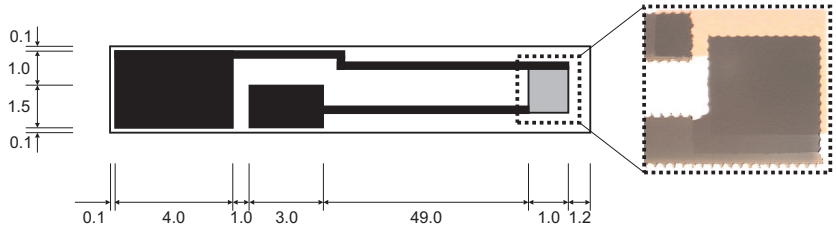

Figure 3.2: Contact geometries of µc-Si:H thin-film silicon solar cells used for pulse EDMR measurements. Contact lines and pads consisting of 100 to 200 nm silver are indicated by the black areas. The active area of the solar cell is shown by the grey area. Optical micrograph from this part of the sample is shown in the enlarged section on the right side of the figure. All dimensions are in mm.

3.2 Methods

3.2.1 EPR measurements

Pulse and continuous wave (c.w.) EPR spectroscopy were carried out on commercial Bruker BioSpin ElexSys spectrometers at various frequencies:

- S-Band: Pulse EPR spectroscopy at S-band was performed on a Bruker BioSpin ElexSys E580 spectrometer equipped with a Super-S FT upgrade and a 4118S-MS5 probe head. The spectrometer is located at the Freie Universität Berlin.

- X-Band: The pulse and c.w. experiments at X-band were done using a Bruker BioSpin ElexSys E580 spectrometer. For pulse EPR measurements the ER4118X-MD5 probe head is used. c.w. EPR spin-counting measurements were done in a Super High-Q cavity resonator (Q = 8000) and the Bruker spin-counting routine. The spectrometer is located at the Helmholtz-Zentrum Berlin in Adlershof.

- Q-Band: The EPR spectra at Q-band were acquired with an ElexSys E580 spectrometer and had a Super-Q FT upgrade and a probe head home built by FU Berlin (Friedhelm Lendzian and Christian Teutloff). The spectrometer is located at the Freie Universität Berlin.

- W-Band: The pulse EPR measurements at W-band were performed on an ElexSys E680 with a Teraflex EN600-1021H resonator. Temperature control was realized

with CF935 helium bath cryostats and ITC503 temperature controllers from Oxford Instruments. The spectrometer is located at the Freie Universität Berlin.

A determination of the defect density in a-Si:H powder samples was carried out by counting the spins in a X-Band c.w. EPR experiment [56]. The amplitude of the absorption signal was calibrated with a highly diluted (2,2,6,6-tetramethylpiperidin-1-yl)oxidanyl (TEMPOL) in toluol solution [56]. All spectrometers are equipped with a microwave-pulse forming unit (MPFU) producing the low power microwave pulses, which are amplified before they interact with the sample. The MPFU provides at least four pulse channels, where each channel produces microwave pulses with different phases relative to the reference arm. The phase settings are denoted by +x, -x, +y and -y [21].

Fig. 3.3 shows the EPR pulse sequences applied in this thesis. The following provides short overview of the various pulse sequences and their purpose. For some pulse sequences, the application of phase-cycling steps is mandatory in order to filter out unwanted signal contributions [59].

1. The 2-pulse ESE sequence, generating a primary echo, is used to measure the field-swept echo detected EPR spectrum (fixed τ), the transversal relaxation properties by the primary-echo decay (incrementing τ) and ESEEM modulations on the primary-echo decay (incrementing τ). For a correct determination of the primary-echo decay, the phase of the initial $\pi/2$ pulse has to cycled (+x, -x), otherwise resonator ring-down can interfere with the signal.

2. The Inversion recovery sequence is used to measure the longitudinal relaxation of the electron spin after the initial inversion pulse (π-pulse). The signal recovery as delay time T increases is monitored by a 2-pulse ESE sequence. Very often the excitation band width of the initial microwave pulse is not sufficient to excite the complete EPR resonance line, and additional echoes can occur. To remove these signals a four-step phase cycling sequence was applied (cf. Table 3.2).

3. The 3-pulse ESE sequence generates a stimulated echo after the last microwave pulse [21]. The pulse sequence can be used to measure longitudinal relaxation (incrementing T at fixed τ) and transversal relaxation (increasing τ at fixed T). When incrementing T at fixed τ, the decay of the stimulated echo can be used to measure ESEEM (3-pulse ESEEM). Several echoes besides the stimulated echo

Inversion Recovery			3-pulse ESE		
1: π	2: $\pi/2$	3: π	1: $\pi/2$	2: $\pi/2$	3: $\pi/2$
+x	+x	+x	+x	+x	+x
+x	-x	+x	-x	+x	+x
-x	+x	+x	+x	-x	+x
-x	-x	+x	-x	-x	+x

Table 3.2: Phase-cycling steps of inversion recovery and 3-pulse ESE sequence.

can occur in a 3-pulse ESE sequence. To remove these signals a four-step phase cycling sequence was applied (cf. Table 3.2).

4. The Davies ENDOR sequence is similar to the inversion recovery sequence, but has an additional intense RF-pulse applied during the delay time T. The RF pulse flips the nuclear spin by π and therefore redistributes spin populations among the eigenstates of the spin systems. Please refer to sec. 2.5 for details about the physics of the ENDOR mechanism. Experimental details are described in the next section.

3.2.2 Pulsed Davies ENDOR

To determine the hyperfine coupling between paramagnetic defects and magnetic nuclei experimentally, pulsed ENDOR experiments have been performed at a microwave frequency of 34 GHz (Q-band) and a temperature of 80 K. The measurements were carried out on a Bruker Elexsys E580 spectrometer at FU Berlin equipped with a Amplifier Research 250A250A RF amplifier and a home-built Q-band ENDOR resonator. The ENDOR spectra were recorded with the Davies ENDOR pulse sequence $\pi - T - \pi/2 - \tau - \pi - \tau -$ echo with delay times $T = 22\,\mu s$ and τ = 400 ns. The excitation bandwidth of the initial microwave preparation pulse can be varied by increasing its length while decreasing its power to keep the flip-angle constant at π. The RF-pulse during the delay time T was applied for 19 μs. All ENDOR spectra were recorded in stochastic mode [60], where the RF is varied randomly with a shot repetition time of 2 ms. The random RF pattern resulted in an excellent baseline stability by avoiding heat-

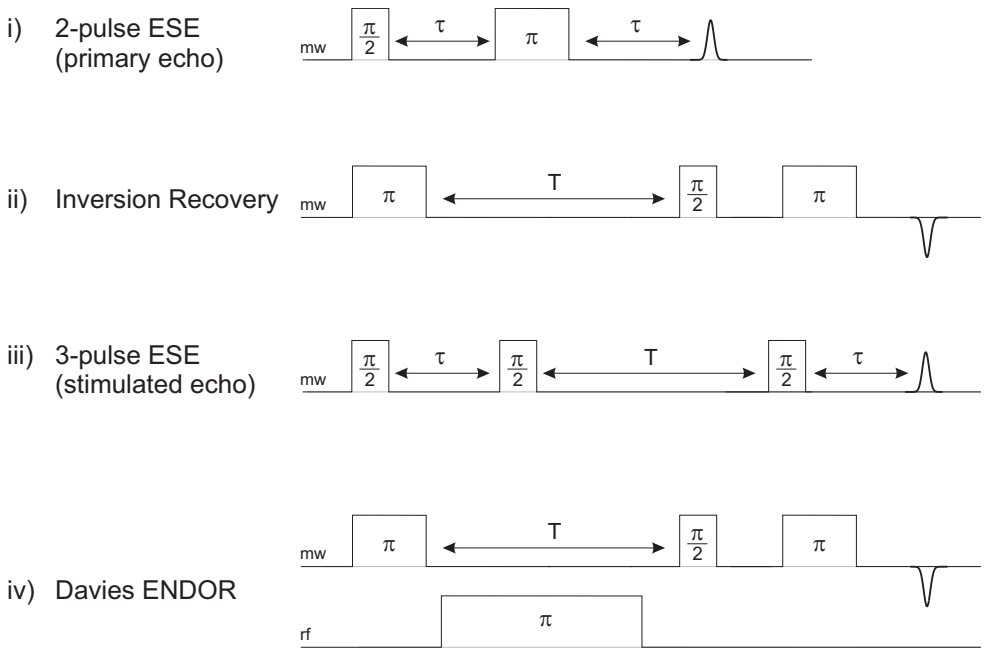

Figure 3.3: Electron-spin echo (ESE) microwave pulse sequences applied in this thesis. (i) 2-pulse ESE sequence, (ii) inversion recovery, (iii) 3-pulse ESE sequence and (iv) Pulse Davies-ENDOR sequence.

ing artifacts and prevented asymmetric ENDOR intensities due to nuclear spin relaxation effects [61].

3.2.3 EDMR measurements

Pulse EDMR measurements were carried out on a modified EPR spectrometer based on a commercial Bruker E580 spectrometer operating at 9.5 GHz. The commercially available spectrometer was augmented with a homebuilt current detection circuit (cf. Fig. 3.4). The EDMR solar cell sample was placed inside a standard dielectric ring resonator (Bruker ER 4118X-MD5) and cooled to a temperature of 10 K by a He-flow cryostat. The solar cell sample is electrically connected to an external voltage source and a transient current amplifier manufactured by the Elektronik-Manufaktur Mahlsdorf. The solar cell was illuminated with a halogen lamp (50 mW/cm^2) and biased in reverse direction (U_s = - 1.0 V) by applying a constant voltage generating a steady-state photocurrent I_{ph} = 17 µA. The static external magnetic field is generated by an electromagnet. Changes of the photocurrent induced by resonant microwave pulses (ν_{mw} = 9.5 MHz) are amplified

by the transient current amplifier (cf. enlarged view in the lower part of Fig. 3.4). The microwave pulses were amplified by a 1kW TWT amplifier to achieve a $\pi/2$ - pulse length ($S = 1/2$) of 16 ns. The transient changes of the photocurrent are subject to low-pass filtering by the RC-time constant of the sample. In addition, the transient current change is processed by an analog bandpass filter after current amplification. Finally the amplified and filtered signal is read into the spectrometer software by a transient recorder (8 bit analog-to-digital converter).

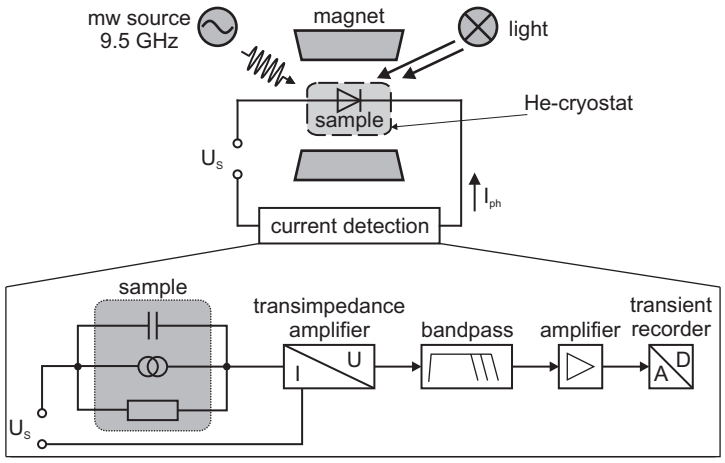

Figure 3.4: Pulse EDMR setup based on a commercial EPR spectrometer. The sample can be illuminated with a light source through an optical window of the resonator. For details see text.

Due to the fact that the described current detection setup has a rather large bandwidth of about 1 MHz, the transient signals are strongly affected by electromagnetic interference (EMI). Weak disturbances from the environment coupling to the electrical circuit can be avoided by using a symmetric current detection implemented in the above described current amplifier. Strong electromagnetic disturbances originate from the TWT amplifier, which could only be avoided by moving the TWT device away from the detection circuit with a distance larger than 2 m.

3.2.4 Density-functional theory calculations

The DFT calculations were performed by Christoph Freysoldt and Gernot Pfanner at the Max-Planck-Institut für Eisenforschung in Düsseldorf. DFT calculations were carried

out with a plane-wave pseudopotential formalism implemented in the Quantum Espresso package [62]. We used norm-conserving, scalar-relativistic Troullier-Martins pseudopotentials and the PBE exchange-correlation functional. A plane-wave energy cutoff of 30 Ry ensures convergence with respect to the basis set. The Brillouin zone integration is done on a 6×6×6 Monkhorst-Pack mesh. The HFIs of all atoms in the supercell are determined from a PAW-like post processing step from the self-consistent calculation [63] using two projectors per 1-channel. Please note that the HFIs of ^{29}Si nuclear spins are mostly negative, since the nuclear g-value of ^{29}Si (g_n = -1.1106) is negative. The g-tensor is computed by the GI-PAW formalism [64]. We consider 27 a-Si:H models consisting of 64 silicon and 8 hydrogen atoms. The defect-free a-Si:H models were created either by releasing hydrogen into WWW-models of a-Si [65] or by heating and gradually annealing of c-Si:H models [66]. DBs were generated from these models by removing one of the hydrogen atoms, followed by structural relaxation.

4 The microscopic nature of native coordination defects in a-Si:H

A determination of the microscopic structure of paramagnetic coordination defects in a-Si:H is mandatory for a deeper understanding of the electronic properties of the material since the defects form deep traps for excess charge carriers in the mobility gap. The defects therefore degrade the photoconductivity and efficiency of solar cell devices based on this material. Theoretical models which account for the generation of these defect during the deposition process explicitly assume that the dominant defect center is a threefold-coordinated Si atom, a dangling-bond (DB) [17, 18]. In this chapter the microscopic nature of paramagnetic coordination defects in a-Si:H is investigated by multifrequency EPR. The improved spectral resolution at high magnetic field reveals a rhombic splitting of the g-tensor with the following principal values: g_x = 2.0080, g_y = 2.0060 and g_z = 2.0033 and shows pronounced g-strain, i.e. the principal values are widely distributed. The multi-frequency approach furthermore yields precise ^{29}Si hyperfine data. In order to translate the experimental EPR parameters into a structural model on the atomic level, DFT calculations on 27 computer generated a-Si:H DB models were carried out. These yielded g-values close to the experimental data but deviating hyperfine interaction values. It is shown that paramagnetic coordination defects in a-Si:H are more delocalized than computer-generated DB defects and models to explain this discrepancy will be discussed.

4.1 Introduction

The performance of thin-film solar cells and other devices based on hydrogenated amorphous silicon (a-Si:H) is limited by localized defect states in the mobility gap, which act as recombination centers for excess charge carriers. In undoped a-Si:H, the defect centers

are paramagnetic and give rise to an inhomogeneously broadened asymmetric EPR line at around g = 2.0050 - 2.0055 [19]. The intensity of this signal is routinely used as a measure for the electronic quality of a-Si:H [67]. The impact of these defect centers on the efficiency of solar cells is even aggravated by the fact that the defect concentration significantly increases upon light exposure [14] (light-induced degradation - SWE [8, 9]). In order to reduce the a-Si:H defect density in the initial and stabilized state after light soaking, optimized deposition protocols have been developed [10]. Despite these improvements, a nanoscopic understanding of the processes leading to the creation of light-induced defects is still missing [13]. A detailed knowledge about the microscopic origin of these defect centers is therefore mandatory for a deeper understanding of the electronic properties of a-Si:H. There has been a controversial debate in the literature as to whether the dominating defects in a-Si:H originate from threefold-coordinated Si atoms, giving rise to dangling-bond (DB) defects, or from fivefold-coordinated Si atoms, giving rise to floating-bond (FB) defects [19, 68]. To decide between the two alternative defect models, EPR techniques are most valuable, since the EPR spectrum reflects the electronic structure of the paramagnetic defect. In the present case, the EPR spectrum is determined by two interactions, the Zeeman interaction given by the g-tensor, and the hyperfine interaction (HFI) between the unpaired electron spin and nuclear spins of close-by H and Si atoms. While the g-tensor reflects the global electronic structure of the paramagnetic defect, HFIs probe the defect wave function locally. Combining these two pieces of information detailed spin-density maps of the unpaired electron spin may be obtained, which constitute highly desired information to identify the microscopic origin of the defect centers. A detailed analysis of the EPR spectrum of the coordination defects was first carried out by Stutzmann et al. at X-band frequency [19]. They determined the g-tensor of the unpaired electron spin to be axially symmetric with principal values similar to the P_b center observed at the Si/SiO_2 interface [69, 70] (cf. Table 4.1). In a subsequent study, Umeda et al. [71] revised the g-tensor values by studying the EPR spectrum at different resonance frequencies (S-, X- and Q-band) with increased spectral resolution (cf. Table 4.1). However, in both studies the symmetry of the the g-tensor was already assumed as axially symmetric in their fitting models and never systematically tested against rhombic symmetry. In addition to the g-tensor, Stutzmann et al. [19] determined the HFI with the nuclear spin of the Si atom where most of the

defect spin density is concentrated. The HFI of this particular atom is characterized by an anisotropic tensor, which will be denoted by $\boldsymbol{A_L}$ in the following, i.e. the A-tensor with the largest isotropic HFI. By analyzing the principal values of this tensor within an analytical linear combination of atomic orbitals (LCAO) model [72], Stutzmann et al. [19] determined the wave function of the defect. Since their analysis of the HFI suggests that the sp^x-hybridized defect wave function is of strong p-character, the authors concluded that the electronic structure of the given center resembles a DB similar to the P_b center. However, the isotropic HFI (A_{iso}) of coordination defects in a-Si:H, as evaluated by Stutzmann and Biegelsen [19, 73], is given by A_{iso} = 200 MHz and is therefore much smaller than the isotropic HFI of the P_b center (A_{iso} = 315 MHz) [74]. This discrepancy was attributed to a relaxation of the atomic structure of the DB from a tetrahedral configuration to a more planar geometry, induced by the amorphous environment. It was argued that in the latter configuration the p-character of the DB wave function is enhanced over the s-character, which leads to a smaller isotropic HFI. It is however not a priori clear whether such a relaxation actually takes place when a DB is created in a-Si:H. This question can only be clarified by a detailed quantitative theoretical treatment of the atomic DB structure and the resulting EPR parameters, which is still missing up to now. The possibility to compare experimental g- and A-tensors in amorphous semiconductor materials with theoretical calculations came into reach only recently. This was mainly due to two reasons. Firstly, precise g-tensor data is usually only available for crystalline materials and secondly, a lack of ab-initio approaches capable of calculating g-tensors from complex material structures. This situation changed with the advent of advanced density functional theory (DFT) methods, which proved to be able to reproduce experimentally determined g-tensors even in complex Si materials [64, 75]. Up to now such studies have been restricted to crystalline Si materials. One of the purposes of this study is to extend this powerful approach to a-Si:H. Here, we present a detailed experimental and theoretical analysis of the g-tensor and the HFIs of the dominant defect center in a-Si:H. We employ high resolution EPR measurements and complement them by density functional theory (DFT) calculations capable of relating the measured g- and A-tensors to the spin-density distribution, binding geometry and the electrostatic surrounding of the paramagnetic site. The defects in a-Si:H are studied experimentally by multi-frequency EPR (S-band: 3.6 GHz/0.13 T, X-band: 9.7 GHz/0.34 T, Q-band:

34 GHz/1.2 T and W-band: 94 GHz/3.35 T). In the absence of field-dependent line broadening mechanisms and at high signal to noise ratio (S/N), a high frequency spectrum is in principle enough to determine the principal values of the g- and A-tensors as well as their relative orientation. In the present case however, pronounced site-to-site variations of the principal g-values (g-strain) restrict the determination of the principal A-values at high resonance frequencies. This limitation can be circumvented by the multi-frequency approach, which allows to separate field-independent ($\boldsymbol{A}$) and field-dependent ($\boldsymbol{g}$) spectral contributions. The HFIs are thereby best resolved at low magnetic fields and corresponding frequencies (S-band and X-band), while the principal values of the g-tensor can be best determined at high frequencies (Q-band and W-band). Furthermore we applied field-swept echo-detected EPR (FSE) instead of the previously used continuous wave (c.w.) EPR. FSE-EPR resolves broad, tailing spectral features better than c.w. EPR techniques. g- and A-values are extracted from the experimental FSE spectra by a robust simultaneous fitting procedure. As a result we show that the g-tensor symmetry of the localized defect is rhombic and therefore lower than axial symmetry as claimed in earlier studies [19, 71]. This result is important to improve the reliability and precision of g-tensor values and provides the basis for detailed studies of the correlation between the material properties and $\boldsymbol{g}$ [54, 76]. Improved g-tensor values may also help to determine structural differences between light-induced and native defects and thereby shed new light on the physical processes underlying the SWE. In order to see whether or not the experimentally determined g- and A-values are adequately described by the atomistic DB model, we employed 27 a-Si:H models, each containing a single DB defect. The g- and A-values of each DB model were then calculated by DFT methods.

4.2 Experimental details

The material investigated in this chapter is an undoped a-Si:H sample in the as-deposited state (sample A) (cf. sec. 3.1.1). The experiments were carried out at different microwave frequencies (S-band, X-band, Q-band and W-band, respectively) at a temperature of 80 K. To measure the EPR spectrum a typical field-swept ESE pulse sequence (FSE) ($\pi/2 - \tau - \pi - \tau -$ echo) is utilized with a π - pulse of 52 ns, 32 ns, 80 ns, 128 ns and an interpulse delay τ of 400 ns, 250 ns, 400 ns, 300 ns at S-, X-, Q- and

W-band, respectively. FSE spectra were independent of τ (data not shown) and the shot-repetition time was set long enough to avoid a saturation of the spin system (> 2ms). Details about the DFT calculations are given in sec. 3.2.4.

4.3 Results and Discussion

Fig. 4.1 depicts FSE spectra of a-Si:H powder samples taken at different microwave frequencies (S-band, X-band, Q-band and W-band, respectively) at a temperature of 80 K. In the left column (Fig. 4.1 a-d) experimental spectra taken at the indicated frequency bands are shown (crosses) together with simulations obtained with the parameters given in Table 4.1 (red solid lines) and the difference between experiment and fit (black solid line at the bottom).

In the right column (Fig. 4.1 e-h) simulated FSE spectra in the absence of g-, A-strain and broadening due to unresolved HFIs are shown, to make the impact of $\boldsymbol{g}$ and $\boldsymbol{A}$ on the line shape at different resonance frequencies more obvious. In the following we will first qualitatively assign the frequency dependent line shapes to the dominating magnetic interactions. Secondly we describe the fitting routine applied to quantitatively extract the principal g- and A-values. Finally we compare these parameters with values derived from DFT calculations on computed a-Si:H DB models.

4.3.1 Analysis of experimental spectrum

The S- and X-band spectra (cf. Fig. 4.1 a,b) consist of an intense central line and two less intense satellite peaks (cf. enlarged spectral regions in Fig. 4.1). Si enrichment studies showed that the EPR spectrum is subject to isotope effects, since naturally abundant Si is composed of stable non-magnetic isotopes ($^{28}/^{30}$Si) with a total abundance of 95.32 %, and one stable magnetic isotope (^{29}Si) with an abundance of 4.68 % [73]. If the immediate vicinity of the defect is depleted from magnetic isotopes (^{29}Si and ^{1}H) large HFIs are absent, resulting in the narrow central line, which is broadened by unresolved HFI to ^{1}H and ^{29}Si nuclear spins [71, 77]. This broadening of the resonance line is well-described by a Lorentzian in the central part of the line (cf. Fig. 4.1 S-band spectrum) and its width is proportional to the abundance of ^{29}Si, p, for $p < 10$ % [71]. In cases, however, where the unpaired electron spin is mainly located on ^{29}Si atoms

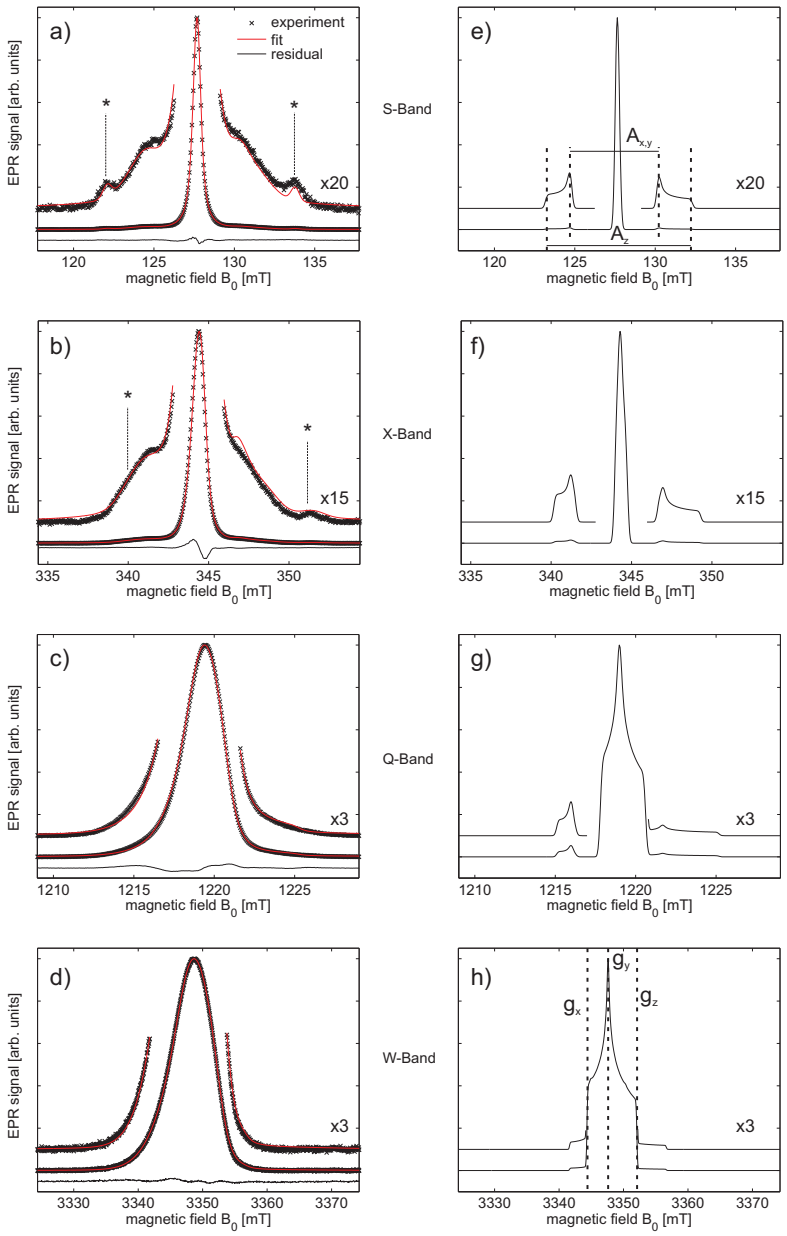

Figure 4.1: S-/X-/Q- and W-Band field-swept echo EPR spectra of defects in a-Si:H (g = 2.0055) at a temperature of 80 K. Each spectrum was recorded by integrating the primary echo of a ($\pi/2 - \tau - \pi - \tau -$ echo) pulse sequence. Left column (a-d): experimental spectra (crosses) and the fitted spectra (red solid line) obtained with the model described in the text. In addition to the coordination defects, another EPR signal with $g = 1.9975$ is observed, marked by (*). The residual between the experimental spectra and the fit is shown by the black solid line at the bottom. Spectra are offset vertically for clarity. Right column (e-h): fitted spectra without g-strain, A-strain and isotropic magnetic field broadening. Principal values of the A_L-tensor and the g-tensor are indicated by horizontal and vertical lines in e) and h), respectively.

the EPR spectrum is dominated by strong HFI (> 150 MHz, equivalent to > 7 mT) giving rise to satellite formation in the EPR spectrum. These satellites are symmetrically centered about the narrow central line (cf. Fig. 4.1 a and e). However, the satellites are already at S-band frequencies significantly broadened by site-to-site disorder resulting in a distribution of ^{29}Si HFIs (A-strain), which hampers the precise determination of the ^{29}Si HFIs. Upon increasing the resonance frequency, the central line and the satellites exhibit increasing asymmetric line broadening, which may be attributed to g-anisotropy and -strain. Therefore, the satellites, which are still resolved at X-band frequencies, overlap with the central line at Q- and W-band. Two points regarding the spectral evolution with increasing frequency are important to note. First, there is no resolution of the principal g-values, i.e. the g-tensor, due to the fact that g-strain proportional to the resonance frequency limits the resolution, even at very high frequencies (cf. Fig. 4.1 d and h). Second, the fact that the satellites are not observable at higher frequencies makes it impossible to extract the magnetic parameters at one single frequency.

4.3.2 EPR signal from paramagnetic impurity

Overlapping the previously observed coordination defects (g = 2.0055), we found an additional spectral contribution in the S- and X-Band EPR spectra (marked by (*) in Fig. 4.1 a, b) which, to the best of the authors knowledge, was not observed before due to limited S/N of previous measurements. At S-Band frequencies, this signal is split in two narrow HFI components, which are symmetrically centered around a g-value of $g_{\|}$ = 1.9975. This deviation from the g-value of the coordination defects clearly shows that the signal centered around $g_{\|}$ must be assigned to an additional paramagnetic site and cannot be ascribed to additional HFI components of the coordination defects. The large HFI indicates that the paramagnetic center is located on an impurity atom, like H or N. The center cannot be located on a Si atom, since non-magnetic Si isotopes would give rise to an intense central line at $g_{\|}$, which is not observed. The most abundant magnetic nuclei of H or N are ^{1}H with a nuclear spin of I = 1/2 and ^{14}N with a nuclear spin of I = 1, giving rise to either two or three EPR lines, respectively. At present it is impossible to distinguish between these two cases since the central ^{14}N-HFI line would overlap with the much more intense central line of the coordination defects. However, for both isotopes the HFIs and the g-value can be directly extracted from the EPR spectrum. In case the

center is associated with ^{1}H the HFI is $\approx$ 320 MHz and in case of ^{14}N half this value, i.e. $\approx$ 160 MHz. At X-Band the impurity signal is still observable but shifted to higher magnetic field relative to the central line, due to the lower g-value. In addition, the signal starts to broaden due to the growing influence of g-strain. At Q- and W-Band frequencies the impurity signal is completely buried under the main spectral contribution.

4.3.3 Fitting model

The EPR signal may be described by the following spin Hamiltonian ($\mathcal{H}$) of a single electron spin ($S = 1/2$) coupled to j surrounding nuclei:

$$\mathcal{H} = \mu_B \boldsymbol{B}_0 \boldsymbol{g} \boldsymbol{S}/\hbar + \sum_j \mu_N g_{jn} \boldsymbol{B}_0 \boldsymbol{I}_j/\hbar + \sum_j \boldsymbol{S} \boldsymbol{A}_j \boldsymbol{I}_j \tag{4.1}$$

$\boldsymbol{g}$ and $\boldsymbol{A}$ are 3x3 matrices with the principal values (g_x, g_y, g_z) and (A_x, A_y, A_z), respectively. Their respective principal axes systems are not necessarily collinear.

Due to the presence of strong g- and A-strain, the dominating A- and g-values cannot be extracted from the EPR spectra directly. Instead simultaneous simulations of the EPR spectra based on Eq. 4.1 have to be performed. Since the spin system is sufficiently dilute only one electron spin needs to be included in the calculations. In that case the Zeeman term in Eq. 4.1 can be solved exactly with the three principal values of the g-tensor as fit parameters. The magnetic-field dependent broadening induced by g-strain is explicitly included in the simulation as an uncorrelated gaussian distribution of the principal values. This procedure has the advantage that the distribution parameters can be extracted directly from the fitting routine and are therefore separated from magnetic-field independent broadening. In contrast to the Zeeman term, the treatment of the HFI term in Eq. 4.1 is more complicated, because an exact simulation including all nuclei is impossible. We therefore introduce a fitting model with certain approximations. The HFI term in Eq. 4.1 is usually divided into two terms

$$\mathcal{H}_{\mathrm{HFI}} = \sum_{k=1}^{n} \boldsymbol{S} \boldsymbol{A}_k \boldsymbol{I}_k + \sum_{j \neq k} \boldsymbol{S} \boldsymbol{A}_j \boldsymbol{I}_j \tag{4.2}$$

where the first term describes the resolved HFI, for which the EPR resonance positions are calculated explicitly in the simulation. The second term describes the unresolved

HFI which leads to a broadening of the magnetic resonance line and is described by an empirical broadening function. This is a very convenient procedure, since the first term usually involves only a few nuclei, while the second term runs over a very large number of nuclei. The shape of the broadening function is usually well-described by one or two-parameter functions like a Gaussian, Lorentzian or Voigtian line shapes [78–80] which can be fitted to the resonance line by parameter adjustment. In addition to unresolved HFIs, paramagnetic centers in the solid-state experience additional line broadening due to electron-electron spin-spin interaction and life-time broadening due to T_1 and T_2 mechanisms. However, for the low defect concentrations and the low temperatures used in this study both of these mechanisms contribute less than 1 μT to the line width and are therefore negligible [81, 82]. This approximation is furthermore supported by the experimental observation that the line width of the broadening function is directly proportional to the ^{29}Si content of a-Si:H [71]. We can therefore conclude that the broadening function is dominated by unresolved HFIs. It is important to note that due to the low natural abundance of ^{29}Si ($p \ll 100$ %) the central line portion of the broadening function has approximately a Lorentzian and not a Gaussian shape [71, 80]. As in earlier studies we use a fitting model, where only one ^{29}Si nuclear spin is treated explicitly (n = 1 in Eq. 4.2, $\boldsymbol{A}_1 = \boldsymbol{A}_\mathrm{L}$). The broadening function due to unresolved HFI by the residual nuclei is modeled by a Voigtian line broadening function [19,71]. In addition, we limit the number of fitting parameters by introducing several prior assumptions for the symmetry of the A_L-tensor and the orientation between the g- and A_L-tensor. Since the satellites are strongly affected by inhomogeneous broadening it is difficult to test the symmetry of the A_L-tensor against rhombicity. Furthermore the relative orientation between the A_L- and g-tensor and its distribution cannot be determined independently, so we simply assume that both tensors are collinear with g_z and A_z being parallel. In addition, we simulated the observed impurity-related signal and added its EPR spectrum linearly to the main contribution in the EPR spectrum. In the simulations we assumed that the impurity spectrum originates from ^{1}H. This assumption leads to additional uncertainty in the central region of the spectra. However, due to the fact that the integrated intensity of this contribution would be less than 1 %, the presence of the impurity in the EPR spectra has only minor influence on the determination of the EPR parameters of the coordination defects, which are the main subject of the present publication.

4.3.4 Multifrequency Fit

To extract the A and g-values we applied the following step-wise fitting routine. In a first step, the Q- and W-band spectra were fitted simultaneously by adjusting the distribution parameters of the three principal g-values (mean value and standard deviation). In a second step, the S- and X-band spectra were fitted by adjusting the distribution parameters of the A_L-tensor principal values, where we again assumed independent normal distributions. In a third step, the S-band spectrum was fitted by adjusting a convolutional Voigtian line broadening function accounting for inhomogeneous broadening by unresolved HFI. In a fourth step, the S- and X-band spectra were fitted by adjusting the g-tensor, g-strain, A_{iso} and the integral intensity of the ^{1}H impurity. The four steps were repeated in a loop until convergence is reached. The simulations of the individual solid-state EPR spectra were performed with EasySpin, a MATLAB® (The Mathworks, Natick, MA, USA) toolbox [25]. The toolbox calculates the resonance field positions by matrix diagonalization or second-order perturbation theory, transition intensities are computed by first-order perturbation theory. The powder spectra are evaluated by considering a large set of different orientations uniformly distributed over the unit sphere. The simulated spectra are fitted to the experimental spectra by non-linear least-squares fitting based on the Levenberg-Marquardt algorithm.

4.3.5 Fit results

The fit results for a rhombic g-tensor are shown as solid lines in Fig. 4.1 a-d. In earlier publications it was explicitly assumed that the g-tensor is axially symmetric, i.e. $g_x = g_y = g_\perp$and $g_z = g_{||}$. In order to test this, we performed two separate multifrequency fits. In the first fit the symmetry of the g-tensor is forced to axial symmetry and in the second fit (Fig. 4.1 a-d) no assumptions about the symmetry were made. In the first case the principal values of the g-tensor are $g_x = g_y = 2.0065$ and $g_z = 2.0042$, in very good agreement with earlier studies [71]. In the second case we obtained a rhombic g-tensor with three different principal values ($g_x = 2.0080$, $g_y = 2.0060$ and $g_z = 2.0033$). However, the quality of the fit, measured by the norm of the difference between the fitted and the experimental spectrum (χ^2), is significantly worse in the case of an axially symmetric g-tensor compared to a rhombic g-tensor (cf. Table 4.1). We

therefore conclude that coordination defects in a-Si:H exhibit a rhombic g-tensor. For the A_L-tensor we obtained A_x = A_y = 151 MHz and A_z = 257 MHz, which corresponds to A_{iso} = 186 MHz and A_{dip} = -35 MHz. These values are slightly smaller than the previously reported ones (cf. Table 4.1). The Voigtian broadening function, accounting for unresolved HFI, deviates only slightly from a pure Lorentzian function (cf. Table 4.1). For the paramagnetic impurity associated with a ^{1}H atom we obtained an isotropic g-value of g = 1.9975 with a large g-strain and an isotropic HFI of A_{iso} = 326 MHz. The concentration of this paramagnetic impurity center is about $1.8 \cdot 10^{14}$ cm^{-3} or 0.45 % of the coordination (DB) defect density. A complete overview of the various fit parameter sets including literature values is given in Table 4.1.

4.3.6 DFT investigations

In the following we compare the experimentally obtained g- and A-values of coordination defects to corresponding values obtained from DFT calculations on computer generated a-Si:H model structures, where each model exhibits a single DB defect. Theoretical modeling of DB defects in a-Si:H is a demanding task, since a large variety of atomic configurations are present in the amorphous material. In order to account for this variety we modeled a large number of different defect structures (27) and calculated the resulting g- and A-values. The aim of this approach is to link the observed g- and A-values with a particular model structure. Surprisingly we found that quite different spin density distributions result in very similar g-values.

To illustrate this finding we show the ground-state spin-densities of two computer-generated DB models together with the calculated g- and A_L-tensors in Fig. 4.2.

The first DB model (DB1) is displayed in Fig. 4.2a (g_x = 2.0091, g_y = 2.0057, g_z = 2.0024, and A_x = -291 MHz, A_y = -288 MHz, A_z = -427 MHz for the ^{29}Si A_L - tensor) and the second DB model (DB2) is shown in Fig. 4.2b) (g_x = 2.0095, g_y = 2.0065, g_z = 2.0034, and A_x = -176 MHz, A_y = -180 MHz, A_z = -236 MHz for the ^{29}Si A_L-tensor). The g-tensor symmetry of both models is clearly rhombic, while the A_L-tensor is very close to axial symmetry. Already from a superficial inspection of the two structures it becomes apparent that the wave function of DB1 is mainly localized on a single Si atom, while the wave function of DB2 is more delocalized. Despite the apparent discrepancy of the electronic structure, the g-tensor principal values of both models are almost identical.

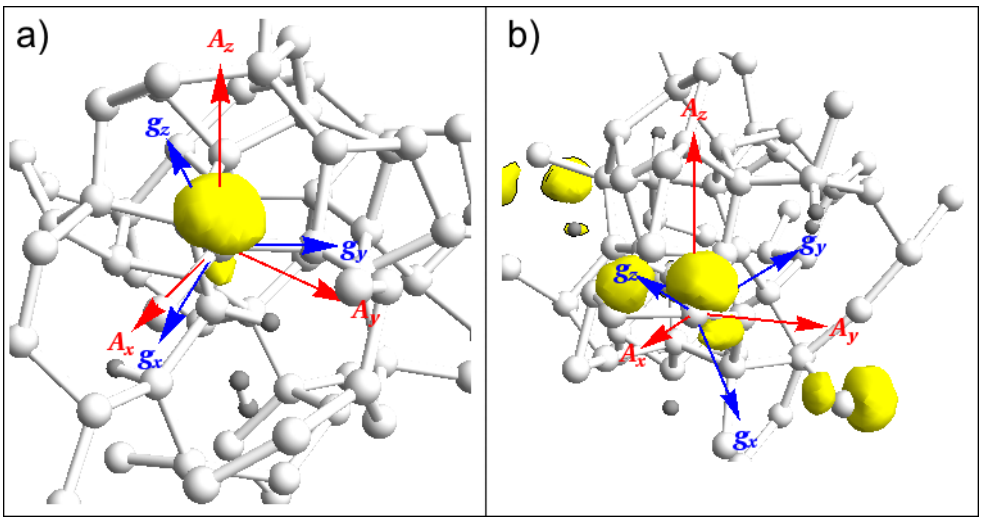

Figure 4.2: Two selected computer generated atomistic models of a DB in a-Si:H (for details see text). Principal values of $\boldsymbol{g}$ and $\boldsymbol{A}_{\mathrm{L}}$ for the two models are a) g_x = 2.0091, g_y = 2.0057, g_z = 2.0024, and A_x = -291 MHz, A_y = -288 MHz, A_z = -427 MHz, b) g_x = 2.0095, g_y = 2.0065, g_z = 2.0034, and A_x = -176 MHz, A_y = -180 MHz, A_z = -236 MHz . Atoms are indicated by light-grey (Si) and dark-grey (H) shaded spheres. Isosurface plot of the electron spin density (isosurface at 10 % of maximum spin-density value) of the trivalent silicon atom is show in yellow. Eigenvectors of the g-tensor are indicated by blue arrows and the eigenvectors of the A_{L}-tensor of the threefold-coordinated Si atom are indicated by red arrows.

Hence, widely different configurations can yield almost identical g-tensors. This effect will be discussed in more detail below. In contrast to the almost identical g-tensor, the HFI and the relative orientation between the g- and A_L-tensor vary drastically. The isotropic HFI of DB2 (A_{iso} = -197 MHz) is much smaller than the isotropic HFI of DB1 (A_{iso} = -335 MHz), which can be attributed to the delocalization of the DB wave function. The axes of the g_z and A_z principal values are nearly parallel in case of DB1 but differ significantly in case of DB2 (cf. Fig. 4.2 a,b).

Comparing the computed values for the DB1 and DB2 models with the experimental EPR data sets, we find that both the experimental and the computed principal g-values show pronounced rhombicity and that the calculated values fall within the distribution functions of the experimental g-values (within 10 % accuracy, cf. Table 4.1). In addition, the DFT results support the previously made assumption of an axially symmetric A_L-tensor for the fits of the EPR spectra in Fig. 4.1 .

We have observed that the various computer generated defect structures show a strong variation in terms of the spin-density distribution. This site-to-site disorder leads to a wide distribution of the g- and A-values (g- and A-strain). It is therefore mandatory to model a larger pool of defect structures in order to estimate the mean values and variances of the full distributions. To model this variety of defect structures, the electronic structure of a representative number of models has to be evaluated.

4.4 Defects in a-Si:H: comparing experimental values to theoretical results

4.4.1 g-tensor

In Fig. 4.3 the principal values of the g-tensor derived from the computer models are plotted together with the experimental distribution functions. The calculated values reproduce the mean experimental values, however the spread of the computed principal g-values clearly exceeds the experimental distributions. By fitting a normal distribution to the g-values, we see that the distributions for g_x, g_y and g_z peak at different values, although parts of the distributions overlap. By analyzing Fig. 4.3, it becomes clear that the g_z distribution peaks close to the free-electron g-value (g_e = 2.0023) and is

well separated from the g_x and g_y distribution. However, since there is a large overlap between the g_x and g_y distributions, it is not immediately clear whether the g_x and g_y distributions are independent or if they actually exhibit the same distribution as it would be the case for an axially symmetric g-tensor. In that case the distribution would be much wider, but still most of the g-tensors would exhibit a slight rhombic symmetry. It is therefore necessary to determine the rhombicity of each calculated g-tensor (g_x - g_y)/(g_x - g_z) separately. By doing so we found that each individual g-tensor is clearly rhombic and the distribution of (g_x - g_y)/(g_x - g_z) peaks at 0.5 which fits well to the experimentally obtained symmetry.

It appears to be surprising that the g-tensors of DB defects with a very symmetric spin-density distribution (cf. Fig. 4.2a) exhibit rhombic symmetry and not axial symmetry. This effect can be rationalized as follows. The anisotropy of the g-tensor and isotropic shifts from g_e result from an indirect coupling of the electron spin to the external magnetic field mediated by the orbital momentum. In the picture of second order perturbation theory, the most important contribution arises from the interplay of the singly-occupied DB orbital ψ_p with all the unoccupied or occupied orbitals ψ_n other than ψ_p weighted by their inverse energetic separation (cf. Eq. 2.4). Even in case of a DB orbital completely localized at the threefold coordinated Si atom the g-tensor is obviously sensitive to changes in the orientation and energies of the other orbitals. For a simplified discussion of the g-tensor anisotropy, let us assume that the singly-occupied DB orbital ψ_p is given by a perfect $|p_z\rangle$ orbital and the other orbitals $|p_{x,y}\rangle$ are also of atomic type. Defining the Cartesian coordinate system such that the z-axis coincides with the axis of the DB orbital, it is straightforward to show that the paramagnetic contribution vanishes for $\alpha\beta = zz$, since $L_z|p_z\rangle = 0$. Significant deviations from g_e are therefore only expected for $g_x \equiv g_{xx}$ and $g_y \equiv g_{yy}$ given by

$$\begin{aligned} \Delta g_{xx} = 2\frac{\langle p_z|\lambda L_x|p_y\rangle\langle p_y|L_x|p_z\rangle}{\epsilon_{p_z} - \epsilon_{p_y}} &= 2\frac{\lambda}{\epsilon_{p_z} - \epsilon_{p_y}} \\ \Delta g_{yy} = 2\frac{\langle p_z|\lambda L_y|p_x\rangle\langle p_x|L_y|p_z\rangle}{\epsilon_{p_z} - \epsilon_{p_x}} &= 2\frac{\lambda}{\epsilon_{p_z} - \epsilon_{p_x}} \end{aligned} \tag{4.3}$$

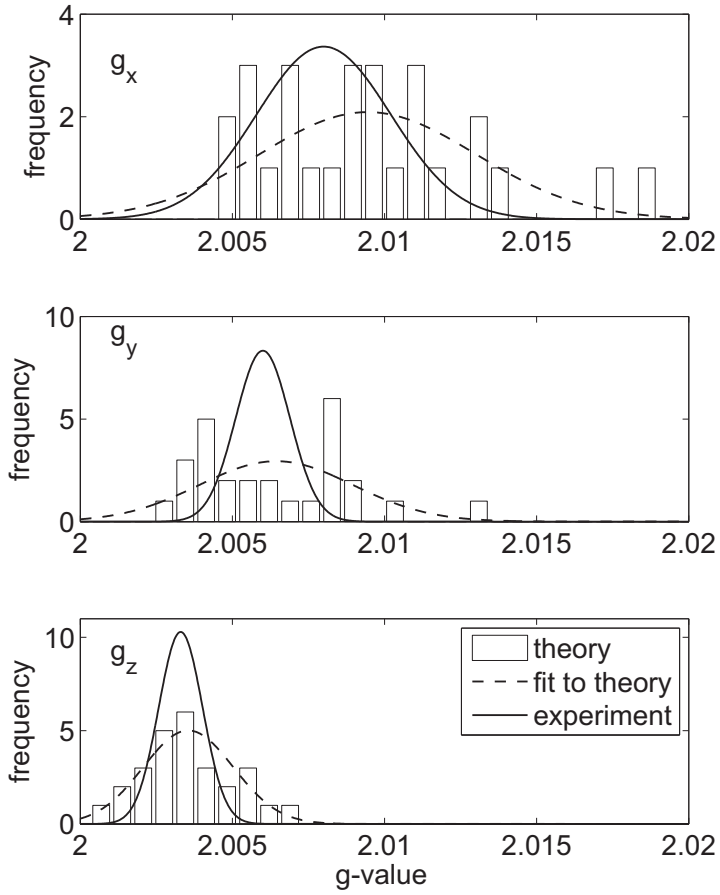

Figure 4.3: Comparison between experimentally and theoretically (DFT) obtained principal values of the g-tensor of coordination defects in a-Si:H. Values for different computer-generated models of a DB in a-Si:H are shown by the histogram. Principal values are sorted by size and assigned to g_x, g_y and g_z. The histogram was fitted by a normal distribution function shown by the dashed line. The experimental data for coordination defects obtained by a fitting model is shown by the solid line.

where we assumed that the spin-orbit coupling λ is a constant. We see that if the degeneracy of the p_x and p_y orbitals is lifted, the g_{xx} and g_{yy} values will not be degenerate. In a most disordered environment like a-Si:H one expects that the degeneracy is lifted due to fluctuations of the bond-angles and bond-length. As a result a rhombic g-tensor instead of an axially symmetric one arises. This analysis is also valid for the more realistic case of $\psi_{p,n}$ being molecular orbitals. We have seen that there is a quantitatively good agreement of the calculated g-tensors of DB models and the experimentally determined g-tensor of coordination defects in a-Si:H. However, we have shown that the g-tensor principal values are rather insensitive to the local electronic structure of the DBs. Widely different wave functions give rise to almost identical g-tensors. We now extend our analysis to the principal values of $\boldsymbol{A}_{\mathrm{L}}$, which are a more precise probe of the local spin density distribution of the defect center.

4.4.2 Hyperfine interactions

The histogram in Fig. 4.4a compares the principal A_L-values derived from the different computer generated DB models with experimentally obtained A_L-distribution functions. The distribution functions were again approximated by a normal probability density function. We found that the values derived from the calculated structures deviate from the values determined in the multifrequency fit. The calculations also lead to a larger distribution of the principal A_L-values and at the same time show larger A_x, A_y and A_z as compared to the experiment. The A_x and A_y distributions in the computer models are clearly degenerate and strongly differ from A_z. This hints towards an A-tensor close to axial symmetry. To check whether the A_x and A_y distributions of the computer models are independent or not, we determined the rhombicity $(A_x - A_y)/(A_x - A_z)$ of each set of principal values and found that the A_L-tensors for all models investigated are indeed very close to axial symmetry. The calculations revealed a rather peculiar deviation of the symmetry properties of $\boldsymbol{g}$ and $\boldsymbol{A}_{\mathrm{L}}$, where $\boldsymbol{g}$ exhibits rhombic symmetry and A_L axial symmetry. The apparent discrepancy in the symmetry properties can be rationalized as follows. The A_L-tensor depends directly on the ground state spin density and is strongly dominated by the local-orbital character (sp^x hybrid) of the DB state at the site of the trivalent Si atom. Structural variations due to the amorphous matrix affect its orientation and possibly the degree of s-p hybridization, but do not alter the fundamental sp^x

character of the DB orbital. Its axial symmetry properties are therefore maintained even in the presence of large disorder-induced fluctuations of the bond-length and bond-angles in a-Si:H. This does also hold in good approximation for the HFIs between the electron spin and nuclear spins of Si-atoms in the first and second coordination shell. We have seen that some of our defect models are actually quite delocalized. However, analyzing our defect models in more detail we see that the localized as well as the delocalized structures exhibit the typical DB characteristics of a spin-density which is mainly localized on a single atom, while the spin density on the other atoms is significantly smaller than on the central Si atom. This is reflected by the fact that the Si atoms with the second-largest HFI exhibit a smaller HFI, on average A_{iso} = -80 MHz and A_{dip} = -7 MHz (cf. Fig. 4.4b).

4.4.3 Resolved and unresolved hyperfine interactions

The most puzzling fact comparing computed and experimentally obtained magnetic interaction values is the discrepancy between the A_L-tensor obtained from DFT calculations and the multifrequency fit to the experimental data. This discrepancy is even aggravated by the fact that the experimentally obtained signal intensities in the satellite region deviate from the theoretically predicted values. In order to shed additional light on these important points we will in the following further inspect the spectral contributions arising from large ^{29}Si HFIs.

We have shown (cf. e.g. Fig. 4.1) that the low frequency EPR spectra (S-and X-band) are composed of two contributions: a central line (A), which is broadened by unresolved HFIs (second term in Eq. 4.2) and two satellite peaks (B), which are mainly due to resolved ^{29}Si HFIs (first term in Eq. 4.2; see also Fig. 4.1a and b). The number of resolved ^{29}Si HFIs is proportional to the integral of line B and will be denoted by N in the following. When we express the spectral intensity of line B (I_B) in terms of the total spectral intensity, the following equation holds

$$N = I_B/p \tag{4.4}$$

where we assumed that $p \ll 100$ %. For one ^{29}Si HFI (N = 1) one would expect I_B = 4.7 %, for two ^{29}Si HFI (N = 2) I_B = 9.4 %, etc. The spectral intensity of line B

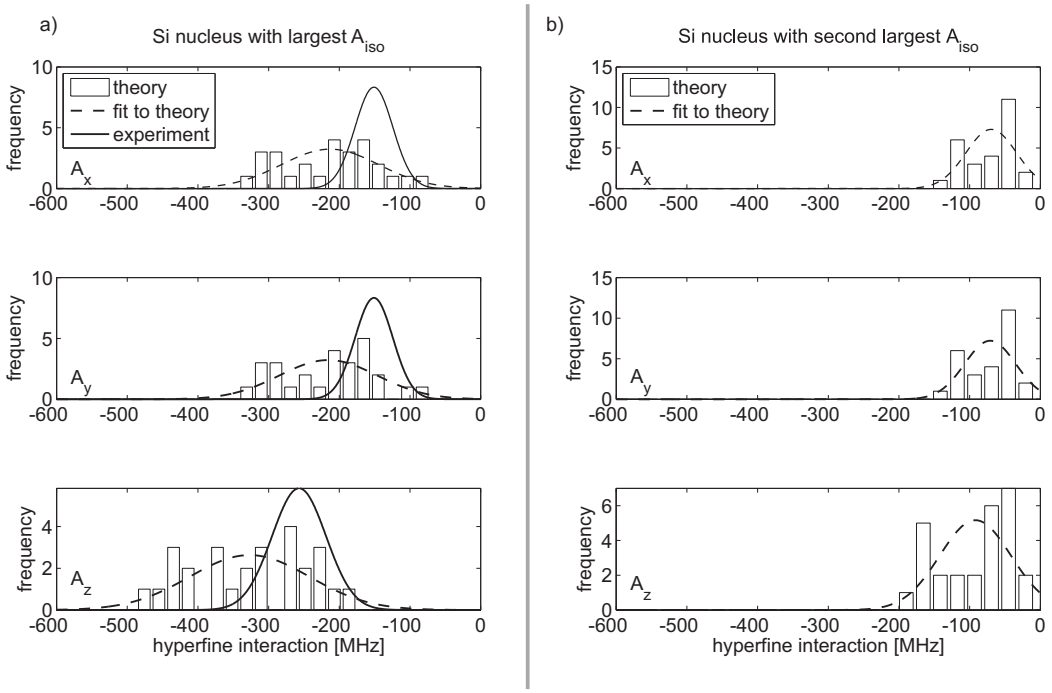

Figure 4.4: Comparison between experimentally and theoretically (DFT) obtained principal values of the largest and second-largest HFI of coordination defects in a-Si:H. A-tensor of the ^{29}Si nucleus with the largest A_{iso} (a) and second largest A_{iso} (b). Values for different computer-generated models of a DB in a-Si:H are shown by the histogram. Principal values are sorted by size and assigned to A_x, A_y and A_z. The histogram was fitted by a normal distribution function shown by the dashed line. The experimental data for coordination defects obtained by a fitting model is shown by the solid line.

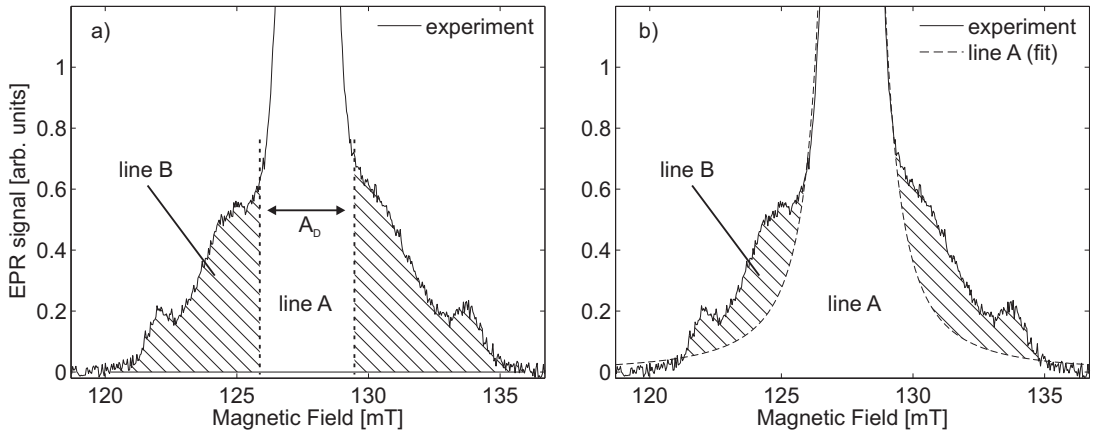

Figure 4.5: Decomposition of S-Band EPR spectrum into line A (unresolved HFIs) and line B (resolved HFIs) by two different methods. a) Dividing the lines by a demarcation HFI (A_D = 100 MHz) leads to a larger spectral intensity of line B, I_B = 10-12 % b) Assuming that the shape of line A is described by a Voigtian function leads to a smaller spectral intensity of line B, I_B = 4-5 %.

can be best analyzed at S-band frequencies where the satellite region is resolved. Proper evaluation of this spectrum is therefore a prerequisite for a precise determination of the underlying ^{29}Si HFIs. Fig. 4.5a) depicts an enlarged view of the satellite region in the S-band spectrum. In order to quantify the contribution of line A and B, we divide the EPR resonance into a central line and a satellite region by introducing a demarcation HFI of A_D = 100 MHz (dashed vertical line in Fig. 4.5a). If we now integrate over the spectral regions attributed to the respective contributions we see that line B constitutes $\approx 11 \pm 1$ % of the total spectral intensity. This estimation for line B clearly deviates from the previously reported $\approx 4 \pm 2$ % [73]. The reason for this deviation is that Stutzmann et al. [19] used a continuous and simplified broadening function for the line shape of line A, which strongly overlaps with line B (cf. Fig. 4.5b). Their estimate therefore redistributes spectral intensity from line B to line A. At first sight, the assumption of a simplified broadening function with a Lorentzian or Voigtian line shape is justified since it reproduces the central part of line A very well. However, the real line shape function may deviate from this simplified function in the satellite region. This may lead to a situation where spectral intensity belonging to line B is falsely attributed to line A and thereby lead to incorrect values for I_B and N. We have shown that the use of a step-

function (with demarcation HFI of A_D) leads to a larger spectral intensity of line B. It is therefore clear that the spectral intensity of line B strongly depends on the choice of the broadening function of line A and on the choice of A_D. Using a step-function for the line shape is without doubt a rather crude estimate since this approach does not take into account the real line shapes of signal A and B in the overlap region. The obtained signal intensity is very surprising since it does not match the value, which one assumes for a single HFI tensor. It rather suggests that the satellite spectrum consists of two large HFI tensors ($N = 2$) with a HFI > A_D. In that case the defect spin-density is distributed over two Si atoms. It is clear that this is not compatible with the DB model, where the wave function of the electron is strongly localized on a single threefold-coordinated Si atom. One intuitively expects that the spin-density on the next-nearest neighbors is much smaller, which is confirmed by the presented DFT calculations of computer generated DB models. The calculations clearly show that there is only one large ^{29}Si HFI, while the second-largest ^{29}Si HFI is on average smaller by a factor of three and therefore smaller than A_D (cf. Fig. 4.4a and b). In summary, we find that the random DB models predict one dominant hyperfine interaction centered around A_{iso} = - 250 MHz, whereas the experimental spectra would be compatible with two dominant hyperfine interactions of similar magnitude centered around A_{iso} = 180 MHz.

In order to validate this assignment and provide more accurate values for the relative signal intensities it is mandatory to model the line shapes of signal A and B in the overlap region. This is, however, only possible with additional assumptions, which may add even larger errors. In order to present a more realistic simulation, the approximate model which divides the EPR spectrum into two lines A and B has to be abandoned. The exact way to model the EPR spectrum is a simulation of the EPR spectrum on the basis of Eq. 4.1, including HFI to all nuclei surrounding the electron spin. However, such an explicit calculation is not possible since we do not know the HFI of each nucleus.

It is evident that the structural models employed for the theoretical analysis miss an important aspect of the experimentally observed defect ensemble. An obvious weakness of the theoretical modeling is that the DBs were created at random points in the amorphous network and were subject only to local relaxation. More complex, but slow (> 10 ns) relaxation mechanisms possibly occurring in the real material are therefore not captured at all. If present, such relaxations might select a subset of the present defect models,

or even other configurations. For instance, the floating-bond type defect exhibits states delocalized over several Si atoms [83, 84]. However, the floating-bond model has long been rejected, being in conflict with a number of other experimental observations [83–86]. In particular, increasing the ^{29}Si content of the samples to 93% was found to give rise to a doublet structure in the spectrum [73], which is incompatible with any model where the electron spin is delocalized over two Si atoms simultaneously. To resolve these contradictory results for the number of Si atoms nearby the electron spin will require additional experiments modulating the isotopic concentration of ^{29}Si. However, at present we can only speculate over plausible microscopic defect models since the available data does not allow us to discriminate them.

4.5 Summary

Using a multifrequency approach, we have determined the principal values of the g-tensor of coordination defects in a-Si:H: $g_x = 2.0080$, $g_y = 2.0060$ and $g_z = 2.0033$ with improved accuracy (cf. Table 4.1). In contrast to earlier studies [19,71], we found that the g-tensor shows pronounced rhombicity. In addition, we carried out a first systematic study where experimental g-, A_L-values and unresolved A-values are compared to theoretical values obtained by DFT calculations of 27 different a-Si:H DB models. As main conclusions we found that the computer models of DB defects reproduce the experimentally observed principal values and the rhombicity of the g-tensor, but do not exhibit HFIs in agreement with the experiment. The apparent discrepancy between the symmetry properties of the g-tensor and the HFIs is attributed to the fact that the g-tensor reflects the global and not the local electronic structure. Indeed, we showed that DBs with a localized and a delocalized electronic structure can give rise to almost identical g-tensors. The principal values of the A_L-tensor for the computer generated DB models disagree with the values obtained by the multifrequency fit. The isotropic HFI of the DB models is on average A_{iso} = - 252 MHz which is much larger than the fit result, A_{iso} = 186 MHz. Our DFT calculations do not support the hypothesis formulated in earlier studies that the structure of DB defects relaxes towards a more planar geometry and thereby reduces the isotropic HFI. In addition to the discrepancies of the A_L-tensor, we observe severe deviations of the second-largest HFI between theory and experiment. We showed that the average

	principal values of g-tensor			principal values of ^{29}Si A_L-tensor				broadening function	
	g_x or $g_\perp$ (g_x - strain)**	g_y or $g_\perp$ (g_y - strain)**	g_z or $g_{\|\|}$ (g_z - strain)**	A_x or $A_\perp$ (A_x- strain)	A_y or $A_\perp$ (A_y- strain)	A_z or $A_{\|\|}$ (A_z- strain)	A_{iso}/A_{dip}	Voigtian function (Gauss/ Lorentz) ΔB_{pp}	χ^2
				[MHz]*	[MHz]*	[MHz]*	[MHz]*	[mT]	
fit with rhombic $\boldsymbol{g}$/ axial $\boldsymbol{A}_L$	2.0080 (0.0052)	2.0060 (0.0021)	2.0033 (0.0017)	151 (63)	151 (63)	257 (90)	186/35	0.11/0.25	0.09
fit with axial $\boldsymbol{g}$/ axial $\boldsymbol{A}_L$	2.0065 (0.0047)	2.0065 (0.0047)	2.0042 (0.0019)	146 (98)	146 (98)	244 (75)	178/33	0.11/0.25	0.24
Umeda et al. [71]	2.0065 (N/A***)	2.0065 (N/A ***)	2.0039 (N/A ***)	143 (56)	143 (56)	333 (73)	206/63	(N/A***)	
Stutzmann et al. [19]	2.0080 (0.0029)	2.0080 (0.0029)	2.0040 (0.0022)	154 (28)	154 (28)	305 (56)	205/50	Not specified	
Present theory (DFT)	2.0094 (0.0084)	2.0064 (0.0059)	2.0035 (0.0035)	-213 (162)	-215 (163)	-326 (200)	-252/-37	cf. text	

Table 4.1: Summary of experimental (multifrequency fit) and theoretical g-tensor and A_L-tensor principal values for coordination defects in a-Si:H. Full-width half maximum (FWHM) of gaussian distributions of the g- and A_L-tensor principal values (g- and A-strain) are given in brackets.
(*) - values given in mT converted to MHz using $\nu = g_e \mu_B B/h$, with g_e the free electron g-value
(**) - ΔB value given in mT converted to Δg (dimensionless) using $\Delta g = (g_e^2 \mu_B/h) \cdot (\Delta B/\nu)$
(***) - In the fitting model of Ref. [71] g-strain and magnetic-field independent broadening are entangled and could not be separated.

number of Si atoms per coordination defect with a HFI larger than 100 MHz is $N \approx 2$. These observations strongly suggest that coordination defects in a-Si:H are much more delocalized than the investigated DB models. We therefore conclude that coordination defects in a-Si:H are not well-described within the random DB model. However, a definite conclusion requires to develop plausible alternative models, additional DFT studies and comparative multifrequency EPR studies on a-Si:H materials with modulated Si and H isotope compositions. Such studies are on the way within the research network EPR-Solar.

5 Structural differences between light-induced and native defects in a-Si:H

It is a common believe that the electronic structure and atomistic origin of native coordination defects generated during the deposition process of a-Si:H and light-induced defects generated by light soaking are identical. In fact, most of the theoretical models explaining the microscopic details of the SWE are based on the explicit assumption that native and light-induced defects are DB defects. An experimental investigation of this hypothesis by EPR can therefore provide a serious test of the available models explaining the SWE.

In this chapter we provide a detailed high-field (Q-Band) pulse EPR measurement of light-induced defects in light-soaked a-Si:H. Primary-echo decay measurements in dependence of the magnetic field position show a strong anisotropic transversal relaxation. The origin of this effect is traced back to a difference in the EPR spectra and transversal relaxation properties of native and light-induced defects. The difference in the primary-echo decay of both defect species is applied to disentangle the highly overlapping EPR spectra. In addition, ENDOR measurements are presented to determine the H distribution around native and light-induced defects since a correlation of defects and H atoms is believed to be an important detail for the generation of defect states in the SWE. Before the experimental details and results are presented, a detailed overview of the history of the SWE, the most important experimental facts and theoretical models explaining the microscopic details of the SWE is presented.

5.1 The Staebler-Wronski effect

In 1977, Staebler and Wronski observed that illumination of undoped a-Si:H with intense light decreases both the dark- and photoconductivity (Staebler-Wronski effect - SWE) [8, 9]. They found that annealing of the samples to temperatures of about 150°C completely reverses the effect. Subsequent investigations discovered that the observed conductivity decrease is due to a shift of the Fermi level towards midgap and a severe decrease of the excess charge carrier lifetime, while the mobility is essentially unchanged. It was not until 1980 that Dersch et al. [14] investigated a-Si:H by c.w. EPR methods realizing that the observed degradation is caused by an increase of the EPR absorption signal at $g = 2.0055$, i.e. the defect density increases. They also found that the additional light-induced defects are metastable and can be removed by annealing to about 150°C. Today it is clear that the light-induced increase of the defect concentration is the most important, but not the only degradation mechanism of a-Si:H [13]. Defect centers contribute most to the decrease of the excess charge carrier lifetime, since the carrier lifetime is strongly correlated to the defect-density N_s [15].

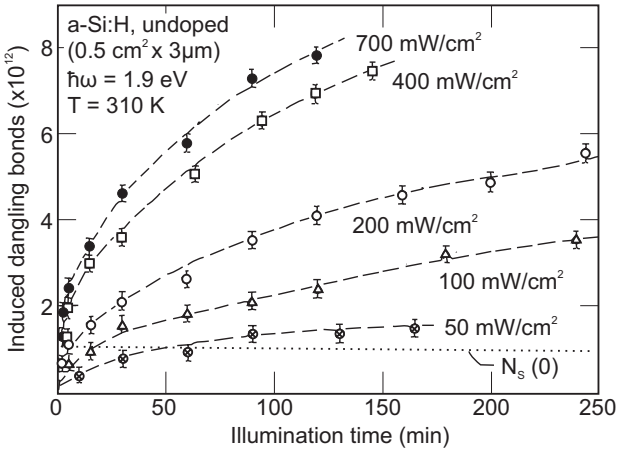

Figure 5.1: Number of light-induced defects vs. illumination time measured by EPR at various light intensities. Please note that the ordinate displays the total number of defects *minus* the number of defects in the initial state. Sample and illumination details are displayed in the upper left corner. The horizontal dotted line indicates the number of DBs $N_s(0)$ prior to illumination. Figure reproduced from Ref. [15].

It was found experimentally that the number of metastable defects increases as $N_s \propto t^{1/3} I^{0.6}$ under continuous light illumination for a time t and light intensity I (cf. Fig. 5.1). The increase of the defect density does not depend on the impurity concentration in the material if the amount of impurities is kept at a low or moderate level [15]. The fact that the SWE also appears in highly-purified (UHV) a-Si:H samples suggests that the microscopic defect reactions are intrinsic to a-Si:H, that is, they only involve a redistribution of Si and H atoms [87]. In order to explain the SWE, several authors proposed intrinsic microscopic models. In this section the main theories available in the literature are briefly explained and the possibilities how these theories can be tested by EPR methods are discussed.

EPR facts of light-induced paramagnetic defects Before we discuss the SWE models in detail, a short review of the most important facts about light-induced defects obtained by EPR is given. These are important details about the microscopic structure of light-induced defects which lead to a consistent disprove of some theories and also stimulated a variety of new model explanations of the SWE.

Investigation of light-induced and native defects by c.w. EPR showed that there is no significant difference between the X-Band EPR spectrum of the two defect species [88]. The g-value and the line shape are unchanged and it was concluded that the microscopic origin of both native and light-induced defects are DBs [14, 88] . There is clear evidence that the defects are isolated from each other on the length scale of the Si-Si bond length (2-3 Å) since the quantum number of the electron spin system is $S = 1/2$ and no exchange narrowing is observed [14, 89] . If the spins were arranged in pairs with a distance of 2-3 Å, a spin singlet or triplet would arise and S would deviate from $S = 1/2$. It is known that high defect concentrations, as observed e.g. in unhydrogenated a-Si, narrow the EPR resonance line due to exchange interaction. Since the shape of the EPR line in the light-soaked state is identical to the EPR line of native defects at X-Band, strong clustering of defects on a small length scale can be excluded. This observation triggered a variety of SWE models which proposed that initially two strongly correlated defects are generated by breaking of a weak Si-Si bond which are then separated on a fast time scale. The corresponding models are discussed in detail below.

Another important fact of light-induced defects in a-Si:H is that the defects do not show an obvious splitting of the EPR resonance due to a large HFI to H atoms [73, 90].

That means that there is no direct evidence for light-induced defects involving H atoms (e.g. three-center bond Si-H-Si) or defects being spatially correlated to H atoms at very short distances (1-2 Å). In fact, two experimental studies of light-induced defects by EDMR [77] and ESEEM [22] measured only contributions from distant H atoms with a distance $r > 4$ Å between the defect center and the H atom. They conclude that there is no significant amount of H in the vicinity of the defect. Isoya et al. [22] even explicitly state that there are no H atoms closer than 4 Å to the defect center (depletion zone). This observation triggered a variety of SWE models which predict metastable states, where the paramagnetic defect is not spatially correlated to H atoms (e.g. the H collision model).

Excess charge-carrier recombination and weak Si-Si bond breaking In a series of experiments, Staebler and Wronski showed that a metastable increase of the defect concentration can also be generated by injecting excess charge carriers in a-Si:H pin diodes and can be prevented when light-illumination is combined with a strong reverse bias to remove light-generated charge carriers from the i-layer. It is therefore clear that the degradation is induced by excess charge carrier trapping or recombination and not by the initial light absorption event itself [20]. From these experiments Stutzmann et al. [15] concluded that bimolecular recombination of excess charge carriers is the cause of defect creation and derived a differential equation for the defect concentration N_s

$$\frac{dN_s}{dt} = c_{sw} np \tag{5.1}$$

where n, p are the electron and hole concentrations, respectively and c_{sw} denotes an empirical proportionality factor depending on microscopic details of the defect creation mechanism. If there is already a certain amount of defects available Eq. 5.1 can be easily solved by assuming that most of the recombination is taking place at defect sites. In this monomolecular recombination limit the charge carrier densities n and p are proportional to G/N_s, where G is the photocarrier generation rate. Together with Eq. 5.1 we then obtain the experimentally observed defect creation dynamics $N_s \propto t^{1/3} G^{2/3}$. This result also reproduces the intensity dependence ($N_s \propto I^{0.6}$), if we assume that G is proportional to the light intensity I.

For the microscopic process leading to the creation of defects, Stutzmann et al. [15] explicitly assumed that the generated defects are DB defects. They proposed the following process leading to the generation of light-induced DB defects (for an example of the spin-density distribution of a DB, cf. Fig. 4.2 a). Excess electrons and holes are trapped or recombine non-radiatively (bimolecular recombination) at a weak Si-Si bond site of the valence band tail. The energy of the recombination is released into the lattice and leads to breaking of the weak Si-Si bond. In their model, the weak bond enters an excited state after trapping an electron-hole pair, which leads to the formation of two adjacent DB defects (cf. Fig. 5.2 a). Since such a configuration is unlikely to be stable with an annealing energy barrier of 1.1 eV, the DBs must be separated on a short timescale after their creation.

One possibility for a separation of the generated DBs is motion of H atoms. The following defect reactions, illustrated in Fig. 5.2b), describe how this can occur:

1. Si-H + Si-Si →Si-DB* + (Si-H/DB*-Si), Ref. [15, 91]
2. Si-H/Si-H + Si-Si →2(Si-H/DB*-Si), Ref. [92, 93]
3. Si-H/H-Si + Si-Si →2{Si-H/DB*-Si} Ref. [94].

Here Si-H denote isolated Si-H bonds and Si-DB* indicate isolated metastable light-induced DBs. Native and light-induced DBs are distinguished by adding (*) for the light-induced DBs. Weak Si-Si bonds are denoted by Si-Si. By short-range diffusion of one or two H atoms, the Si-Si bonds are transformed into a three center bond (Si-H/DB*-Si) or a local dihydride cluster (Si-H/H-Si) or a dissociation of H_2^*-complexes (Si-H/Si-H) as in case of (2). Please note that (Si-H/DB*-Si) and {Si-H/DB*-Si} denote two different spatially correlated DB-H pairs:

- For (Si-H/DB*-Si) the H atom is located on a bond centered site and the distance between the DB and the H atom is about 1-2 Å. This is the original model proposed in Ref. [15].
- For {Si-H/DB*-Si} the distance between the DB and the H atom is about 4-5 Å since the H atom is located in a tetrahedral like site (T_d) [94].

Defect reaction (1) after H bond switching (cf. Fig. 5.2b-1) yields two DBs which are located within one lattice constant to the H atom [15]. In this case one expects a

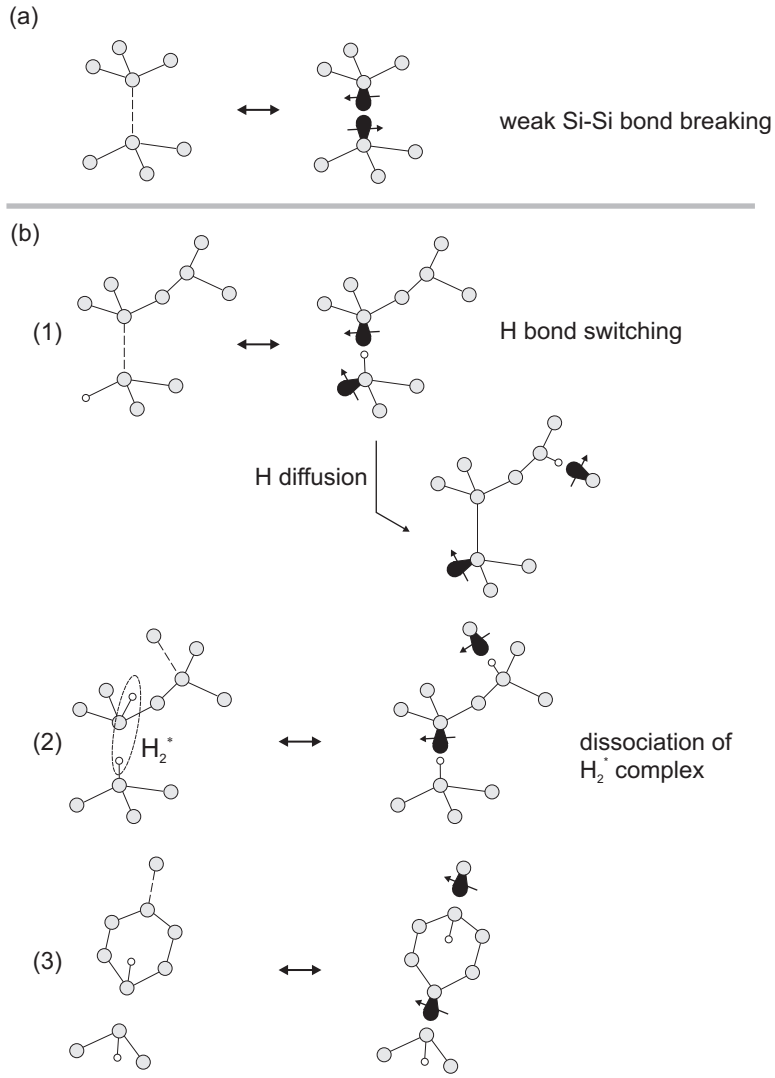

Figure 5.2: Microscopic defect reactions proposed for the creation of metastable DBs in the SWE. Gray objects denote Si atoms, open objects denote H atoms, dashed lines indicate weak Si-Si bonds, DBs are indicated by a schematic wave function and the spins of the unpaired electrons are indicated by arrows. (a) breaking of weak Si-Si bond by an excess charge carrier recombination event; (b) weak Si-Si bond breaking involving motion of H atoms: (1) stabilization of broken bond by H bond switching - by H diffusion the DBs can be separated even further, (2) dissociation of H_2^*-complex yields two DBs spatially correlated to H atoms, and (3) H atoms located in a tetrahedral site switch to neighboring Si atoms. Distance between DBs and H atoms is larger than in model (2).

significant spin-spin coupling between the two paramagnetic defects which is in conflict with experimental facts known from EPR, discussed above. Morigaki [91] showed that the DB defects are further separated by H diffusion which consequently reduces the spin-spin coupling as the distance increases.

The H diffusion is also included in the model of a dissociation of a H_2^*-complex (defect reaction 2) and yields two separated metastable DBs as shown in Fig. 5.2b-2 [92, 93]. In contrast to defect reaction (1) this model predicts that all metastable defects are spatially correlated to H atoms and not only half of them. The difference between the two defect reactions has serious consequences for the interpretation of EPR measurements in a-Si:H. As will be outlined in sec. 5.3, the spatially correlated defects might not be observable in the EPR spectrum due to a large HFI with the H atoms in their vicinity. If this is true, the real metastable defect density is twice as large as determined by conventional c.w. EPR measurements.

Defect reaction (3) is an example of a state where DB defects are spatially correlated to H atoms but do not exhibit a large HFI between [94]. The H atoms are located in a tetrahedral like site and not on a bond centered site as for defect reaction (1). This increases the distance between the DB defects and the H atoms and therefore decreases the HFI.

We have already seen that EPR experiments do not show any evidence for DBs spatially correlated to H atoms, at least if the distance is large enough and the HFI small. This experimental observation stimulated a variety of alternative microscopic models for the SWE.

Si-H bond dissociation and Hydrogen collision model A simple model of the SWE would be the direct emission of H atoms from Si-H bonds, leading to the formation of DBs. However, in order to avoid recombination with the created defect the H atoms have to diffuse away from the broken bond and the process quickly becomes irreversible [95]. This model was excluded as a source of the SWE.

Branz extended the Si-H bond dissociation model by proposing a collision step between mobile H atoms, originally emitted from Si-H bonds [96]. The two mobile H atoms form a metastable H-complex denoted by M(Si-H)$_2$ in a strongly exothermic reaction as shown in Fig.5.3. The defect reaction of this process is given by 2(Si-H) + Si-Si $\rightarrow$2(Si-DB*) + M(Si-H)$_2$. By annealing at 150 °C for several hours, the process is reversed and the

metastable complexes dissociate and saturate the DBs. The predicted time evolution of the DB concentration is again $N_s \propto t^{1/3}G^{2/3}$, as in the case of the weak Si-Si bond breaking model, but derived from different physical processes.

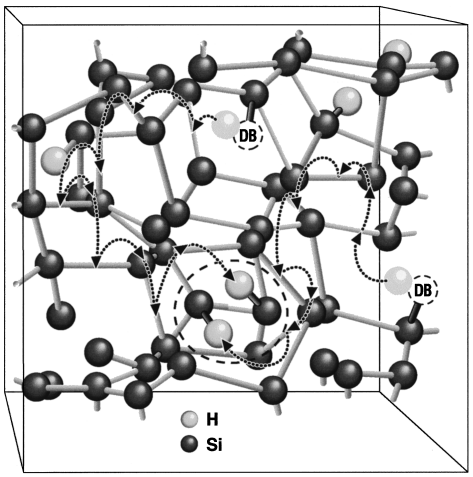

Figure 5.3: Schematic representation of the microscopic processes within the framework of the H collision model. Figure reproduced from Ref. [96].

Transformation of existing non-paramagnetic charged dangling-bond defects Another model accounting for the light-induced increase of paramagnetic DBs was introduced by Adler and proposes a charge transfer between originally charged DBs (DB^+, DB^-) with an effective negative correlation energy [97] (cf. Fig.5.4). This process does not create new DBs, but transforms non-paramagnetic centers into paramagnetic DBs, which are then observable by EPR. However, charged DB densities appear to be too low in undoped a-Si:H to support this model and the experimentally determined time evolution of the DB density is not compatible with the one-carrier capture mechanism (cf. Ref. [96] and references therein).

How to test the theoretical descriptions of the Staebler-Wronski effect? In the preceding discussion we have seen that different models, based on completely different microscopic processes, do actually result in the same unusual sublinear time-dependence. It is therefore most difficult to distinguish between the available theories by merely considering the time evolution of the DB concentration. Another approach to deduce the

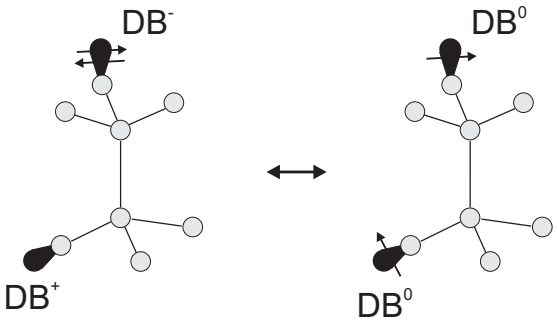

Figure 5.4: Schematic representation of the charge-transfer model proposed by Adler [97]. Grey objects denote Si atoms and DBs are indicated by a schematic wave function and an arrow indicating the electron spin.

microscopic origin and dynamics of the SWE is a microscopic investigation of the final metastable state by EPR methods. Here different models do actually predict quite different microscopic centers for the metastable state and its environment offering a possibility to test the available theoretical models:

- The presented SWE models altogether describe defect reactions which explicitly generate DB defects. In addition, the H collision model [96] and the defect recharging model by Adler [97] explicitly state that the metastable defects are isolated DBs and are therefore by definition identical to native defects. The theoretical prediction that the light-induced defects are identical to native defects can be tested experimentally by a comparison of the EPR spectrum of native and light-induced defects. This relation will be investigated in detail in the following section.

- The weak Si-Si bond breaking model demands a separation of the light-induced DB defects by a redistribution and/or diffusion of H atoms. If the H atoms are redistributed locally, that is, the H motion is restricted to a small length scale, the DB defects are not well separated. Although the distance between the defects should be large enough for exchange narrowing to be absent, a small residual dipolar coupling between the electron spins could prevail. In order to determine the dipolar coupling between the electron spins and their spatial distribution an investigation of the primary-echo decay of light-induced defects is mandatory, since small dipolar couplings between the electron spin influence the transversal spin relaxation properties (cf. section 2.6.2).

- The weak Si-Si bond breaking model predicts the presence of spatially correlated light-induced DB-H pairs in the light-soaked state B. In the annealed state A, the DBs are not correlated to H atoms. Due to their magnetic moment, close H atoms with a large HFI induce a characteristic splitting of the EPR spectrum. The predicted splitting is obviously not present in the EPR spectra. However, if the HFI of the H atom of a spatially correlated light-induced DB-H pair is smaller than 30 MHz and widely distributed, the EPR spectrum will not be affected due to strong inhomogeneous broadening by unresolved HFI and g-strain. The application of advanced EPR techniques like ESEEM or ENDOR is necessary in this case. A comparison of ESEEM and ENDOR spectra of light-induced and native defects can provide conclusive evidence whether or not correlated DB-H pairs are present.

5.2 Pulse EPR investigation of light-induced defects

In order to perform the discussed experimental test of the SWE models and to determine the EPR parameters (g-tensor and HFIs) of light-induced defects, pulsed EPR measurements are carried out. Multifrequency EPR investigation of native coordination defects presented in chapter 4 showed that this approach is capable of providing a precise measurement of the g-tensor principal values and large HFIs. The techniques developed in chapter 4 are now applied to investigate light-induced defects.

In order to investigate light-induced defects, a-Si:H samples are degraded by light soaking. After EPR measurements in the light-soaked state, the samples are thermally annealed and investigated again by EPR. In this section results from device-grade (sample B) and non-device grade (sample C) a-Si:H samples are presented. The following EPR investigation shows that the EPR parameters of native and light-induced defects in both sample types do not significantly deviate and the observed effects can be considered as universal for the sample set presented in this thesis. Since it is difficult to investigate device-grade sample B in the annealed state due to the low defect density, comparisons between the annealed and light-soaked state are carried out for the non-device grade sample C which exhibits a higher initial defect density. A more detailed pulse EPR investigation in the light-soaked state is carried out on the device-grade sample B.

Fig. 5.5 shows the comparison of light-soaked and annealed FSE spectra of sample C. It is important to realize that Fig. 5.5 shows the normalized EPR spectra. The absolute EPR intensity as well as the total defect density N_S is of course larger in the light-soaked state. The FSE spectrum in the light-soaked state obviously deviates from the FSE spectrum in the annealed state. Please note that the difference is rather small and is only resolved here due to the fact that the experiment was carried out at high-field (Q-Band). At lower microwave frequencies the difference is negligible and was therefore overseen in the past since most EPR experiments published in the literature were carried out at X-Band.

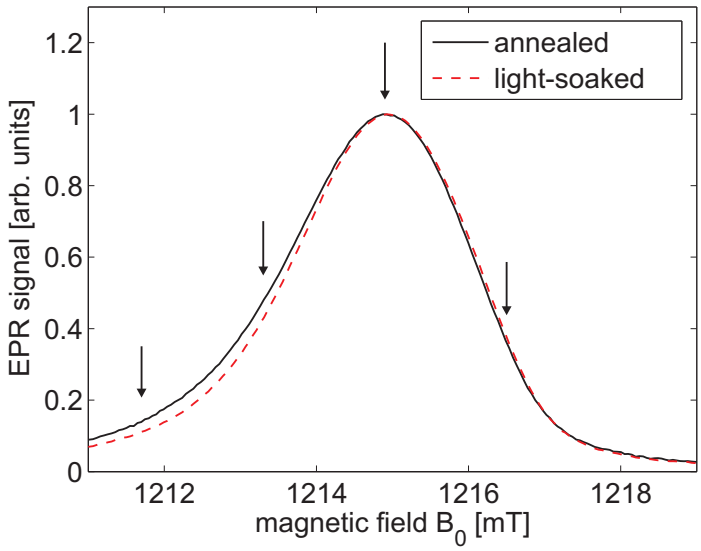

Figure 5.5: Normalized FSE spectra of sample C in the annealed and light-soaked state measured with a pulse delay $\tau = 300$ ns and at a temperature of 80 K. Arrows indicate magnetic-field positions where primary-echo decays were recorded (cf. Fig. 5.14). EPR spectra are normalized to a microwave frequency of 34.10 GHz.

There are several possibilities for the origin of the observed deviation:

1. The EPR spectrum and the interaction parameters of the two defect species are different (different g-tensor or HFIs)

2. The presented measurements are pulse EPR experiments, hence different transversal relaxation properties can lead to a difference in the observed FSE spectra

In order to find out if (1), (2) or maybe both mechanisms are the origin for the observed deviation of the FSE spectra, the FSE spectrum and the corresponding primary-echo decay are investigated in more detail.

As noted earlier, the more detailed pulse EPR investigation is carried out on sample B and the results are shown in Fig. 5.6. The transversal spin relaxation is evaluated using a conventional primary-echo pulse sequence (for details about the pulse sequence cf. sec. 3.2.1). The primary-echo decay is recorded at a temperature of T = 60 K and for different magnetic field positions. To ensure that only the on-resonance spin packets selected by the magnetic field contribute to the echo decay, the echo is fully integrated.

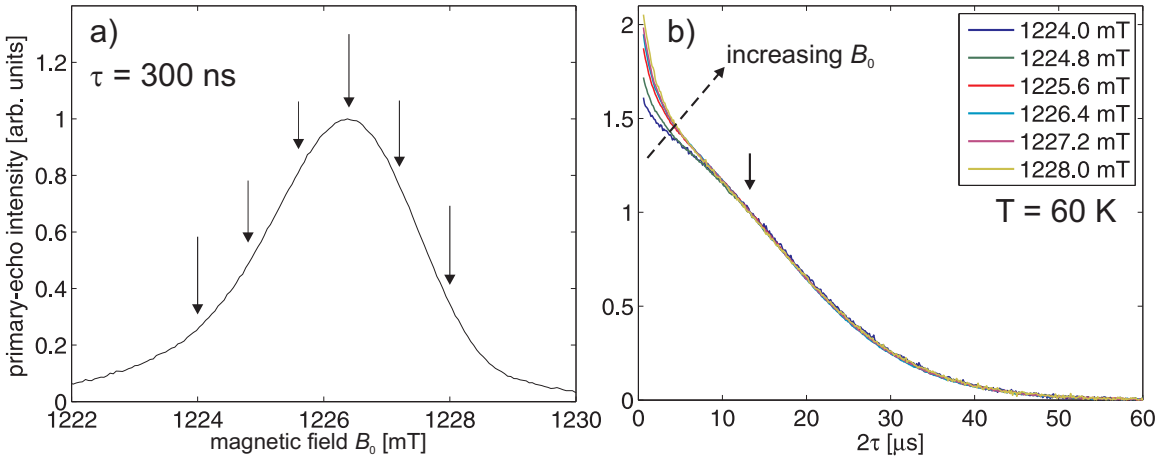

Figure 5.6: Pulse EPR investigation of of sample B in the light-soaked state. a) FSE spectrum measured with a pulse delay τ = 300 ns at a temperature of 60 K. b) Corresponding primary-echo decay at magnetic field values indicated by arrows in a). The echo decays are normalized to the echo amplitude at the pulse delay value indicated by the solid arrow in b).

From 5.6b), we see that the primary-echo decay shows a strong dependence on the magnetic field position. Please note that this was not the case for native coordination defects (cf. chapter 4). Since an anisotropic transversal spin relaxation can seriously distort the EPR spectrum, a straight-forward determination of the g-tensor and the HFIs as in the case for native coordination defects is no longer possible and great care has to be taken to extract the correct values.

On the high-field side of the spectrum the primary echo decays much faster for small pulse delays τ than on the low-field side. To clarify the origin of this unusual behavior, the primary-echo decay is studied as a function of temperature.

The resulting primary-echo decays of sample B (light-soaked) measured at the peak of the resonance are shown in Fig. 5.7a) and b) for temperatures ranging from 293 K to 40 K. At room temperature the echo decay is mono-exponential with a decay time constant of $T_m = 4.3\,\mu s$. The mono-exponential nature of the echo-decay and the fact that the spin-lattice relaxation time $T_1 = 6\,\mu s$ [98] is approximately equal to T_m indicates that the primary-echo decay is limited by spin-lattice relaxation. Upon decreasing temperature the primary-echo decay becomes slower, due to an increase of T_1 [98]. However, already at temperatures lower than 200 K the echo decay is no longer mono-exponential and develops a complicated functional behavior. The echo decays taken at 60 K and 40 K differ only slightly, which suggests that the decay saturates at low temperatures. At the lowest temperature, T = 40 K, the decay is composed of two components, a fast decay at short τ - delays and a rather slow decay with a $\exp[-\tau^2]$ dependence at long τ - delays (cf. Fig. 5.8).

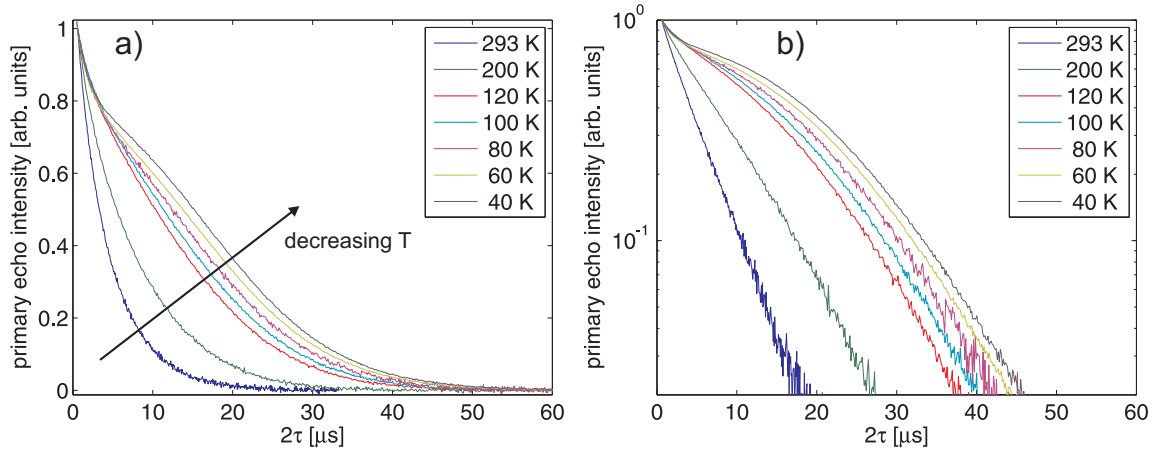

Figure 5.7: Temperature dependence of the primary-echo decay in sample B (light-soaked) recorded in the center of the absorption line (g = 2.0055). The echo is fully integrated and the decays are normalized. a) Linear plot, b) Semi-logarithmic plot.

The slow decay is attributed to spectral diffusion initiated by flip-flop processes of nuclear spins of H atoms [99]. The functional dependence of the primary-echo decay by this process is given by (cf. sec. 2.6.2)

$$I_e = I_0 \, exp\left[-(\tau/T_{SD})^2\right] \tag{5.2}$$

where T_{SD} is the temperature independent spectral diffusion time constant [99]. This mechanism dominates the transversal spin relaxation at low temperatures, where the spin-lattice relaxation has become sufficiently slow (around $T = 40$ K). The spectral diffusion time constant T_{SD} can be extracted by fitting Eq. 5.2 to the echo decay in the long τ range ($5\,\mu s - 33\,\mu s$). The fit result is shown in Fig. 5.8b) and yields $T_{SD} = 11.4\,\mu s$.

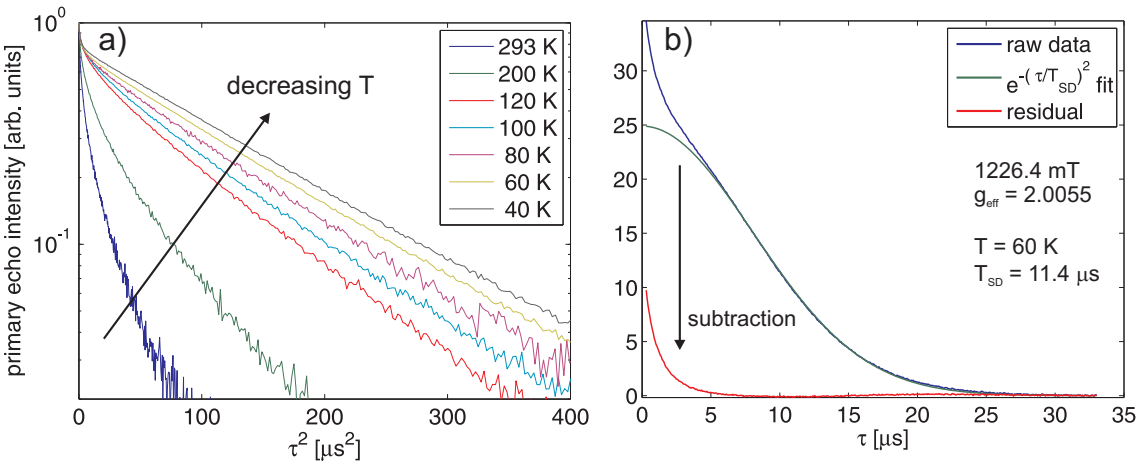

Figure 5.8: Temperature dependence of the primary-echo decay in sample B (light-soaked) recorded in the center of the absorption line ($g = 2.0055$). a) Semi-logarithmic plot versus τ^2. b) Fit (green curve) of Eq. 5.2 to the long τ range ($5\,\mu s - 33\,\mu s$). Subtracting the fit from the primary-echo decay (blue curve) results in the residual red curve.

It is important to note that T_{SD} strongly depends on the concentration and distribution of H atoms in the material and therefore depends on the sample properties and deposition conditions [99]. Various T_{SD} values for samples in this study and values taken from literature are summarized in Tab. 5.1. Sample A and C were prepared under identical conditions and therefore exhibit the same H concentration and nearly identical T_{SD} values. The larger T_{SD} value of device-grade sample B suggests that it exhibits a smaller H concentration.

a-Si:H sample	mw-band	state	N_s [cm^{-3}]	T_{SD} [μs]	H conc. [at. %]
A	Q	as-dep.	$3.2 \cdot 10^{16}$	7.9 ± 0.5	-
B	Q	light soaked	$4.6 \cdot 10^{16}$	11.4 ± 0.5	-
C	Q	light soaked	$5.3 \cdot 10^{16}$	7.6 ± 0.5	-
a-Si:H (Ref. [99])	X	as-dep.	$8 \cdot 10^{17}$	6.6 ± 0.5	33 (NMR)

Table 5.1: Spectral diffusion characteristic time T_{SD} of defects in a-Si:H for various samples and comparison with values reported in the literature. Typical errors for the defect density are 30 % [56].

Besides the analyzed nuclear-spin induced spectral diffusion component, the primary-echo decay exhibits an additional fast decay, which can be analyzed by subtracting the slowly decaying spectral diffusion function from the echo decay (cf. Fig. 5.8b). The residual of the primary-echo after subtraction corresponds to the fast relaxing echo decay which is now isolated and can be analyzed separately from the slow primary-echo decay discussed above. In Fig. 5.9 the residual primary-echo decays are plotted versus the magnetic field position. The residual echo decays follow a mono-exponential function with a decay time constant $T_D = 2.1\,\mu s$ which does not depend on the magnetic field position. It is important to realize that by the presented subtraction procedure the primary-echo decay, which shows initially a strong dependence on the magnetic-field position, can be decomposed into two components whose decay functions do not depend on the magnetic-field position.

This analysis shows that the transversal relaxation pattern initially observed in Fig. 5.6b) is not caused by an orientation dependence of the transversal spin relaxation, since in that case the involved time constants T_{SD} and T_D would change as a function of the position in the EPR resonance [100–102]. Instead, the EPR spectrum is a superposition of two paramagnetic defect centers, which exhibit different transversal relaxation mechanisms and time constants.

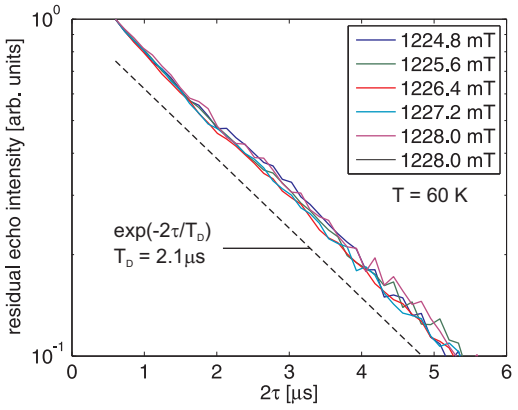

Figure 5.9: Residual primary-echo decay after subtraction of the slow spectral diffusion component at different field values indicated by arrows in Fig. 5.6. Measured at Q-Band and T = 60 K. The dashed line indicates a mono-exponential decay with a time constant T_D= 2.1 μs.

5.2.1 Decomposition of EPR spectrum

We have seen that the EPR spectrum is composed of two spin species, which exhibit different spin relaxation properties. The primary-echo decay time constant of both spin species is isotropic and does not depend on the magnetic-field position. However, the initially observed primary-echo decay (cf. Fig. 5.6 b) does depend on the magnetic field position. The reason for this observation is that the EPR spectra of the two spin species differ from each other. Hence, the two defect centers exhibit different g-tensor principal values, g-strain and/or HFIs. In order to obtain the individual EPR spectra of the two defect centers, the difference in spin relaxation properties can be utilized to decompose the total EPR spectrum. The individual components can then be analyzed separately. The EPR spectra are decomposed by the following procedure which essentially relies on the fact that the relaxation of each spin species is isotropic.

The EPR spectrum of the slowly decaying spin species is directly obtained by fitting Eq. 5.2 to the primary-echo decays. The EPR spectrum, obtained by plotting I_0 versus the magnetic field, is shown by the black open circles in Fig. 5.10 a). This procedure is justified by the fact that the relaxation of the slowly decaying spin species is isotropic.

The EPR spectrum of the fast decaying spin ensemble is obtained by the initial value of the residual echo decay at τ = 300 ns (red open circles in Fig. 5.10 a). It is important to note that due to the rapid spin relaxation the primary echo has already decayed from

its initial value within the spectrometer deadtime. While this effect is negligible for the slowly decaying spin ensemble, the fast relaxing spin ensemble already decayed by about 25 % ($1 - e^{-2\tau/T_D} \approx 0.25$) at $\tau = 300$ ns. However, this is of minor importance for a quantitative discussion of the spectral shape. In case the absolute amplitudes are of interest, one has to correct for this decay.

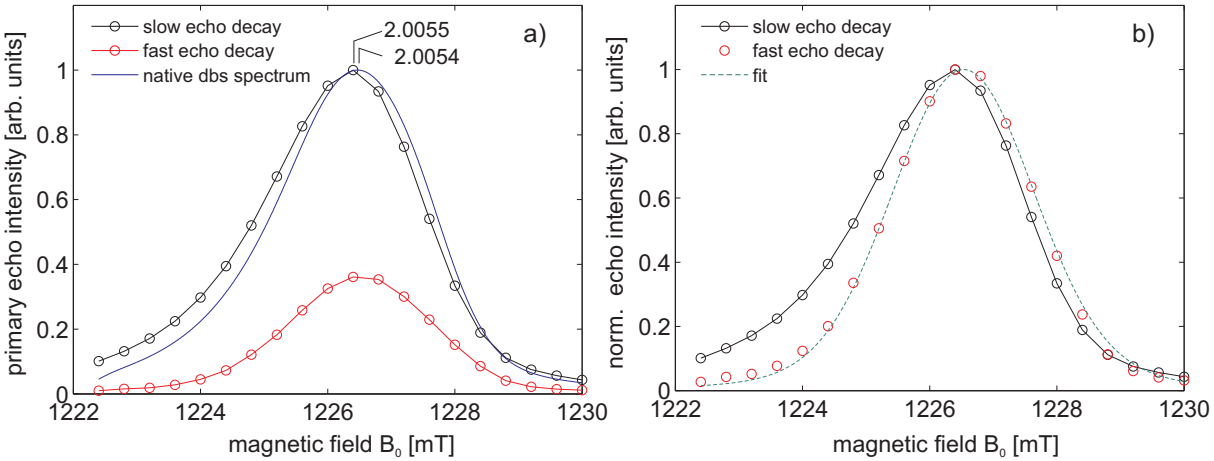

Figure 5.10: Decomposed spectra of the slowly and fast decaying spin subensembles. T = 60 K. a) Amplitude of the slowly decaying spin subensemble (black open circles) following Eq. 5.2 and fast exponentially decaying spin subensemble (red open circles). The blue solid line indicates the EPR spectrum of native defects in as-deposited samples (cf. chapter 4). Spectra are normalized to a microwave frequency of 34.42 GHz. b) Spectra normalized to their maximum amplitude and fit of the EPR spectrum of the fast decaying spin subensemble (green dashed line). For details on the fit model and results see text.

The spectrum of the slowly decaying spin ensemble is shown in Fig. 5.10 a). The shape of the spectrum is slightly asymmetric as observed for native defects in as-deposited a-Si:H (blue line). However, the spectrum is shifted to slightly lower magnetic field values, which indicates that the g-value slightly increases from 2.0054(3) to 2.0055(3). The absolute error of these values is given in brackets and is rather large since the shift corresponds to a magnetic field difference of 60 μT which is difficult to calibrate.

However, relative errors are smaller and the shift is therefore significant. In Fig. 5.10 b) the spectrum of the fast decaying component is compared to the normalized spectrum of the slowly decaying spin ensemble. Its spectral shape is much more symmetric and is close to a Gaussian line shape. The line can be fitted by an isotropic g-tensor with a center-of mass of 2.0053 and a g-value distribution with a FWHM of 0.0040 and a Lorentzian magnetic field broadening with a FWHM of 0.24 mT (dashed line in Fig. 5.10 b).

It is clear that the g-tensor of the light-induced defects also exhibits rhombic symmetry, as observed for native coordination defects in as-deposited a-Si:H (cf. chapter 4). It is, however, difficult to obtain the exact principal values from a measurement of the EPR spectrum at only a single microwave frequency. Nevertheless, the fact that the EPR spectrum is narrower suggests that the g-tensor anisotropy is reduced. One possibility for this is a defect with a more symmetric atomic structure. In the limit of an isotropic wave function the g-tensor anisotropy is zero. It is therefore likely that wave function of light-induced defects is more symmetric than the wave function of native defects.

5.2.2 Defect clusters - instantaneous diffusion

At this point, the question remains why the different spin populations exhibit a different primary-echo decay and EPR spectrum. Especially the origin of the mono-exponential decay of the fast relaxing spin ensemble is unknown. One possibility for the cause of this decay is a clustering of light-induced defects. The dipolar spin-spin interactions between the electron spins of the defect states induce a dephasing of the transversal magnetization by the spectral diffusion mechanism [34, 35]. This can be tested experimentally by decreasing the microwave power of a pulse with constant length to obtain a smaller flip angle. Fig. 5.11 shows that decreasing the flip angle from 180° to about 63°, the primary-echo intensity decreases (decreasing signal-to-noise ratio). However, the decay function qualitatively remains the same. Although the echo decay is unchanged at short and long τ values, the echo signal in the range $5\,\mu s < 2\tau < 10\,\mu s$ is slightly reduced. However, the echo decay is not majorly influenced by decreasing the flip angle and we can conclude that instantaneous diffusion plays only a very minor role for the decay of the primary echo.

The absence of instantaneous diffusion does, however, not mean that the light-induced defects with a fast primary-echo decay do not interact with each other by spin-spin interaction. The instantaneous diffusion effect is rather weak in comparison with the relaxation mechanisms which dominate the primary-echo decay of defects in a-Si:H. It was shown that instantaneous diffusion can be active over a wide range of average defect concentrations. Instantaneous diffusion can be observed at very low concentrations $C = 10^{16}$ cm^{-3} [103] up to very high concentrations $C = 10^{18}$ cm^{-3} [104,105]. One can therefore measure dipolar interaction energies from about 1 kHz to 50 kHz. At a defect concentration of $C = 10^{18}$ cm^{-3} the time constant of the instantaneous diffusion effect is about 1.2 μs for $g = 2$ [21] if the pulse excites the entire resonance line. The time constant of the fast echo decay (cf. Fig. 5.9) is $T_D = 2.1$ μs. The intrinsic transversal relaxation in the limit of a small flip angle is therefore already so fast that additional instantaneous diffusion will not affect the echo decay. It is therefore possible that the local defect concentration is higher than the average defect concentration measured with c.w. EPR $C = 2 - 4 \cdot 10^{16}$ cm^{-3} and a clustering of the light-induced defects occurs. As we will discuss later, it is indeed very probable that the clustering of defects is the cause for the fast primary-echo decay.

5.2.3 Overall description of temperature dependence of the primary-echo decay

Up to now the echo decay of the fast relaxing spin ensemble was analyzed only at a single temperature ($T = 60$ K). In order to conclude on the origin of the fast transversal relaxation mechanism the temperature dependence of T_D needs to be investigated in more detail. The temperature dependence can reveal which spectral diffusion mechanism is active (cf. sec. 2.6). In addition, the time constant T_D of the exponential echo decay of the fast relaxing spin ensemble was determined in a rather unreliable way by subtracting the slowly decaying contribution. Both, the temperature dependence and the correct value of T_D can be obtained by using a fitting model which correctly describes the whole echo decay including both spin ensembles at the same time. We introduce the following model for the overall primary-echo decay

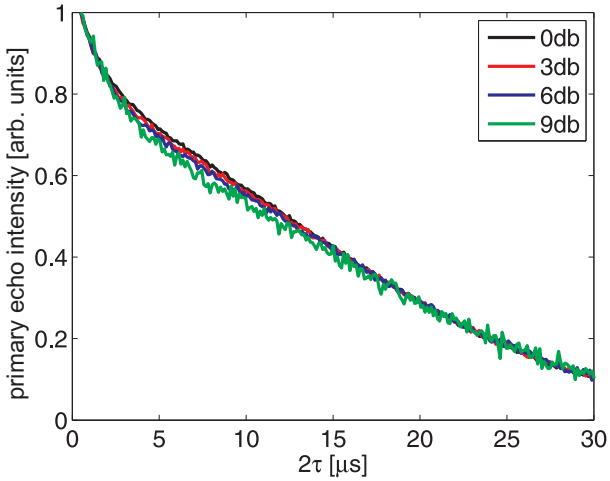

Figure 5.11: Flip angle dependence of primary-echo decay (normalized) in the center of the EPR spectrum ($g = 2.0055$), $T = 80$ K. The length of the first pulse (20 ns) and the length of the second pulse (40 ns) of the primary-echo sequence are kept constant. The microwave power is decreased in steps of 3 db relative to the maximum power available (0 db - 20 mW). The corresponding flip angles of the second pulse are calculated by $\beta = \pi \cdot 10^{-(P-P_{\mathrm{ref}})[\mathrm{db}]/20}$: 0 db - 180°, 3 db - 127°, 6 db - 90°, 9 db - 63°.

$$I_{\mathrm{e}}(\tau, T, \omega) = \mathrm{C}(T) \cdot \exp\left[-\frac{2\tau}{T_{\mathrm{m}}(T)}\right] \times \times \left\{ I_{S_10}(\omega) \cdot \exp\left[-\left(\frac{\tau}{T_{\mathrm{SD}}}\right)^2\right] + I_{S_20}(\omega) \cdot \exp\left[-\frac{2\tau}{T_{\mathrm{D}}}\right] \right\} \quad (5.3)$$

where the two spin subensembles are denoted by S_1 (slowly relaxing spins) and S_2 (fast relaxing spins) and their spectral intensities as a function of the resonance frequency ω are given by $I_{S_1,S_20}(\omega)$. The echo decay of the S_1 spins follows the nuclear-spin induced spectral diffusion decay (Eq. 5.2) with the temperature independent characteristic time T_{SD}. The fast relaxing S_2 spins exhibit a mono-exponential decay with a time constant T_{D}. It is furthermore assumed that the spin populations S_1 and S_2 are subject to the same temperature-dependent T_{m} processes, where T_{m} is an exponential decay time constant. For a detailed discussion of the primary-echo decay and the various relaxation processes please refer to sec. 2.6.2. The temperature dependent parameter C accounts

for Curie's law and the pulse excitation profiles which depend on the pulse length and the cavity Q-factor. Instantaneous diffusion is neglected (cf. sec. 5.2.2). Eq. 5.3 is fitted to the echo decays by non-linear least-squares fitting based on a Levenberg-Marquardt algorithm implemented in MATLAB®. Fit results for the center of the EPR spectrum (g = 2.0055) are shown in Fig. 5.12 a). For the time constants we obtain $T_{SD} = 11.8\,\mu s$ and $T_D = 1.9\,\mu s$. Since all echo decays are well-described by a single T_D value, we conclude that T_D is *temperature-independent*.

The amplitudes $I_{S_1,S_20}(\omega)$ are now handled correctly and the ratio I_{S_10}/I_{S_20} at g = 2.0055 is $\frac{2.5}{1}$ and therefore slightly higher than before. The EPR spectra obtained by the fit (data not shown) are very similar to those obtained by subtracting the slow echo decay (cf. Fig. 5.10). The fit results for the temperature-dependent C parameter are shown in Fig. 5.12 b). It increases with decreasing temperature following a $1/T$ dependence, which is attributed to the increase of the equilibrium magnetization described by Curie's law.

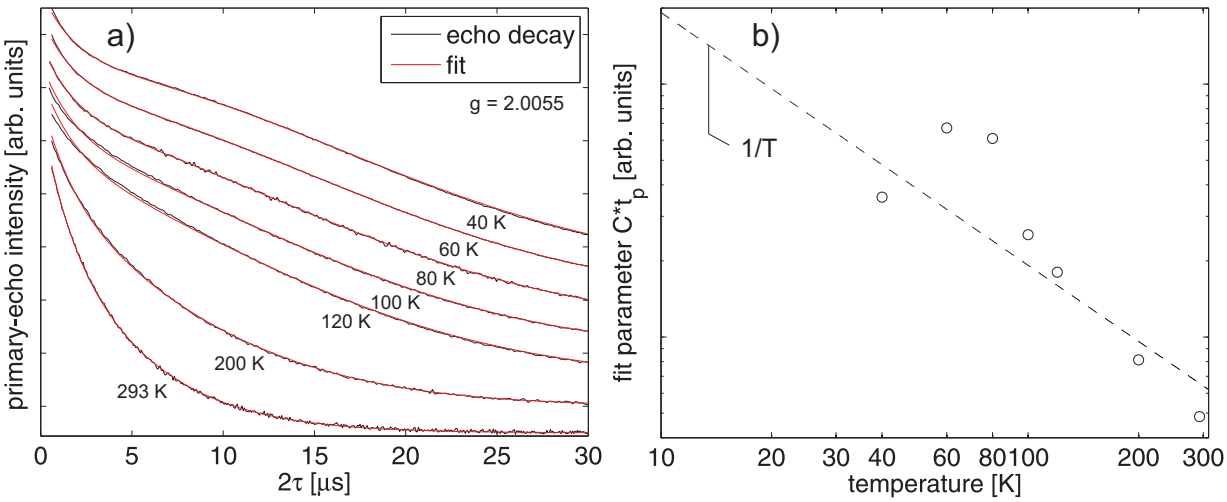

Figure 5.12: a) Temperature dependence of primary-echo decay at g = 2.0055 (black line) fitted by Eq. 5.3(red line). b) Corresponding temperature dependence of fit parameter C scaled with the microwave pulse length to account for the excitation bandwidth.

Fig. 5.13 shows the fit results for T_m in comparison to the spin-lattice relaxation time constant T_1. The latter was determined by inversion recovery (for details about the pulse sequences cf. sec. 3.2.1) and stimulated echo pulse sequences (data not shown). Values

obtained for T_1 in this work agree very well with values obtained in earlier studies [98]. At high temperatures ($T > 80$ K) both T_1 and T_m follow the $T^{-2.3}$ temperature dependence also observed in the case of native defects in a-Si:H [82]. At lower temperatures ($T < 80$ K) deviations from this behavior occur and the spin-lattice relaxation time is larger than predicted by the $T^{-2.3}$ law. If the phase memory time T_m also deviates from this relation is difficult to say because at these low temperatures T_m is too long to be measured by a two-pulse sequence. The fact that T_m shows the same temperature dependence as T_1 indicates that the spin relaxation of both spin populations, S_1 and S_2 , is limited by lifetime broadening induced by spin-lattice relaxation. It is important to realize that this process is a global property of both defect ensembles, while the spectral diffusion process described by T_D only affects S_2 not S_1.

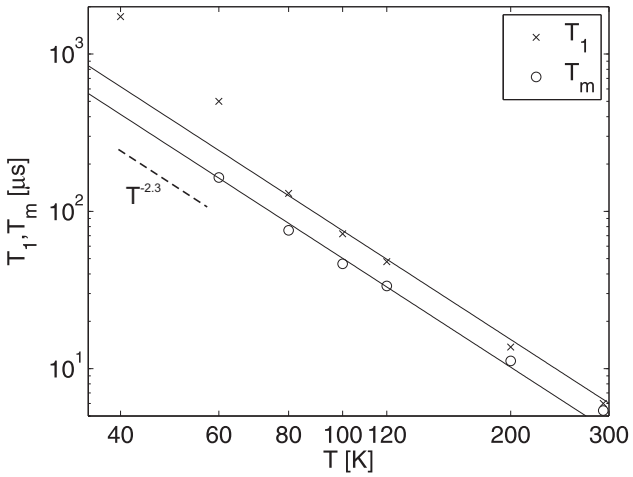

Figure 5.13: Temperature dependence of T_m and T_1 at $g = 2.0055$ determined by the fitting model described by Eq. 5.3.

5.2.4 Reversible changes of the primary-echo decay

In this section it is shown that the observed changes in the primary-echo decay are indeed connected to the SWE. The SWE can be reversed by moderate thermal annealing to restore the original state and defect density of the material. In order to show that the observed changes of the transversal spin relaxation properties are reversible, the primary-echo decay in the light-soaked state has to be compared to the annealed state. However, device-grade samples (sample B) exhibit a very low defect density in the annealed state.

It is therefore difficult to investigate this type of sample due to the low signal intensity. The non-device grade samples investigated in this thesis (sample B) exhibit a larger initial defect density and one can conveniently compare the primary-echo decay in both states.

The FSE spectra of sample C in the light-soaked and annealed state were already presented in Fig. 5.5. Fig. 5.14 b) shows that sample C exhibits an anisotropic primary-echo decay in the light-soaked state very similar to the one observed for sample B. Upon annealing of sample C, the defect density decreases and the primary-echo decay becomes approximately isotropic (Fig. 5.14 a). The changes in the primary-echo decay are therefore reversible.

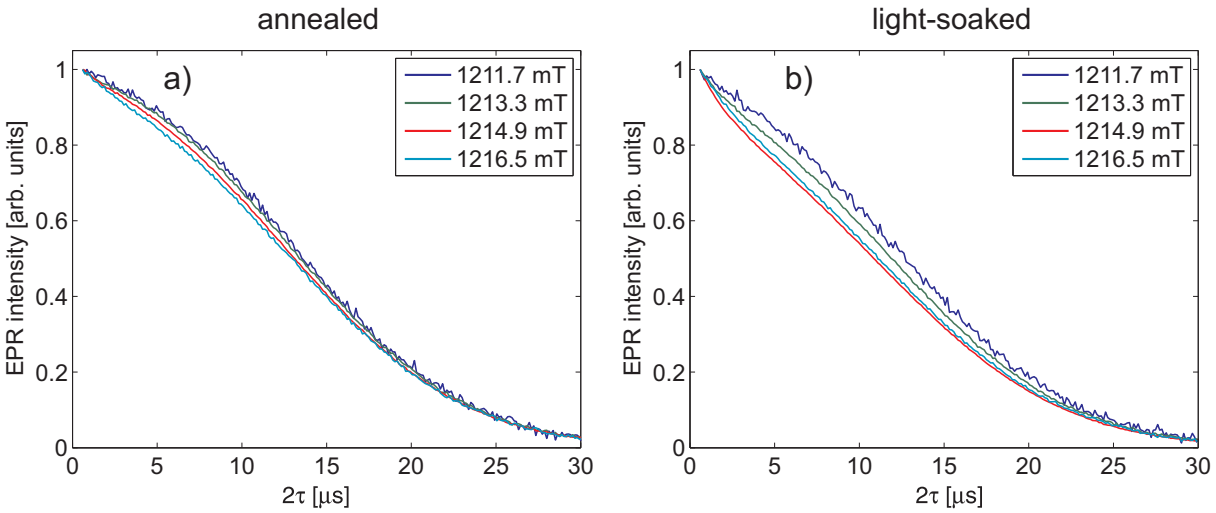

Figure 5.14: Primary-echo decay of sample C at magnetic-field positions indicated by arrows in Fig. 5.5: a) annealed state, b) light-soaked state. The echo decays are normalized to the echo amplitude at τ = 300 ns and to a microwave frequency of 34.10 GHz.

The anisotropy of the primary-echo decay as shown in Fig. 5.14b) is similar to the anisotropy observed for sample B. The decomposition of the spectrum taken in the light-soaked state by the procedure described before is shown in Fig. 5.15. In sample C less defects with a fast spin relaxation are created by light soaking than in sample B. However, the line shape of the spectra is within error the same as the line shape observed for sample B. The amplitude ratio I_{S_10}/I_{S_20} at g = 2.0055 of the two spectral components is $\frac{4.7}{1}$ (cf.

Fig. 5.15) and is approximately equal to the ratio of the defect density in the light-soaked and annealed state as determined by c.w. EPR (ratio is equal to $\frac{4.3}{1}$). It is therefore clear that most of the defects created by light soaking can be attributed to the fast-relaxing spins. It is, however, important to note that the ratio of $\frac{4.7}{1}$ observed for sample C is not a universal value. For sample B we observed a different ratio of $\frac{2.5}{1}$ (cf. Fig. 5.10). It is possible that not only fast-relaxing spins are generated by light soaking, but also the number of slowly relaxing spins is increased. Up to now it is unclear which parameter actually determines the amount of the two different defect species. However, there is no doubt that light degradation of a-Si:H generates defects which are distinctly different in their microscopic structure compared to native defects and that these defects can be removed again by thermal annealing.

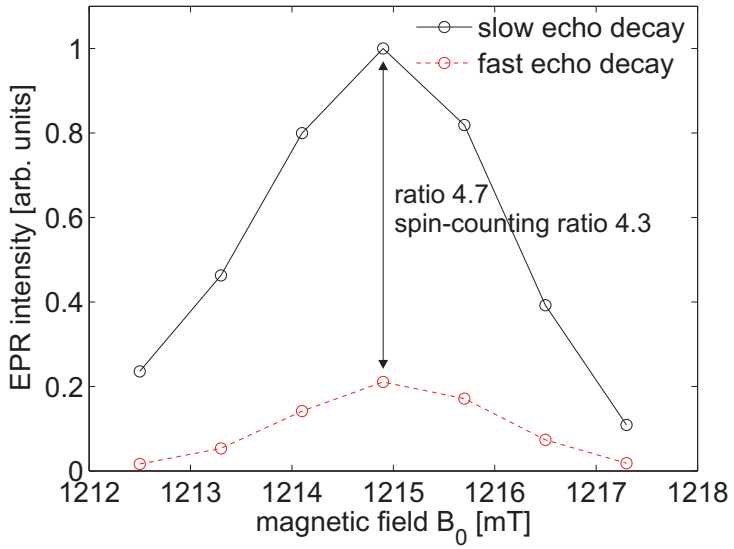

Figure 5.15: Decomposed spectra of sample C of the slowly and fast decaying spin subensembles. T = 80 K. Amplitude of the slowly decaying spin subensemble (black open circles - solid line) following Eq. 5.2 and fast exponentially decaying spin subensembles (red open circles - dashed line).

5.2.5 Discussion

We have shown that the spin relaxation properties of defects in a-Si:H are sensitive to the material state. Transversal spin relaxation properties change rather drastically upon light soaking. It is also known that the longitudinal spin-lattice relaxation time

constant increases upon light soaking [98]. However, in that case T_1 of native and light-induced defects is the same, that is, the spin-lattice relaxation is a global process which is identical for both defect species [98]. This homogeneous increase in T_1 was ascribed to a decrease of the density or coupling to vibrational modes in a-Si:H which are believed to be the cause for the anomalous spin-lattice relaxation [98]. The change of the vibrational mode structure is not surprising in view of macroscopic changes in the mass density of a-Si:H upon light soaking [106]. It is, however, rather difficult to deduce microscopic details about the defect structure from the observed increase of T_1 since quantitative theoretical models of spin-lattice relaxation in these non-crystalline systems are only poorly developed [32].

sample	annealed state	light-soaked state	ratio I_{S_10}/I_{S_20} at $g = 2.0055$ in light-soaked state
A	isotropic echo decay (as-deposited)	not investigated	N/A
B	not investigated	anisotropic echo decay: superposition of slow and fast echo decay	$\frac{2.5}{1}$
C	isotropic echo decay	anisotropic echo decay: superposition of slow and fast echo decay	$\frac{4.7}{1}$

Table 5.2: Primary-echo decay dependence on the magnetic field position for device-grade (sample B) and non-device grade samples (sample A, C) in the as-deposited, annealed and light-soaked state. S_1 (slowly relaxing spins) and S_2 (fast relaxing spins). Data for sample A is not shown.

This is different for the observed changes in the transversal relaxation upon light soaking. We have shown that at low temperatures most of the native and light-induced defects exhibit different primary-echo decays and are therefore subject to different relaxation processes. The two defect species give rise to an anisotropic relaxation of the primary echo which can be observed in device-grade and non-device grade a-Si:H samples

(for overview of samples studied in this thesis cf. Table 5.2). The relaxation processes can be utilized to decompose the EPR spectra into the two underlying components. The two components, defects with a slow and fast primary-echo decay, are analyzed in the following.

Defects with slow primary-echo decay The transversal spin relaxation of defects with a slow primary-echo decay is dominated by nuclear-spin induced spectral diffusion at low temperatures and remains unchanged upon light soaking. The EPR spectrum of these defects peaks at a center-of-mass g-value of 2.0055, is asymmetric and exhibits strong g- and A-strain and is therefore very similar to the EPR spectrum of native coordination defects present in as-deposited a-Si:H (cf. chapter 4). Although there are slight differences in the EPR spectra of both defect species, one can conclude that both belong to the same defect population.

Defects with fast primary-echo decay Defects with a fast primary-echo decay (time constant $T_D = 2.1\,\mu s$) are generated by light soaking and are therefore clearly linked to the SWE. The EPR spectrum of these light-induced defects is distinctly different from the EPR spectrum of native coordination defects. The EPR spectrum peaks at a different center-of-mass g-value of 2.0053 and is more symmetric, which suggests that the g-tensor anisotropy of the defects with a fast primary-echo decay is smaller compared to the g-tensor anisotropy of native coordination defects. It is therefore clear that the microscopic defect structure of these defects is different. More information about the microscopic nature of these defects is contained in their transversal spin relaxation properties. The primary-echo decay of these defects is mono-exponential with a time constant much faster than in case of native defects. The faster time constant could be explained by the creation of these defects in H rich regions of a-Si:H. However, the fact that the primary-echo decay of this process follows a mono-exponential function and not a stretched-exponential suggests that the mechanism is different from nuclear-spin induced spectral diffusion.

Another explanation for the observed primary-echo decay could be a formation of defect clusters. Here, light-induced defects are not isolated from each other and can be close enough to interact with each other by spin-spin dipolar interaction. Such a formation would induce a strong instantaneous diffusion effect of the excited electron

spins (A-spins), which is not observed. However, the decay time constant $T_D = 2.1\,\mu s$ is already so fast that instantaneous diffusion might be negligible, although the defects are arranged in clusters. In that case the spin flip rate of the A-spins could be rather large due to correlated spin flip-flops (spin-spin relaxation) and the instantaneous diffusion effect will be disguised [34]. A further evidence for defect clusters in which the electrons relax via correlated spin flip-flops is the fact that the decay time constant T_D is temperature independent. However, it is important to realize that the average distance r_{av} between the electron spins within a cluster cannot be too small (1nm $< r_{av} <$ 10 nm), otherwise a stronger narrowing of the EPR resonance line due to exchange interaction as in the case of unhydrogenated a-Si should occur [89, 107].

5.3 Investigation of the hydrogen distribution in the vicinity of native and light-induced defects

In sec. 5.1 we have seen that various models explaining the microscopic mechanism of the SWE predict the generation of light-induced DB-H defect pairs by light illumination of a-Si:H. Especially the weak Si-Si bond breaking model predicts the presence of spatially correlated light-induced DB-H pairs in the light-soaked state B. It is generally assumed that DBs are not correlated to H atoms in the annealed state A. The presence of proposed correlated DB-H defect pairs can be resolved by EPR techniques via the HFI between the DB electron spin ($S = 1/2$) and the nuclear spin of the H atom ($I = 1/2$). In principle, the technique allows to measure the magnitude of the HFI with high precision. From the value of the HFI one can determine the distance between the DB defect and the H atom. Since a-Si:H contains a large amount of H (typically 10 at. %), each defect is encircled by several H atoms at different distances. However, if the distances are exactly the same for all defects in the material, the EPR techniques can still unambiguously identify all of them with high precision. The critical problem in the case of defects and H atoms in an amorphous solid, like a-Si:H, is that the environment of the individual defects in the material is not always the same (site-to-site variation). The bond-length, bond-angles and also the distances between the defects and H atoms are widely distributed due to the large disorder present in a-Si:H and a measurement of the H distribution becomes non-trivial.

5.3.1 Hydrogen distribution in the vicinity of native coordination defects

To determine the H distribution experimentally, a variety of EPR investigations were performed in the past. An important result from EPR experiments carried out at X-band is that the replacement of H with deuterium ($I = 1$) during the growth process does not change the EPR absorption line shape of the DB resonance line ($g = 2.0055$) [73]. The hyperfine interaction to nearby nuclei is therefore completely hidden underneath the inhomogeneously broadened EPR resonance and sophisticated techniques like electron spin echo envelope modulation (ESEEM) or electron nuclear double resonance (ENDOR) have to be applied instead of conventional EPR. Isoya and coworkers [22] showed in 1993 by ESEEM experiments that no H atoms are located within a radius of about 3 Å around DBs. In this thesis, the ESEEM experiments of Isoya et al. were reproduced and the result for a two-pulse ESEEM spectrum of native coordination defects in as-deposited a-Si:H is shown in Fig. 5.16. Besides the fact that most of the samples studied in Ref. [22] were deuterated, the ESEEM spectra presented here and those in Ref. [22] are very similar. Resonances are only observed at the free nuclear precession frequencies ν_I (and $2\nu_I$) of ^{29}Si and ^{1}H nuclei and the width of the resonance lines is narrow in all cases, hence the nuclei which dominate the ESEEM spectra are remote matrix nuclei with a very small HFI. The largest HFI which are present in the spectrum are about 5 MHz and the ESEEM spectrum therefore suggests that larger HFIs of both ^{29}Si and ^{1}H nuclei are not present for coordination defects in a-Si:H. However, it is well known that standard two-pulse and three-pulse ESEEM experiments exhibit a number of experimental difficulties.

ESEEM is a time-domain technique, which impedes the observation of broad spectral features in disordered solids [108]. Already from a quick inspection of Fig. 5.16 it becomes clear that the ESEEM spectrum is not free from artifacts. The ν_I contribution for ^{29}Si nuclei is small but the $2\nu_I$ contribution is very intense. A broad distribution of resonance frequencies of ^{29}Si nuclei due to a distribution of HFIs leads to a distribution of the $\nu_{\alpha,\beta}$ contribution. The broad distribution induces a quick decay of the ESEEM oscillations in the time-domain. If the decay time constant (or the width of the $\nu_{\alpha,\beta}$ distribution) is smaller than 100 ns ($\cong$ 10 MHz), the resonances will decay within the dead-time of the spectrometer and will not be observable. The $2\nu_I$ contribution is in first-

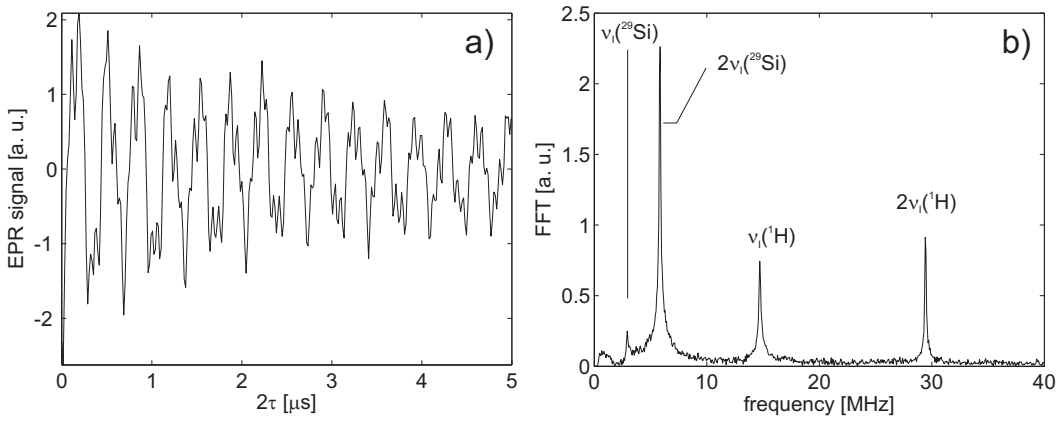

Figure 5.16: Two-pulse ESEEM spectra (X-Band, T = 60 K) of native coordination defects in as-deposited a-Si:H (sample A). a) Modulations of the primary-echo decay after subtraction of a 9th order polynomial. b) Magnitude Fast-Fourier Transformation (FFT) of modulations shown in a). The free nuclear precession frequencies of ^{29}Si and ^{1}H nuclei are indicated.

order approximation not susceptible to such a distribution and therefore remains narrow enough to be observed. With these observations, it is clear that two-pulse (as well as three-pulse) ESEEM is a very unreliable technique to detect HFIs of paramagnetic centers which exhibit a distribution of HFIs. In principle, the full inhomogeneously broadened ESEEM powder pattern can be restored by advanced ESEEM experiments like four-pulse ESEEM and hyperfine sublevel correlation spectroscopy (HYSCORE) [109]. It is, however, difficult to obtain the necessary sensitivity to detect small ensembles of strongly coupled H atoms (cf. Fig. 5.17). In contrast to ESEEM, ENDOR is an ideal tool for detecting strongly coupled nuclei in disordered systems as is illustrated in Fig. 5.17. Davies ENDOR is superior to ESEEM in disordered systems since it is not a time domain technique but a static pulse sequence. As illustrated in sec. 3.2.1 and 2.5, Davies ENDOR is based on an inversion pulse sequence generating an inverted echo. A radiofrequency pulse redistributes populations within the spin system and therefore leads to a reduction of the inversion of the selected spin transition. The spin system is therefore actively manipulated, while ESEEM relies on a free transient evolution of the spin system under the spin Hamiltonian. Davies ENDOR is therefore suited to detect intermediate HFIs as illustrated in Fig. 5.17. Very large resolved HFIs in disordered system, however, cannot be addressed by ENDOR due to inhomogeneous broadening

of the ENDOR resonance lines. In that case one better resorts to the EPR spectrum where large HFIs are usually resolved. However, in order to exploit the full potential of Davies ENDOR, optimal conditions have to be chosen since the technique has a very low sensitivity. The experiment has to be carried out at high-field (Q-Band) to increase the polarization of the spin system, stochastic excitation has to be applied to avoid heating effects of the baseline and asymmetric ENDOR intensities due to nuclear spin relaxation and the optimal pulse length for the initial inversion pulse has to be used. Only by these extensive optimizations of the Davies ENDOR technique, the current sensitivity and resolution could be obtained.

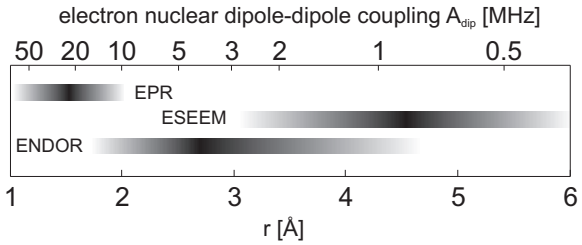

Figure 5.17: Illustrative overview of the applicability of various electron spin resonance techniques to determine hyperfine couplings and therefore the distance between H and DBs for the special case of DBs in disordered amorphous silicon (g = 2.0055). The optimum sensitivity is gained in the dark shaded area. The anisotropic electron-nuclear dipole-dipole coupling A_{dip} is calculated within the point-dipole approximation.

Fig. 5.18 shows the measured ENDOR response of native defects in sample A for different microwave inversion pulse length scaled to the ENDOR efficiency F_{ENDOR}

$$F_{\mathrm{ENDOR}} = 1/2\left[I_{\mathrm{echo}}(\mathrm{RF_{off}}) - I_{\mathrm{echo}}(\mathrm{RF_{on}})\right]/I_{\mathrm{echo}}(\mathrm{RF_{off}}) \tag{5.4}$$

where I_{echo} is the intensity of the inverted echo in the Davies-ENDOR pulse sequence (cf. sec. 3.2.1). For an inversion pulse length of 600 ns, an intense ENDOR response centered at the ^{1}H free nuclear precession frequency ν_0 = 52 MHz is observed (Fig. 5.18).

The spectral position of the observed ENDOR resonances can be explained by the effective spin Hamiltonian of an electron spin S = 1/2 coupled to a nuclear spin I = 1/2 [21]. For an axially symmetric hyperfine tensor, the resonance frequencies of the

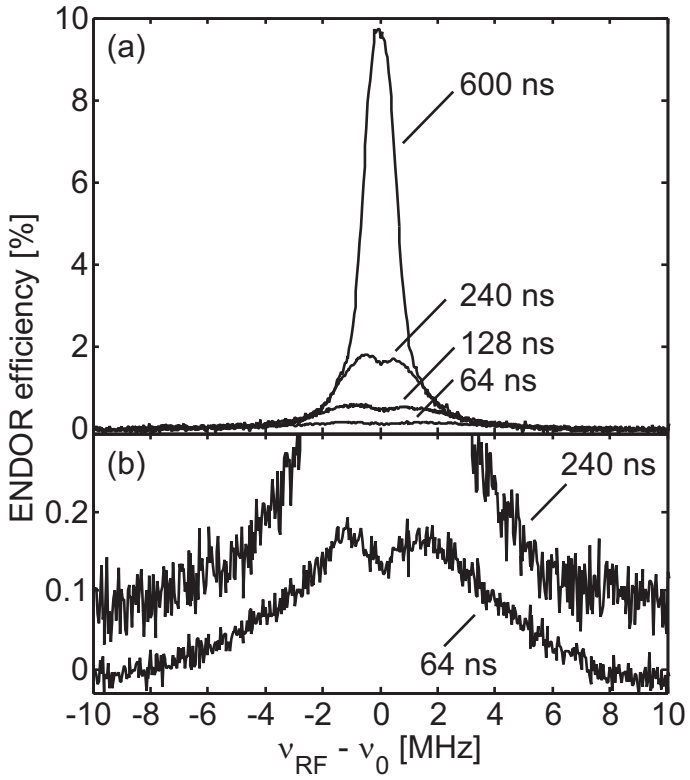

Figure 5.18: ENDOR spectra of native defects in sample A taken at $g = 2.0055$ with different length of the initial microwave inversion pulse. Davies ENDOR pulse sequence: $\pi - \mathrm{RF} - \pi/2 - \tau - \pi - \mathrm{echo}$ (for details cf. sec. 2.5). A total of 3000 averages were recorded for each pulse length. Decreasing the length of the inversion pulse results in a suppression of the central line (matrix line) (a) and an enhanced signal-to-noise ratio for strongly coupled H nuclei (b). The upper data trace in (b) is offset for clarity.

nuclear spin transitions in the two electron spin manifolds α and β excited by the RF pulse are given by

$$\omega_{\alpha(\beta)} = \omega_I \pm \left[\frac{A_{\mathrm{iso}}}{2} + \frac{A_{\mathrm{dip}}}{2}(3\cos^2\theta - 1)\right] \tag{5.5}$$

if the anisotropic electron-nuclear dipole-dipole coupling A_{dip} is small ($A_{\mathrm{dip}} \ll \omega_{\mathrm{I}}$). The ENDOR spectra are then symmetric about $\omega_{\mathrm{I}} = 2\pi\nu_0$. A_{dip} can be approximated by the point-dipole approximation (cf. Eq. 2.13) in which case A_{dip} is proportional to r^{-3} and increases if the nuclei are located closer to the electron spin (cf. Fig. 5.17). The random distribution of paramagnetic centers in the disordered solid and the sample powder distribute the resonance frequencies $\omega_{\alpha(\beta)}$. ENDOR powder spectra were obtained by averaging $\omega_{\alpha(\beta)}$ over the unit sphere (in this case over θ - the relative orientation of the electron-nucleus axis and the external magnetic field vector) where we assumed that the relative orientation between the paramagnetic center and nuclei in its vicinity are uncorrelated (full orientational disorder). The central ENDOR signal, in literature generally referred to as the matrix line [110], is ascribed to a large number of purely dipolar coupled H nuclei far away from the defect center ($r > 4$ Å) (distant nuclei). Close lying H atoms ($r < 3$ Å) exhibit a larger dipolar hyperfine interaction A_{dip} and a non-zero isotropic hyperfine interaction A_{iso}. Compared to the ENDOR response from the distant nuclei, the close lying nuclei give only rise to a small ENDOR signal intensity and were therefore not observed in earlier ENDOR experiments which were performed in a continuous mode (c.w. ENDOR) [111, 112] instead of pulsed mode as reported here. The ENDOR signal from these nuclei can be enhanced by increasing the excitation bandwidth of the initial microwave inversion pulse, i.e. decreasing its length [113]. This manifests itself in an enhanced signal-to-noise ratio in the spectra in Fig. 5.18. At the same time the ENDOR response from distant nuclei with a small hyperfine coupling is suppressed due to a complete inversion of both electron spin manifolds by the non-selective inversion pulse [114]. As a result a hole is burnt into the central part of the ENDOR signal, often referred to as the Davies hole. Since the width of the spectral hole scales linearly with the reciprocal inversion pulse length, it is obvious that the resulting doublet structure ($\nu_{\mathrm{RF}} - \nu_0 = \pm 1$ MHz in Fig. 5.18) is not caused by a predominant species of H nuclei with an isotropic hyperfine interaction similar to the width of the spectral hole. Instead it represents an experimental artifact due to the suppression of the matrix line. The signal-to-noise ratio for the low ENDOR signal intensity originating

from strongly coupled H nuclei is optimized by decreasing the length of the microwave inversion pulse to 40 ns (cf. Fig. 5.19).

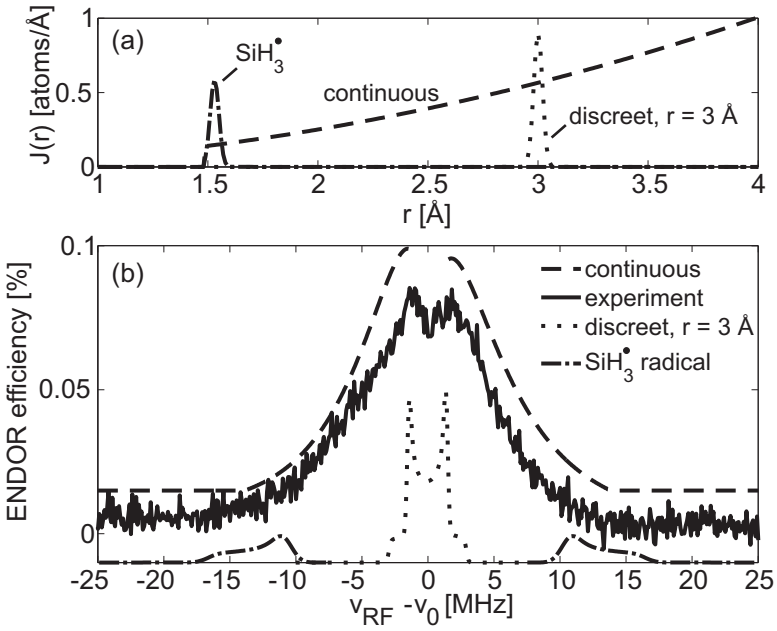

Figure 5.19: (a) Radial distribution function $J(r)$ for a continuous (dashed line) and discreet (dotted line) distribution of H atoms around DBs. The position of H atoms in free $SiH_3^\bullet$ radicals is shown by the dash-dotted line. (b) Corresponding ENDOR spectra for distributions in (a) and comparison with the experimental spectrum with an inversion pulse length of 40 ns. In (b) the dashed, the dotted and dash-dotted spectra are offset vertically with respect to the experimental spectrum for better overview.

The unstructured shape of the ENDOR spectrum proves that a broad distribution of hyperfine coupling constants exists. The broad distribution shows that the location of H atoms is not limited to discreet positions, which would result in distinct powder spectra (Pake-pattern) (dotted line in Fig. 5.19). Instead H atoms are continuously distributed around DBs and the distribution is characterized by a radial distribution function (RDF) $J(r)$. The RDF is an isotropic correlation function and is proportional to the number of nuclei on a sphere with radius r. In the case of a homogeneous H density, the RDF is given by $J(r) = 4\pi r^2 n_H$ and is proportional to r^2, since the surface area is simply proportional to r^2. For illustrative purposes the ENDOR spectrum can be simulated from $J(r)$ by a summation of the ENDOR powder patterns calculated for the individual

distances weighted with $J(r)$ (dashed line in Fig.5.19). The simulation is normalized to the experimental spectrum. The central part (matrix line), which is of no further interest for our study, is neglected, since a simulation of the matrix line or its suppression generally requires complex numerical calculations [115]. The simulation is in qualitative agreement with the experimental data (cf. Fig. 5.19) which shows that the H atom distribution is indeed in good approximation homogeneous. No evidence for a preferred microscopic structure with a definite hyperfine coupling or a spatial correlation is found, since it would lead to a deviation from the monotone shape of the ENDOR spectrum. It is important to realize that the homogeneous distribution of H atoms indicates that the number of H atoms in the vicinity of the defect is not fixed but varies from site to site.

As depicted in Fig. 5.17, we can translate the hyperfine coupling into a value for the distance between H atoms and DBs with the point-dipole approximation for A_{dip} (cf. Eq. 2.13). For H atoms at distances larger than 3 Å, A_{iso} is much smaller than A_{dip} and can be neglected, since the localization radius of the DB wave function is $r_{\mathrm{DB}} \approx 3$ Å [73]. For a distance of 3 Å, the hyperfine coupling then amounts to $2A_{\mathrm{dip}}$= 5.8 MHz, which is significantly lower than the hyperfine couplings observed in the ENDOR spectrum in Fig. 5.19. If no H atoms are located at distances closer than 3 Å from the DB, the ENDOR signal intensity will be exactly zero for hyperfine couplings larger than $2A_{\mathrm{dip}}$= 5.8 MHz (dotted line in Fig. 5.19). This proves that some H atoms are situated at distances smaller than 3 Å from the DB. For these strongly coupled H atoms the point-dipole approximation is not applicable and A_{iso} is no longer negligible. In this regime, a reasonable structural assignment can only be established by the comparison of the experiment with model systems or quantum chemical calculations. A prominent model system for the DB in a-Si:H is given by the free $SiH_3^{\bullet}$ radical. The expected ENDOR resonance positions for the coupling between the DB electron spin and the nuclear spin of the H atoms in this molecule are shown in Fig. 5.19 (dash-dotted line) (A_{iso} = 25 MHz, A_{dip} = 4 MHz [116]). The experimental ENDOR spectrum of a-Si:H clearly shows a non-zero intensity at these spectral positions which proves that H atoms can also occur at the back-bonds of DBs. The reduced spectral intensity at large hyperfine couplings compared to the central ENDOR resonance indicates that DBs with H atoms in a back-bonded position are a minority in a-Si:H while the majority of DBs is only remotely connected to H atoms. This, however, does not imply that the probability of finding H

atoms at a certain point of space is smaller or different in the vicinity of DBs than it is in a region without DBs. Instead the above discussion of the experimental ENDOR data suggests that this probability is a constant for every point in the sample (homogeneous distribution). In other words, there is no anti-correlation of H atoms and DBs, i.e. H atoms avoid bonding to DB Si atoms, as was proposed in an earlier model [73, 117]. The basic assumption of this model is that the release of local strain in the network is the driving force for DB formation. The authors of Ref. [73, 117] argue that the probability of finding a H atom back bonded to DB Si atoms is very small, since the H bonding would have already decreased the bond coordination. Hence the formation of a DB is no longer necessary to approach a local free energy minimum during the growth of the material. With the experimental findings of this work in mind, it is unlikely that such a simple model can explain the defect reactions during growth of the material and a revision of the model seems necessary. It is interesting to note that this model, which accounts for the creation of native DBs, is different compared to models dealing with the formation of light-induced DBs. While Si-Si bonds connected to Si-H bonds are excluded as precursors for the formation of native DBs in the above mentioned model, they are explicitly included in the weak Si-Si bond breaking model proposed to explain the SWE (cf. sec. 5.1 and Ref. [15]). Additional insight concerning this issue can be gained by comparing the H distribution around native and light-induced defects. The results of this study will be discussed in the next section.

5.3.2 Hydrogen distribution in the vicinity of light-induced defects

The preceding analysis of the H distribution around native coordination defects in a-Si:H revealed that the H atoms are homogeneously distributed. Theoretical models of the SWE predict that this should not be the case for light-induced defects. According to specific SWE models the defect density is increased upon light soaking by a generation of intimately correlated DB-H pairs. For such a defect configuration one expects a rather large A_{dip} due to the small distance between the DB defect and the H atom. Values for A_{iso} are difficult to predict due to the importance of spin-polarization effects. The magnitude of A_{iso} can be large > 50 MHz or small < 1 MHz depending on the sign and size of the exchange coupling between the unpaired electron spin and the paired electron spins in the Si-H bond. The HFI of intimately correlated DB-H pairs should majorly

change the ENDOR spectrum upon light soaking of the a-Si:H sample. Fig. 5.20 a) shows a comparison of ENDOR spectra of sample C in the light-soaked and annealed state.

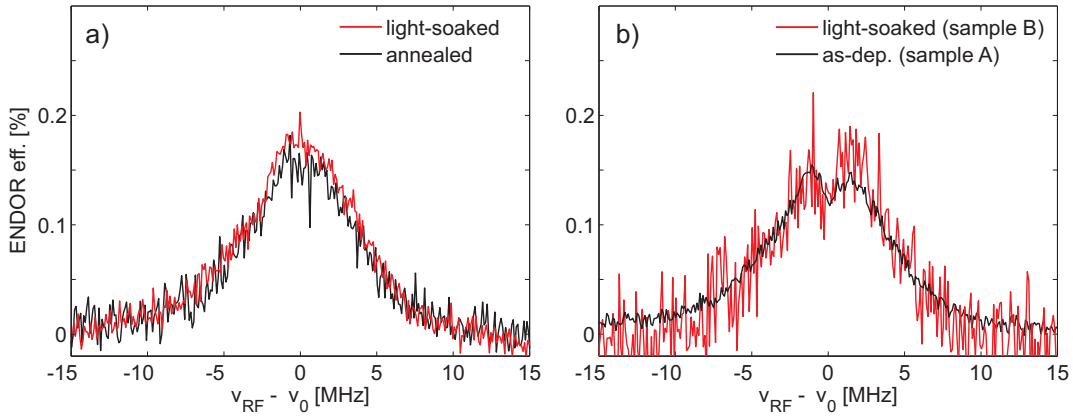

Figure 5.20: Pulse Davies ^{1}H-ENDOR recorded at Q-Band microwave frequency and at a temperature of T = 80 K. The length of the inversion pulse length was T_{inv} = 64 ns. Free Larmor precession frequency of nuclear spins of H atoms at a magnetic field of 1.2 T: $\nu_0 \approx 52$ MHz. Accumulation time for ENDOR spectra 1 - 2 days. a) Comparison of ^{1}H-ENDOR spectra of sample C in the light-soaked and annealed state. b) Comparison of the ^{1}H-ENDOR spectra of sample B in the light-soaked state and sample A in the as-deposited state.

The ENDOR spectra are identical within the signal-to-noise ratio and do not show any evidence for the presence of intimately correlated DB-H pairs. However, the difference in the defect density between the light-soaked and annealed state of sample C is rather small ($N_s = 4.3 \cdot 10^{16}\,\mathrm{cm}^{-3} \rightarrow 5.3 \cdot 10^{16}\,\mathrm{cm}^{-3}$), hence the ENDOR spectra presented in Fig. 5.20 a) still contain a large contribution arising from native coordination defects. In case of device grade samples (sample B), the defect density increases by as much as a factor of 10, hence the ENDOR spectrum is dominated by light-induced defects and contributions from native defects are negligible. However, the small defect density makes it impossible to determine the ENDOR spectrum of sample B in the annealed state. Hence, the ENDOR spectrum in the light-soaked and annealed state cannot be compared in the case of sample B. Instead, the light-soaked state is compared with the ENDOR spectrum of native defects in as-deposited a-Si:H (cf. Fig. 5.20 b). Again, the ENDOR spectra are identical within the signal-to-noise ratio and do not show any

evidence for the presence of intimately correlated DB-H pairs. In fact, considering the complete set of ENDOR spectra for all samples as shown in Fig. 5.20, one realizes that within the signal-to-noise ratio all samples exhibit the same ENDOR spectrum. Hence, the ENDOR spectrum of native as well as light-induced defects in a-Si:H is universal and does not depend on the material state and the deposition conditions. It is therefore very likely that there are no major changes in the H distribution of light-induced defects.

5.3.3 Spatial correlation between light-induced defects and H atoms

In summary, pulse ^{1}H-ENDOR experiments show that H atoms are continuously distributed around native coordination defects in as-deposited a-Si:H. No correlation between the defects and H atoms is observed and the H atoms are presumably homogeneously distributed in the network. However, the ENDOR spectra show contributions from H atoms with HFIs up to 30 MHz. This indicates that H atoms can be located very close ($r < 3$ Å) to the coordination defects. If the coordination defects are seen as DB defects, one can conclude that the spectral contributions at large HFIs (25 - 30 MHz) indicate that a minority of DBs carry H atoms at their backbonds.

^{1}H-ENDOR measurements of light-induced defects show very similar results as obtained for native defects. No evidence for a spatial correlation between light-induced defects and H atoms, as predicted by the weak Si-Si bond breaking model, is found. However, the implications of the ENDOR results for the various SWE models are complex. Each defect reaction (cf. sec. 5.1) has to be discussed in detail since each slightly different structures of the final metastable state are predicted. In addition, the presented ENDOR spectra are subject to certain experimental limitations. In the following, the experimental limitations of ENDOR are described and a detailed discussion of each SWE defect reaction is presented. This discussion will decide which model can be confirmed, discarded or which models cannot be tested by the present ENDOR measurements.

In sec. 5.1 we have seen that several defect reactions can yield a metastable increase of the defect density. The basic microscopic processes of the weak Si-Si bond breaking model are

1. Si-H + Si-Si →Si-DB* + (Si-H/DB*-Si), Ref. [15, 91]
2. Si-H/Si-H + Si-Si →2(Si-H/DB*-Si), Ref. [92, 93]

3. Si-H/H-Si + Si-Si →2{Si-H/DB*-Si} Ref. [94].

The defect reactions predict either one or two spatially correlated defect states with the H atom on the bond centered (BC) site (Si-H/DB*-Si), or two spatially correlated defects states 2{Si-H/DB*-Si} with the H atom on a tetrahedral like site (T_d). The distance between the H atom and the DB is about 2 Å for the BC site and 4-5 Å for the T_d site. The dipolar HFI A_{dip} between the DB electron spin and the nuclear spin of the H atom is large in the first case and small in the second case. Let us assume that the H atoms spatially correlated with light-induced defects exhibit a normal distribution of isotropic and dipolar HFIs A_{iso} and A_{dip}. In the following, the mean values of the distributions of A_{iso} and A_{dip} are denoted by $\langle A_{iso}\rangle$ and $\langle A_{dip}\rangle$ and the standard deviations by σ_{iso} and σ_{dip}.

In case of defect reaction (2) each DB is spatially correlated to a H-atom and $\langle A_{iso}\rangle$ of (Si-H/DB*-Si) states can take very high values due to a significant spin density of the unpaired electron at the site of the H atom. If $\langle A_{iso}\rangle$ of these H atoms is larger than the line width of the EPR spectrum (about 1 mT for S- or X-Band), a splitting of the resonance line will occur. Please note that in case of a large σ_{iso} and in case of a finite A_{dip} and σ_{dip} the splitting may not be resolved, instead a strong broadening of the EPR spectrum occurs. Since this is not observed one can conclude that $\langle A_{iso}\rangle$ and $\langle A_{dip}\rangle$ are presumably smaller than 1 mT ($\approx$ 30 MHz). The experimental ENDOR spectra show that H atoms with a HFI between 0 and 30 MHz indeed exist. However, there are major problems in this range of HFIs. Resonance lines of intermediate HFIs (10 MHz < $\langle A_{iso}\rangle$,$\langle A_{dip}\rangle$ < 30 MHz) can be excessively broadened by A-strain (σ_{iso},σ_{dip}> 10 MHz). It is therefore not possible to definitely exclude the presence of light-induced (Si-H/DB*-Si) states. One can, however, conclude that the mean HFI $\langle A_{iso}\rangle$ and $\langle A_{dip}\rangle$ of such defect configurations has to be smaller than 30 MHz.

Defect reaction (1) predicts that only half of the defects are spatially correlated to H atoms and the other half are isolated DB defects. Stutzmann et al. [46] argued that $\langle A_{iso}\rangle$ and $\langle A_{dip}\rangle$ is larger than 100 MHz and the HFIs are widely distributed (large σ_{iso} and σ_{dip}). As discussed above, this would lead to a strong broadening of the EPR resonance line of the light-soaked a-Si:H samples. In this model the correlated defects (Si-H/DB*-Si) exhibit a large HFI and are therefore not observable in the EPR spectrum due to excessive broadening (hidden HFI line). The uncorrelated defects Si-DB* exhibit a homogeneous H distribution as in the case of native defects and their EPR resonance line remains

narrow. This would imply that not all singly-occupied defects present in the mobility gap of a-Si:H contribute to the EPR spectrum with a g-value of $g = 2.0055$. The EPR measurements presented in this thesis do not show the presence of a hidden HFI line. An equal light-induced increase of correlated (Si-H/DB*-Si) and isolated DB defects Si-DB* remains to be either confirmed or ruled out by further experimental investigations.

Defect reaction (3) predicts the generation of two spatially correlated {Si-H/DB*-Si} states, where the distance between the H atom and the DB is about 4-5 Å. At such a large distance $\langle A_{dip} \rangle$ can be estimated within the point-dipole approximation (cf. Eq. 2.13), $\langle A_{dip}(4-5 \text{ Å}) \rangle$ = 0.6 - 1.2 MHz. $\langle A_{iso} \rangle$ is also small due to the negligible spin density of the electron spin at the site of the H-atom. Unfortunately, such a small HFI ($\langle A_{iso} \rangle$ and $\langle A_{dip} \rangle$ < 2 MHz) cannot be detected by ENDOR since the technique exhibits a blind spot in this region (Davies hole). The width of this blind spot can be decreased by increasing the length of the microwave inversion pulse. However, the large abundance of matrix nuclei (H content of a-Si:H is about 10 at. %) makes it impossible to detect a redistribution of H-atoms with a small HFI. Although the small HFI predicted by defect reaction (3) is in principle in agreement with the ENDOR experiments, the model cannot be tested with this technique.

The above discussed defect reactions all result in a generation of metastable spatially correlated Si-H/DB*-Si. The H collision model does not rely on the generation of these metastable states. The defect reaction of the H collision model is given by 2(Si-H) + Si-Si $\rightarrow$ 2(Si-DB*) + Si-H/H-Si [96]. The DB defects generated within the H collision model exhibit no spatial correlation to H atoms. This does, however, not mean that the vicinity of each DB is depleted from H. As we have shown for native coordination defects, a small minority of defects exhibits H atoms in their direct vicinity. The H distribution around light-induced defects is again homogeneous as in the case of native coordination defects since the experimental ENDOR spectra do not change by light-soaking (cf. Fig. 5.20). The ENDOR spectra indicate that the distributions of metastable defects and H atoms are not correlated, that is, not very defect has a H atom in its vicinity. Only a very small minority of defects exhibits this correlation.

5.4 Conclusion

In this section the obtained results are discussed in the context of theoretical SWE models. It was shown, for the first time, that the common believe of native and light-induced defects exhibiting the same EPR spectrum is incorrect. This observation suggests that the microscopic origin of light-induced defects cannot be attributed to DB defects. This is a drastic issue since theoretical models explaining the SWE on a microscopic level explicitly assume that native and light-induced defects are DB defects. The only difference between the models is the spatial defect distribution and the defect environment. In addition, the investigation of the spatial correlation between H-atoms and light-induced defects by ^{1}H-ENDOR showed no evidence in favor for models which propose the generation of DB-H pairs. However, it is important to say that on the present experimental ground the weak Si-Si bond breaking model cannot be disproved conclusively.

It is clear that the observation of a change in the EPR spectra between native and light-induced defects cannot be intuitively explained within any of the SWE models discussed in this thesis. At this point one can only speculate about the microscopic structure of light-induced defects. It was shown that the EPR spectrum of these defects is narrower than the EPR spectrum of native coordination defects which can only be caused by a reduction of the g-tensor anisotropy. The experimental observation that the transversal relaxation properties of light-induced defects are distinctly different from native coordination defects is a further prove that the defects are of different origin. Spins of light-induced defects relax much faster than spins of native defects. One possibility for this fast echo decay is a clustering of light-induced defects. This is in principle predicted by the weak Si-Si bond breaking models (defect reaction 1,2 and 3) which do not propose a further separation of the metastable defects by H diffusion. In these models the DBs in the metastable state exhibit a distance between them of about 4 - 10 Å, which would result in a very large dipolar spin-spin coupling of about 50 - 800 MHz. However, at such small distances exchange interaction is significant, which could lead to the formation of a singlet or triplet state, which is clearly not observed. It is therefore unclear whether a cluster of only one spin pair is enough to explain the observed behavior.

Another important issue is the observation that the HFI values for native coordination defects do not match those obtained for computer generated DBs, as outlined in chapter

4. In view of this result and the investigation of light-induced defects, significant doubt arises whether the defect structures are at all close to the atomic configuration of a DB.

6 ED-ESEEM a new technique for the investigation of defects in thin-film silicon solar cells

The previous chapters brought new insight into the microscopic origin of defects in a-Si:H powder samples by the application of advanced EPR techniques. These powerful methods should now be applied to investigate defects in fully-processed thin-film solar cells. The presented EPR techniques are, however, by far not sensitive enough to be applied to thin-film solar cells of device grade, which exhibit only a small number of defects. This problem will be solved by using EDMR. This chapter presents the implementation of a novel spectroscopic EDMR technique to determine unresolved HFIs of paramagnetic defects or impurities in thin-film solar cells. The developed technique is a combination of high-sensitivity pulse EDMR methods and ESEEM, a routinely applied pulse sequence in conventional EPR to detect small HFIs. A proof-of-principle implementation of the novel ED-ESEEM method is presented and the technique is applied to e- and CE-centers in µc-Si:H thin film silicon solar cells. The measurements show that electron spins of e-centers are weakly coupled to ^{29}Si, ^{31}P and ^{1}H nuclei. ED-ESEEM measurements of CE-centers show that the immediate vicinity of the defect is depleted from ^{31}P and ^{1}H nuclei. The CE-centers are therefore attributed to shallow defect states in the crystalline grains of the µc-Si:H absorber layer and not to interface defect states at the boundary between amorphous and crystalline phases of µc-Si:H.

6.1 Introduction

Spectroscopic techniques to detect small HFIs masked by inhomogeneous line broadening are important to investigate the microscopic structure of paramagnetic defects or impurities in thin-film solar cells. Conventional EPR provides high resolution spectroscopic tools, such as ENDOR or ESEEM to solve this problem. However, these techniques are usually inapplicable in materials containing less than 10^{10} paramagnetic centers, which is frequently the case in device grade thin film silicon solar cells. For charge transport determining paramagnetic defects this limit can be lifted by detecting resonant changes in the (photo-) current instead of EPR induced changes of the microwave absorption [118]. Electrically detected magnetic resonance (EDMR) actively manipulates spin pair recombination or hopping rates and probes the resulting conductivity changes with a detection sensitivity down to $\approx$ 100 spins [39]. Thereby EDMR is capable of combing ultra-high sensitivity with nanoscopic identification of electronic states involved in spin-dependent charge transport and loss mechanisms in semiconductors. The introduction of pulse (p)EDMR methods [119] lead to recent progress in semiconductor devices by identifying the contributing paramagnetic sites by their g- and HFI-tensors [50], discriminating between alternative spin-dependent transport pathways exhibiting different dynamics [50] and determining electron spin-spin interactions [120] as well as electron-spin coherence properties [121–123]. Large resolved HFIs of phosphorus donors in crystalline silicon were recently probed by electrically-detected ENDOR experiments [124, 125]. Despite these breakthroughs, pEDMR up to now was not capable of providing small unresolved HFIs (typically smaller than 20 MHz) in disordered materials where inhomogeneous broadening due to a distribution of g- and HFI-values prevails. In order to overcome this limitations, we developed a novel pEDMR detection scheme for electrically detected (ED)-ESEEM. By employing this method to a multi-layer thin-film a-Si:H/µc-Si:H solar cell with few electron spins (number of spins $\approx 10^4$), we observed first electrically detected spin echo modulations.

6.2 Experimental results

The transient current response of the sample was recorded by a current amplifier and integrated from 3-8 µs for spin echo measurements to obtain a charge ΔQ. A detailed description of the experimental setup can be found in sec. 3.2.3 and Ref. [50].

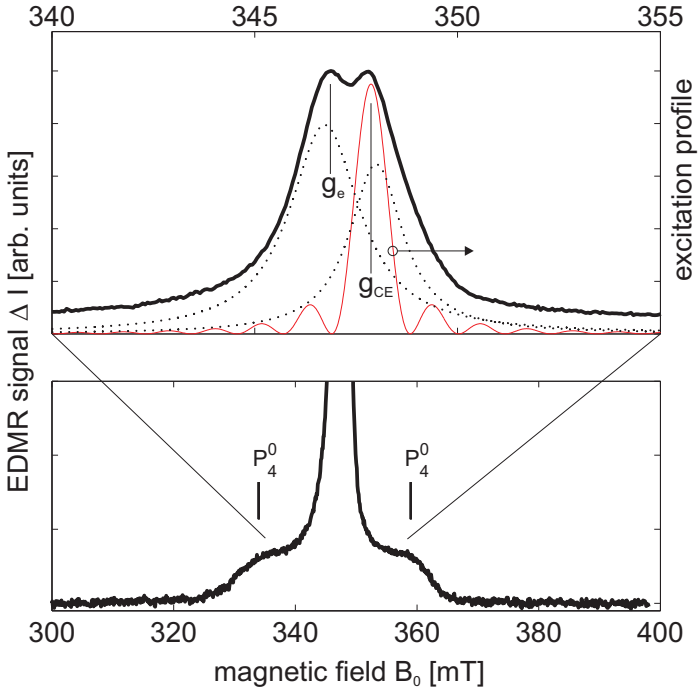

Figure 6.1: Field-swept pEDMR spectrum are recorded by monitoring the transient current change (ΔI) 3 µs after a 100 ns π-pulse. The spectrum shows narrow resonances attributed to e and CE centers in addition to a broad resonance of P_4^0-donor states split by a large isotropic HFI. Deconvoluted pEDMR spectra are shown by the dotted lines. The excitation profile of the microwave pulse sequence is shown by the red solid line. ESEEM measurements are carried out at magnetic field positions indicated by g_e and g_{CE}.

Fig. 6.1 shows the field swept pEDMR spectrum recorded as a transient current change 3 µs after a 100 ns microwave π-pulse. The spectrum exhibits two partly overlapping narrow signals with g_e = 2.0045(5) and g_{CE}= 1.9975(5), respectively and a 25 mT broad signal centered around g_P = 2.003 (Fig. 6.1). In a previous study these signals have been assigned to spin-dependent transport between conduction band tail states (e) (g_e = 2.0045(5)) and neutral fourfold-coordinated P_4^0-donor atoms (g_P = 2.003) in the n-a-Si:H

emitter layer [126]. The HFI between the P_4^0-donor electron and its host ^{31}P nucleus is on average 25 mT [44] and therefore separates the e-center from the P_4^0-donor transitions. The remaining signal has been assigned to hopping transport among conduction band tail states (referred to as CE centers, g_{CE} = 1.9975(5)) in the µc-Si:H absorber layer [50]. This spatial assignment of spin-dependent processes to individual layers of multi-layer devices is usually done by comparing the g-values to those in literature studies of isolated a-Si:H and µc-Si:H layers obtained by either EDMR, optically-detected magnetic resonance (ODMR), EPR or light-induced EPR. However, the assignment of EDMR signals in multi-layer devices such as silicon thin-film p-i-n solar cells is complicated by the fact that these devices exhibit complex charge-carrier transport processes, which are not restricted to the bulk of the individual layer but can also take place at their interfaces [127]. Another possibility to identify the spatial origin of the EDMR signals is a subsequent alternation of the device layers [50], which however exhibits the severe disadvantage that in state-of-the art thin film solar cells a layer modification usually alters the growth boundary conditions for other layers. A spectroscopic solution of this problem, which is non-invasive and does not rely on a comparison with earlier studies on different devices, exploits the HFI between the electron spin with its surrounding magnetic nuclei. By this method the chemical composition of the layer material (e.g. dopants, impurities and alloy composition) as well as the spin-density distribution of the paramagnetic defect state in the lattice can be deduced [128]. Since the determination of small HFI in the pEDMR spectrum is prevented by inhomogeneous broadening, ENDOR or ESEEM techniques have to be applied [21]. The implementation of ENDOR in electrical detection schemes is technically demanding, due to inductive coupling of RF-radiation to the detection circuit and were realized only for the detection of large resolved HFIs in crystalline systems [124, 125] or in low-power continuous wave mode [129]. ESEEM techniques, relying solely on microwave pulses, are therefore favored for electrical detection. ESEEM is based on a two-pulse sequence $\pi/2-\tau_1-\pi-\tau_2-\text{echo}$ where coherences are refocused at $\tau_2 = \tau_1$ to generate a spin echo, whose amplitude is measured as a function of $\tau = \tau_1$. For electrical detection of the spin echo the standard two-pulse ESEEM sequence is augmented with a $\pi/2$ readout pulse at the time of echo formation to transfer electron coherence to polarization [122] (cf. inset Fig. 6.2).

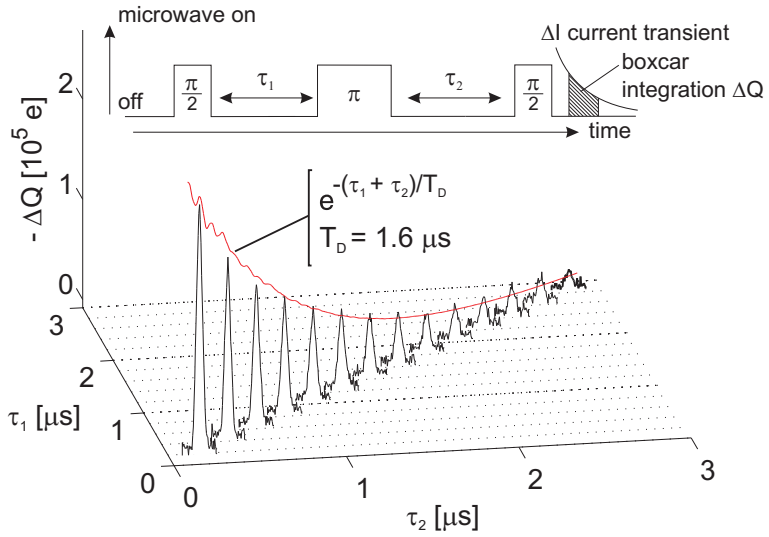

Figure 6.2: Electron-spin echo decay of e-centers (g_e = 2.0042) after subtraction of a linear background. The echo decays approximately mono-exponentially with a time constant T_D = 1.6 µs. The inset shows the applied microwave pulse sequence together with a schematic current transient after the last read-out pulse, which serves as the observable in an ED-ESEEM experiment.

Processes in EDMR involve correlated spin pairs, which consist of two $S = 1/2$ electron spins S_1 and S_2 and can be described within the coupled radical pair model [130]. We consider only e-centers (S_1) and P_4^0 donors (S_2) spin pairs, transitions between CE states are described in a similar way. In addition we assume that the spin pair is weakly coupled (cf. sec. 2.7.2). S_1 is coupled to an arbitrary nuclear spin $I_1 = 1/2$ and S_2 is coupled to its ^{31}P nuclear spin $I_2 = 1/2$. If the HFI between the excited electron spin (S_1) and I_1 is anisotropic, ESEEM is induced by the formation of coherence-transfer echoes [131,132]. In the following, we consider the coherence on the allowed S_1 transition (1,5) only, other coherences behave in an analogous way (cf. sec. 2.7.2). The coherences on transition (1,5) are generated by the initial $\pi/2$ pulse and accumulate a phase proportional to their eigenfrequency ω_{kl} during the first free evolution period (cf. Fig 6.3b-I/II). Due to the pseudo-secular HFI, there is also a certain probability that the EPR π pulse also flips I_1. This induces a coherence transfer to other transitions (mn) with a different eigenfrequency ω_{mn} (cf. Fig 6.3b-III). During the second evolution period a different phase is acquired and the observable coherence-transfer echoes refocus along a different axis than the original coherence on (1,5) (cf. Fig 6.3b-IV).

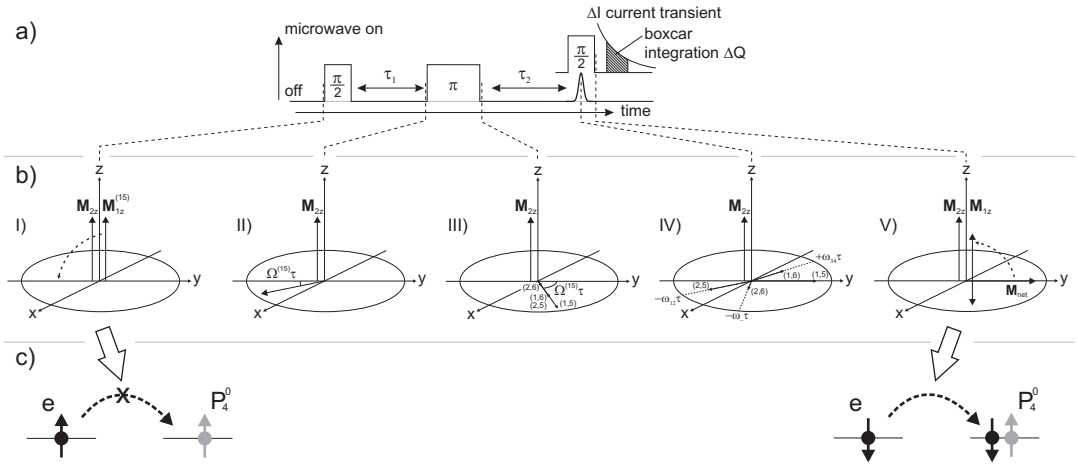

Figure 6.3: a) Applied microwave pulse sequence together with a schematic current transient after the last read-out pulse. b) Evolution of polarization and coherence on the allowed transition (1,5) of S_1 in the laboratory frame during the pulse sequence shown in a). I) S_1 and S_2 are ordered longitudinally before the pulse sequence. II) Longitudinal magnetization (**M**) on (1,5) is flipped to the x-y plane by the $\pi/2$-pulse and gains a phase $\Omega^{(15)}\tau$ during the first free evolution period. III) The π-pulse inverts the phase and redistributes the magnetization between four allowed and forbidden electron spin transitions of S_1. IV) At the time of echo formation the different coherences gained a certain phase relative to the coherence on transition (1,5). V) The final $\pi/2$ pulse converts coherences back to polarization, which is now reduced as compared to the initial polarization. The level scheme and transition frequencies of the spin system are given in sec. 2.7.2 c) Spin-dependent hopping transition between the e-center (S_1) and the P_4^0 center (S_2). The triplet longitudinal spin order in the initial state before the pulse sequence prohibits charge carrier hopping due to the Pauli Exclusion Principle. In the presence of ESEEM, the reduced polarization of S_1 after the pulse sequence can be visualized by a certain population of spins S_1 which are anti-parallel to S_2 and therefore allow carrier hopping, increasing the overall photocurrent of the sample.

Since all coherence-transfer echoes refocus at the same time, the echo envelope is modulated with the difference frequencies $\omega_{mn} - \omega_{15}$, which are the nuclear frequencies [21, 133, 134]. Quantitatively, the two-pulse ED-ESEEM echo intensity as a function of τ under selective excitation of S_1 is given by (cf. sec. 2.7.2)

$$I_{2p}(\tau) = 1 - \frac{k}{4}(2 - 2\cos\omega_\alpha\tau - 2\cos\omega_\beta\tau + \cos\omega_+\tau + \cos\omega_-\tau) \qquad (6.1)$$

with the nuclear frequencies of I_1: $\omega_\pm = \omega_\alpha \pm \omega_\beta, \omega_{\alpha/\beta} = \sqrt{(\omega_{I_1} \pm A/2)^2 + B^2/4}$, and the modulation depth parameter $k = \left(\frac{B\omega_{I_1}}{\omega_\alpha\omega_\beta}\right)^2$. For an axially symmetric HFI between S_1 and I_1 the secular and the pseudo-secular part can be expressed as $A = A_{iso} + A_{dip}(3\cos^2\theta - 1)$and $B = 3A_{dip}\sin\theta\cos\theta$, where A_{iso} and A_{dip} denote the isotropic and anisotropic HFI, respectively and θ indicates the angle between the external magnetic field and the electron-nucleus axis [21]. Since the online monitoring of spin coherence as in conventional EPR is not possible in EDMR, the echo decay is recorded in a two-dimensional (2D) experiment, where the second delay τ_2 is varied for a fixed value of the first delay τ_1 around the echo top occurring at $\tau_1 = \tau_2$ [122]. Fig. 6.2 shows ΔQ as a function of τ_1 and τ_2 for e-centers after subtraction of a linear background. The echo decays approximately mono-exponentially with a fast decay time constant $T_D = 1.6\,\mu s$. To record ESEEM, we incremented the delay times simultaneously $\tau_1 = \tau_2 = \tau$ and eliminated the unmodulated part of the echo envelope through division by a polynomial fit. The remaining modulated part of the echo envelope is shown in Fig. 6.4 a).

Before Fast Fourier Transformation (FFT) the time traces were apodized by a Kaiser 2π window to obtain a high side-band suppression and zero-filled up to 4096 points. The upper curve in Fig. 6.4b shows the FFT of the e-center echo envelope. Several pronounced resonance peaks are observed at frequencies matching calculated ω_I or $2\omega_I$ of ^{29}Si, ^{31}P and ^{1}H nuclei, indicated by vertical lines in Fig. 6.4b. This proves that the observed ESEEM pattern originates from a large number of distant matrix nuclei with a weak anisotropic and negligible isotropic HFI, since only in this case the nuclear frequencies reduce to ω_I or $2\omega_I$. Since the maximum electron-nuclear distance detectable by ESEEM is about 8 Å, the observation of ^{29}Si and ^{1}H ESEEM and the absence of ^{11}B (I = 3/2, 80.1% relative abundance) ESEEM leads to the immediate conclusion that

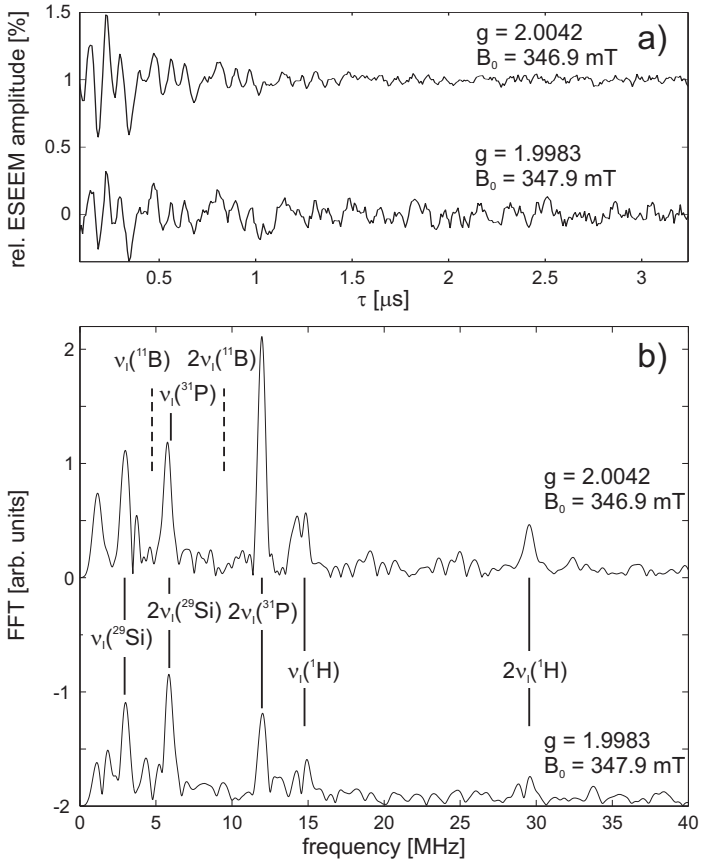

Figure 6.4: a) Electron-spin-echo envelope measured by simultaneously incrementing τ_1 and τ_2 and after division by a 9^{th}-order polynomial fit. Upper trace: e-states (g_{e} = 2.0042), lower trace: CE-states (g_{CE} = 1.9983). b) Magnitude FFT spectra of echo modulations in a) normalized to $2\omega_{I_1}(^{29}\text{Si})$ modulation. Vertical lines indicate computed ω_{I_1} and $2\omega_{I_1}$ for given magnetic nuclear isotopes.

the electronic processes are restricted to the n-a-Si:H or i-µc-Si:H layers of the solar cell. The observation of ^{31}P ESEEM shows that e-centers are located in the n-a-Si:H layer. It is however not immediately clear, whether the ^{31}P nuclei are part of the diamagnetic (P_3^0) or paramagnetic (P_4^0) atomic configuration of P impurities. In both cases, the ^{31}P nuclear spin will interact with the e-center's electron spin (S_1) via HFI, also in case the paramagnetic P_4^0 is the actual spin-pair partner of the e-center (special case $I_1 = I_2$). In the latter case, however, forbidden transitions involving a simultaneous flip of the electron and nuclear spin are shifted in energy relative to allowed S_1 transitions due to the large HFI between I and S_2 (cf. sec. 2.7.2). In this case the condition for a simultaneous excitation of allowed and forbidden transitions, a prerequisite for the observation of ESEEM [135], is not met due to a limitation of the experimental excitation bandwidth. We therefore attribute the ^{31}P nuclei to the P_3^0 configuration. This assignment is also supported by the fact that EDMR spin-pairs are weakly-coupled (cf. sec. 2.7.2) with a negligible electron-electron coupling, which indicates that the electron spins are separated by more than 3 nm, a value well beyond the detection radius of ESEEM ($\approx$ 8 Å). Having identified the nature and electronic configuration of the magnetic nuclei inducing ESEEM, we can now discuss their spatial distribution and concentration which is reflected in the ESEEM spectrum (cf. Fig. 6.4b). Using conventional ESEEM Yamasaki et al. [136] have shown that the global alloy composition is reasonably well described by the intensity ratio $\omega_+(^{31}\mathrm{P})/\omega_+(^{29}\mathrm{Si})$ of weakly coupled matrix nuclei. Although our ESEEM spectra are very similar to theirs, the $\omega_+(^{31}\mathrm{P})$ intensity clearly exceeds the $\omega_+(^{29}\mathrm{Si})$ intensity in our case (cf. upper trace Fig. 6.4b) and does therefore not reflect the global solid-phase concentration. This peculiarity constitutes the major difference between microwave detected ESEEM spectra on n-a-Si:H powder samples [136] and the ED-ESEEM spectra reported here. It is important to note that as long as the experiment is carried out at the same magnetic field the $\omega_+(^{31}\mathrm{P})/\omega_+(^{29}\mathrm{Si})$ intensity ratio shows only a minor dependence on the experimental conditions, such as the microwave pulse length and intensity, and is merely determined by the HFI of these nuclear isotopes and their distribution in the solid. We therefore conclude that the distribution and local concentration of P_3^0 or the microscopic structure of e-centers selected in ED-ESEEM differs from that of e-centers in n-a-Si:H powder samples (cf. Ref. [136]).

CE-states were investigated under otherwise identical conditions by slightly tuning the magnetic field to excite centers with g_{CE}= 1.9983. The resulting ESEEM spectra are similar to those of e-centers, but show a strong reduction of the $\omega_+(^{31}P)/\omega_+(^{29}Si)$ intensity ratio (cf. lower curve Fig. 6.4b). Although the exact distribution of ^{31}P and ^{29}Si nuclei around e-centers is yet unknown, the reduction of the $\omega_+(^{31}P)/\omega_+(^{29}Si)$ intensity ratio is a strong indication that much less ^{31}P nuclei are located around CE-centers. Even the residual contribution of ^{31}P ESEEM is attributed to an off-resonant excitation of e-centers by the broad excitation profile of the microwave pulses and does not arise due to HFI between CE-states and ^{31}P nuclear spins. This is verified by a numerical simulation of the π-pulse excitation profile (cf. Fig. 6.1), which shows that the employed microwave pulses still excite a rather large fraction of the e-center resonance. A quantitative simulation shows that the off-resonant e-center contribution is only reduced by a factor of two when tuning the magnetic field to g_{CE}, in excellent agreement with the experimental spectrum (cf. Fig. 6.4b). The residual ^{31}P ESEEM does therefore not originate from CE-centers and we conclude that ^{31}P nuclei are not significantly abundant around CE-centers, hence they are located in the undoped µc-Si:H absorber.

The same argumentation is valid for ^{1}H ESEEM observed in case of excitation of CE centers. The signal contributions at ω_I (^{1}H) or $2\omega_I$ (^{1}H) are reduced by about a factor of two as compared to e-centers and can again be assigned to an off-resonant excitation of e-centers. The CE centers alone do not show signal contributions at ω_I (^{1}H) or $2\omega_I$ (^{1}H), hence the centers are not coupled to distant H atoms. It is therefore very likely that the vicinity ($r < 6$ Å) of CE-centers is depleted from H atoms. This has important consequences for the microscopic origin of CE centers. Due to the lack of H coupling, observed before with conventional ESEEM in highly-crystalline µc-Si:H [43], the states must be located within a H free region of the material, most likely within crystalline grains. They cannot be located at the boundary between crystalline and amorphous phases of µc-Si:H since H is very abundant in the amorphous phase.

6.3 Conclusion

We demonstrated the electrical detection of ESEEM of e- and CE-centers in a-Si:H/µc-Si:H thin-film solar cells. Echo modulations arise due to highly-abundant matrix nuclei

(^{29}Si,^{31}P,^{1}H) which exhibit weak HFI to the paramagnetic sites. ESEEM of e-centers show a pronounced contribution due to ^{31}P nuclei, which indicates that e-centers are located in the n-a-Si:H layer. This contribution is strongly reduced in case of CE-centers which we conclusively assign to the undoped µc-Si:H absorber. Our experimental results therefore verify previous assignments of spin-dependent processes. It is argued that for CE-centers ESEEM signals arising due to HFI to ^{31}P and ^{1}H nuclei can be explained by an off-resonant excitation of e-centers by the short microwave pulses employed. CE-centers by themselves do not exhibit HFIs to distant ^{31}P and ^{1}H nuclei. It can be concluded that due to the lack of H coupling, CE-centers are located within crystalline grains and not at the boundary between amorphous and crystalline phases of µc-Si:H.

The presented ED-ESEEM pulse technique is by no means limited to the device in this study, but can be applied to a large variety of materials exhibiting spin-dependent charge transport processes. Even fully processed electronic devices can be investigated, which renders ED-ESEEM the method of choice to study other high-end semiconductor devices [137], organic light emitting diodes [138] and solar cells [139] as well as spintronic devices [140]. Applied to these devices, future ED-ESEEM will be capable of providing detailed information about the HFIs and superhyperfine interactions of paramagnetic sites in crystalline or disordered solids. In both cases, the two-pulse ESEEM approach presented in this study can be extended to more advanced ESEEM pulse sequences like Hyperfine Sublevel Correlation Spectroscopy (HYSCORE) to obtain high-resolution spectra to deduce HFI and nuclear quadrupole couplings with all relevant nuclei in the vicinity of the addressed unpaired electron [108, 109].

7 Conclusions and future work

This thesis presents a detailed investigation of the microscopic nature of localized defect states in a-Si:H. It is important to identify the microscopic nature and generation of these defect states since they influence the performance of a-Si:H solar cell devices. Especially a better understanding of the generation of light-induced defects, the SWE, a central point in this thesis, is of high importance, since this effect seriously limits the potential of a-Si:H based solar cells. In order to extent the in-depth study to paramagnetic defects in thin-film solar cells, a novel ED-ESEEM pulse sequence was developed which was applied to investigate unresolved HFIs of defect states in µc-Si:H p-i-n solar cells. In the following the main achievements and results of this thesis are summarized and an outlook for future experiments is given.

7.1 The microscopic nature of native coordination defects in a-Si:H

To provide a complete picture of defects in a-Si:H, a detailed study of native coordination defects in as-deposited a-Si:H was presented in chapter 4. The EPR spectrum of these defects is studied at various microwave frequencies (S-, X-, Q-, and W-Band) to provide a complete resolution of their EPR parameters, the g-tensor and the hyperfine interactions. In contrast to earlier studies, it is found that the coordination defects exhibit a rhombic g-tensor with the following principal values, $g_x = 2.0080$, $g_y = 2.0060$ and $g_z = 2.0033$ and not an axially symmetric g-tensor. The obtained experimental values are compared to those obtained by *ab-initio* DFT calculations of EPR parameters of DB models. The g-tensor principal values and its rhombic symmetry are reasonably well reproduced by theory. However, the experimentally determined hyperfine interaction with ^{29}Si nuclei ($A_{\mathrm{iso}} = 186$ MHz) is significantly smaller than values predicted by theory ($A_{\mathrm{iso}} = -252$

MHz). This indicates that the coordination defects in a-Si:H are more delocalized than one would expect for the case of DB defects. This conclusion is corroborated by a detailed analysis of the line shape of the EPR resonance. The broadening of the central portion of the EPR resonance line at low microwave frequencies is dominated by unresolved hyperfine interactions. This broadening also includes large hyperfine interactions and it is shown that the number of Si atoms with a large hyperfine interaction is about two in the experiment compared to one in case of theoretical models of DB defects. The defect centers in a-Si:H are therefore delocalized over two Si atoms, a microscopic picture which is not in agreement with the presented theoretical study and with an intuitive picture of DB defects located primarily on a single Si atom. The major deviations between experiment and theory of the largest HFI and the broadening function are strong indications that the computer generated DB defects do not adequately represent the coordination defects present in a-Si:H. The real coordination defects are presumably more delocalized. Electronic states of fivefold coordinated Si atoms, so-called floating bonds, were discussed in the literature as an alternative defect model for coordination defects in a-Si:H. Floating bonds are electronic states delocalized over several Si atoms and would be in closer agreement with the presented analysis of the EPR spectrum. However, floating bonds were excluded as an alternative for dangling bonds, since the electronic states are not located in the middle of the band gap but form shallow states closer to the conduction band edge. In conclusion, the coordination defects in a-Si:H are more delocalized than DB defects randomly generated from various a-Si:H models.

7.2 Structural differences between light-induced and native defects in a-Si:H

Following the multifrequency EPR study of native coordination defects in as-deposited a-Si:H, a detailed investigation of light-induced defects showed that the primary-echo decay and the EPR spectrum change after light soaking. A former believe that light-induced defects are identical to native defects with respect to their electronic structure and EPR parameters can therefore be rejected. A detailed analysis of the primary-echo decay of defects showed that the EPR spectrum is composed of two spin species with two different transversal relaxation properties, a spin species with a slow and one with a fast

primary-echo decay. The primary-echo of the slowly decaying electron spins is dominated by nuclear-spin induced spectral diffusion. The origin of the primary-echo decay of the fast decaying light-induced electron spins is yet unidentified.

The different primary-echo decays are utilized to disentangle the highly-overlapping EPR spectra. The EPR spectrum of the slowly decaying electron spins suggests that those defects are identical with native coordination defects. The EPR spectrum of the fast decaying electron spins is narrower and more symmetric than the EPR spectrum of native coordination defects and centered around a slightly smaller g-value. In addition, EPR spectrum of light-induced defects indicates that the g-tensor anisotropy compared to native coordination defects is reduced. Although the difference in the EPR spectra and the primary-echo decay of native and light-induced defects suggests that the electronic structure of the two spins species is different it is rather difficult to speculate about the origin of this deviation. One possible explanation of the reduced g-tensor anisotropy could be a reduction of the anisotropy of the defect wave function. It was discussed that not electronic states of threefold coordinated Si atoms but floating bond states of fivefold coordinated Si atoms are generated by light-soaking [141]. These centers exhibit a much more isotropic wave function and could therefore give rise to the defects observed in the pulse EPR study presented in this work.

Although a definite conclusion about the microscopic origin of the light-induced defects can not be given at this point, the observed differences between the native and light-induced defects provide a serious experimental test for the theoretical models explaining the SWE on a microscopic level. It is obvious that all models which predict that the metastable state is identical to native coordination defects (isolated defects) are in error. A variety of SWE models, however, do not predict isolated defects but defects strongly correlated to H atoms. Whether or not such a correlation could induce the observed changes in the EPR spectrum and transversal relaxation times is difficult to answer at this point. There are at least two ways to test if such a correlation between defects and H atoms exists. One way is a theoretical study of the defects in the various SWE models. If it is possible to produce realistic a-Si:H models with metastable defects as predicted by the various SWE models, a detailed calculation of the EPR parameters by the presented DFT methods could help to test the SWE models in more detail. The other way involves a direct measurement of the H distribution around the defect centers by ENDOR.

We provided a detailed investigation of the H distribution around defects by the ENDOR technique. It is shown by pulsed Davies-ENDOR measurements at Q-Band microwave frequencies that the ENDOR spectra of native coordination defects centered at $\nu_I(^1H)$ are broad and unstructured and indicate the presence of H atoms with HFI up to 30 MHz. This shows that H atoms can be located quite close to the defect center. Earlier investigations of the H distribution around defects by ESEEM [22] indicated that the immediate vicinity of the defect centers (r < 4 Å) is depleted from H atoms. This discrepancy of the results obtained by ESEEM and ENDOR is attributed to the fact that two-pulse ESEEM techniques are subject to deadtime artifacts and are therefore blind to H atoms with a larger HFI. The ENDOR spectra presented here suggest that the H distribution is presumably homogeneous and the immediate vicinity of the defect center is not depleted from H atoms. Applying the ENDOR technique to light soaked a-Si:H sample does not result in substantially different ENDOR spectra. It is shown that various samples in different material state give rise to the same ENDOR spectra. The results obtained by ENDOR do not suggest a spatial correlation between light-induced defects and H atoms. However, it is difficult to conclusively disprove any model accounting for the microscopic mechanism of the SWE by the presented ENDOR measurements since very weak contributions of HFIs due to correlated DB/H states as predicted by the weak Si-Si bond breaking models (cf. sec. 5.1) cannot be observed in the ENDOR experiment at present.

7.3 Development of ED-ESEEM technique for the investigation of defects in thin-film silicon solar cells

The investigation of native and light-induced defects in a-Si:H powder samples by the advanced EPR techniques gave new insight. It is, however, not possible to apply these techniques to fully-processed thin-film solar cells due to the low sensitivity of this method. It was shown that EDMR represents a much more sensitive spectroscopic technique and can be applied to study defects in thin-film solar cells. Pulse EDMR techniques are, however, much less developed compared to conventional pulse EPR due to a number of experimental difficulties. In chapter 6, an implementation of a proof-of-principle ED-ESEEM experiment is presented which is capable of determining small unresolved hyper-

fine interactions of defects in device-grade thin film solar cells. The developed two-pulse ED-ESEEM technique is applied to a device-grade µc-Si:H p-i-n thin film solar cell. The obtained ESEEM spectra are very similar to ESEEM spectra measured with conventional EPR on powder samples. Spectroscopy of e-centers in the phosphorus doped a-Si:H (n) layer of the solar cell shows resonances due to ^{29}Si, ^{31}P and ^{1}H nuclei in the vicinity of the defect states. ESEEM spectra of CE-centers in the intrinsic µc-Si:H absorber layer of the solar cell show only a small residual contribution of ^{31}P and ^{1}H nuclei, which is attributed to an off-resonant excitation of e-centers by the short microwave pulses employed. It is therefore concluded that the CE-centers by themselves do not exhibit resonances in the ESEEM spectrum due to H atoms. Their vicinity is therefore depleted from H. This observation suggests that CE-centers in µc-Si:H are located at the inside of crystalline grains and not at the boundary between the amorphous and the crystalline phases of µc-Si:H.

7.4 Future work

This thesis presented several results which are not in agreement with the established theoretical descriptions of native and light-induced defect states in a-Si:H. Especially the assumption that the dominant defect center in a-Si:H is a DB and the hypothesis that both native and light-induced defects are identical have to be revised. In view of the obtained results, it seems to be mandatory to develop new theoretical approaches for the origin of defects in a-Si:H and the SWE. The following section gives a brief overview of future experiments which can contribute to the field of a-Si:H by obtaining additional experimental facts about the origin of defects and the microscopic processes of the SWE. These results will majorly contribute to a further development of theoretical descriptions of defects in a-Si:H.

In chapter 4 a detailed experimental and theoretical study of coordination defects in as-deposited a-Si:H was presented. This study revealed a rather peculiar discrepancy between the experimentally determined EPR parameters of the present defects and theoretically obtained parameters of computer-generated DB models. There are essentially two points in which theory deviates from the experiment:

1. The largest HFI of the electron spins with nuclear spins of ^{29}Si atoms (experiment: $A_{iso} = 186$ MHz; theory: $A_{iso} = -252$ MHz)

2. The intensity of the HFI satellites and the number of Si atoms with a resolved HFI > 100 MHz (experiment $N \approx 2$, theory $N \approx 1$)

In view of these two important points one can conclude that there seems to be an essential point which is missing in the theoretical DFT study. It is possible that the structural DB models do not represent the real defect structures present in a-Si:H. Another possibility is that the method by which these defects are generated within the a-Si:H computer models is not correct. Clearly, a more extended theoretical DFT study of a wider defect pool needs to be carried out in order to clarify these questions.

The deviation of the satellite intensity of the EPR resonance line can also be addressed by an experimental study. The experimentally determined satellite intensity is larger than the theoretically obtained value, which indicates that the coordination defects exhibit significant spin-density on at least two Si atoms and not only on one Si atom. In order to be sure that the satellite intensity is interpreted correctly, the EPR spectrum needs to be studied in dependence of the ^{29}Si content and the defect concentration N_s of the a-Si:H sample to exclude additional field-independent broadening mechanisms. The ^{29}Si content should be reduced as much as possible by ^{28}Si enrichment. In this case the satellites of the EPR resonance at S- or X-Band microwave frequencies should entirely disappear and the central line should be much narrower. In the limit of zero ^{29}Si content, the EPR resonance line should be determined by unresolved HFI of nearby H atoms. To test if electron-electron spin-spin dipolar broadening contributes in a significant way to the EPR line shape, the EPR spectrum has to be studied as a function of the defect concentration N_s ($N_s < 10^{17}$ cm^{-3} to avoid exchange narrowing). This needs to be tested experimentally, since the dominant broadening mechanism of the EPR resonance line is important for a correct interpretation of the number of Si atoms over which the coordination defects are delocalized.

The EPR spectrum at a ^{29}Si content of 93 % exhibits a doublet structure [73]. Clearly, the observed doublet structure is not in agreement with the presented analysis of the satellite intensity. The doublet structure of the EPR spectrum with a high ^{29}Si content suggests that the spin-density of the defects is concentrated on a single Si atom (one large HFI), while the analysis of the experimental EPR spectrum of a-Si:H with a low ^{29}Si

content indicates that the defect is delocalized over two Si atoms (two large HFIs). It is therefore necessary to reproduce earlier EPR measurements of defects in a-Si:H samples with a large ^{29}Si content. Such studies are on the way in our research groups (B. George, HZB).

A thorough understanding of the microscopic details of native coordination defects in a-Si:H is of course also important for a deeper understanding of the SWE, since it was believed that the light-induced defects and the native defects are identical. Chapter 5 presented a detailed analysis, why this believe has to be rejected. Primary-echo decay measurements of light-induced and native defects by high-field EPR (Q-Band) showed that there are distinct differences in the relaxation properties and the EPR spectrum between these defect species. In order to clarify the origin of the observed differences, additional EPR studies are mandatory. Two experiments are proposed which are important to collect further experimental facts about the observed changes in the relaxation properties and the EPR spectrum

1. Multifrequency EPR study of light-induced defects by two-dimensional primary-echo decay measurements versus external magnetic field

2. Investigation of deuterated a-Si(:D) samples to conclude about the dominating relaxation mechanism of light-induced defects

The first experiment follows the multifrequency approach presented in chapter 4 for native coordination defects, with the slight modification that each EPR spectrum has to be decomposed via the primary-echo decay. It is therefore mandatory to record the full primary-echo decay for each microwave frequency in a two-dimensional experiment. With such a multifrequency study a full resolution of the g-tensor and the HFIs of light-induced defects is possible like in the case of native coordination defects.

Up to now the origin of the fast primary-echo decay of the light-induced defects is unknown. It was speculated that the dominant relaxation mechanism could be spectral diffusion induced by dipolar coupled electron spins or nuclear-spin induced spectral diffusion. In order to test if the latter is the responsible relaxation mechanism, an investigation of deuterated a-Si(:D) samples is necessary. The nuclear-spin induced spectral diffusion depends critically on the g-value of the nuclear spins involved. Hence the effect exhibits a strong isotope dependence and its rate should be reduced in the case of D.

A deeper understanding of the electronic processes in a-Si:H during light illumination will help to understand the microscopic origin of the SWE which is still a major limitation for the potential of thin-film silicon solar cells. Unfortunately, a complete suppression of the SWE seems to be impossible since the effect is an intrinsic property of the material. However, it is possible to control the SWE on a highly sophisticated level since the magnitude of effect of the light degradation depends on the deposition conditions and the structural properties of the employed materials. The magnitude of the SWE and the deposition conditions are related in a fairly complicated way and this is the point where a deeper understanding of the electronic processes and structural changes can help. The potential of thin-film silicon solar cells is therefore not yet fully exploited and this technology can contribute to a sustainable solution of global warming and power generation issues.

Bibliography

[1] Goldemberg, J. ; Johansson, T. B.: *World Energy Assessment Overview, 2004 Update*. New York : United Nations Development Programme, 2004

[2] Jacobson, M. Z.: Review of solutions to global warming, air pollution, and energy security. In: *Energy Environ. Sci.* 2 (2009), p. 148–173

[3] Sawin, J. L. ; Martinot, E.: REN21 - Renewables 2010 Global Status Report. (2010)

[4] EPIA - Solar Generation V - 2008. (2008)

[5] Green, M. A.: Thin-film solar cells: review of materials, technologies and commercial status. In: *J. Mater. Sci.: Mater. Electron.* 18 (2007), p. S15–S19

[6] Shah, A. ; Torres, P. ; Tscharner, R. ; Wyrsch, N. ; Keppner, H.: Photovoltaic technology: The case for thin-film solar cells. In: *Science* 285 (1999), p. 692–698

[7] Green, M. A. ; Emery, K. ; Hishikawa, Y. ; Warta, W.: Solar cell efficiency tables (version 36). In: *Prog. Photovoltaics* 18 (2010), p. 346–352

[8] Staebler, D. L. ; Wronski, C. R.: Reversible Conductivity Changes in Discharge-Produced Amorphous Si. In: *Appl. Phys. Lett.* 31 (1977), p. 292–294

[9] Staebler, D. L. ; Wronski, C. R.: Optically induced conductivity changes in discharge-produced hydrogenated amorphous silicon. In: *J. Appl. Phys.* 51 (1980), p. 3262–3268

[10] Zeman, M. ; Van Elzakker, G. ; Tichelaar, F. D. ; Sutta, P.: Structural properties of amorphous silicon prepared from hydrogen-diluted silane. In: *Philos. Mag.* 89 (2009), p. 2435–2448

[11] Staebler, D. L. ; Crandall, R. S. ; Williams, R.: Stability of *n-i-p* amorphous silicon solar cells. In: *Appl. Phys. Lett.* 39 (1981), p. 733–735

[12] Chaudhuri, P. ; Ray, S. ; Batabyal, A. K. ; Barua, A. K.: Thickness dependence of light-induced effects in a-Si solar cells. In: *Sol. Cells* 31 (1991), p. 13–21

[13] Fritzsche, H.: Development in understanding and controlling the Staebler-Wronski effect in a-Si:H. In: *Annu. Rev. Mater. Res.* 31 (2001), p. 47–79

[14] Dersch, H. ; Stuke, J. ; Beichler, J.: Light-induced dangling bonds in hydrogenated amorphous silicon. In: *Appl. Phys. Lett.* 38 (1981), p. 456–458

[15] Stutzmann, M. ; Jackson, W. B. ; Tsai, C. C.: Light-induced metastable defects in hydrogenated amorphous silicon: A systematic study. In: *Phys. Rev. B* 32 (1985), p. 23–47

[16] Smith, Z. E. ; Wagner, S.: Band Tails, Entropy, and Equilibrium Defects in Hydrogenated Amorphous Silicon. In: *Phys. Rev. Lett.* 59 (1987), p. 688–691

[17] Stutzmann, M.: Weak bond-dangling bond conversion in amorphous silicon. In: *Philos. Mag. B* 56 (1987), p. 63–70

[18] Powell, M. J. ; Deane, S. C.: Improved defect-pool model for charged defects in amorphous silicon. In: *Phys. Rev. B* 48 (1993), p. 10815–10827

[19] Stutzmann, M. ; Biegelsen, D. K.: Microscopic nature of coordination defects in amorphous silicon. In: *Phys. Rev. B* 40 (1989), p. 9834–9840

[20] Stutzmann, M.: Microscopic aspects of the Staebler-Wronski effect. In: *Mater. Res. Soc. Symp. Proc.* 467 (1997), p. 37–48

[21] Schweiger, A. ; Jeschke, G.: *Principles of Pulse Electron Paramagnetic Resonance*. Oxford, UK; New York : Oxford University Press, 2001

[22] Isoya, J. ; Yamasaki, S. ; Okushi, H. ; Matsuda, A. ; Tanaka, K.: Electron-spin-echo envelope-modulation study of the distance between dangling bonds and hydrogen atoms in hydrogenated amorphous silicon. In: *Phys. Rev. B* 47 (1993), p. 7013–7024

[23] Abragam, A. ; Pryce, M. H. L.: Theory of the Nuclear Hyperfine Structure of Paramagnetic Resonance Spectra in Crystals. In: *Proc. R. Soc. London, Ser. A* 205 (1951), p. 135–153

[24] Kneubühl, F. K.: Symmetrie und Mikrowellenspektren mehratomiger paramagnetischer Zentren. In: *Phys. kondens. Mater.* 1 (1963), p. 410 – 447

[25] Stoll, S. ; Schweiger, A.: EasySpin, a comprehensive software package for spectral simulation and analysis in EPR. In: *J. Magn. Res.* 178 (2006), p. 42–55

[26] Stone, A. J.: Gauge invariance of g tensor. In: *Proc. R. Soc. London, Ser. A* 271 (1963), p. 424–434

[27] Davies, E. R.: A New Pulse ENDOR Technique. In: *Phys. Lett. A* 47 A (1974), p. 1–2

[28] Van Vleck, J. H.: Paramagnetic Relaxation Times for Titanium and Chrome Alum. In: *Phys. Rev.* 57 (1940), p. 426–447

[29] Orbach, R.: On the Theory of Spin-Lattice Relaxation in Paramagnetic Salts. In: *Proc. Phys. Soc. London* 77 (1961), p. 821–826

[30] Abragam, A. ; Bleaney, B.: *Electron paramagnetic resonance of transition ions*. New York : Dover Publications, 1986

[31] Castner, T. G.: Raman Spin-Lattice Relaxation of Shallow Donors in Silicon. In: *Phys. Rev.* 130 (1963), p. 58–75

[32] Bowman, M. K. ; Kevan, L.: Electron Spin-Lattice Relaxation Mechanism Involving Tunneling Modes for Trapped Radicals in Glassy Matrices. Theoretical Development and Application to Trapped Electrons in γ-Irradiated Ethanol Glasses. In: *J. Phys. Chem.* 81 (1977), p. 456–461

[33] Carr, H. Y. ; Purcell, E. M.: Effects of Diffusion on Free Precession in Nuclear Magnetic Resonance Experiments. In: *Phys. Rev.* 94 (1954), p. 630–638

[34] Salikhov, K. M. ; Dzuba, S. A. ; Raitsimring, A. M.: The Theory of Electron Spin-Echo Signal Decay Resulting from Dipole-Dipole Interactions between Paramagnetic Centers in Solids. In: *J. Magn. Res.* 42 (1981), p. 255–276

[35] Dzuba, S. A. ; Raitsimring, A. M. ; Tsvetkov, Y. D.: Electron Spin-Echo Studies of Phase Relaxation Kinetics in Systems Containing Two Types of Spins. In: *J. Magn. Res.* 40 (1980), p. 83–89

[36] Salikhov, K. M. ; Semenov, A. G. ; Tsvetkov, Y. D.: *Elektronnoe spinovoe echo i evo primenenie*. Novosibirsk : Izdadelstvo Nauka, 1976

[37] De Sousa, R. ; Das Sarma, S.: Electron spin coherence in semiconductors: Considerations for a spin-based solid-state quantum computer architecture. In: *Phys. Rev. B* 67 (2003), p. 033301

[38] Abe, E. ; Tyryshkin, A. M. ; Tojo, S. ; Morton, J. J. L. ; Witzel, W. M. ; Fujimoto, A. ; Ager, J. W. ; Haller, E. E. ; Isoya, J. ; Lyon, S. A. ; Thewalt, M. L. W. ; Itoh, K. M.: Electron spin coherence of phosphorus donors in silicon: Effect of environmental nuclei. In: *Phys. Rev. B* 82 (2010), p. 121201

[39] McCamey, D. R. ; Huebl, H. ; Brandt, M. S. ; Hutchison, W. D. ; McCallum, J. C. ; Clark, R. G. ; Hamilton, A. R.: Electrically detected magnetic resonance in ion-implanted Si:P nanostructures. In: *Appl. Phys. Lett.* 89 (2006), p. 182115

[40] Kaplan, D. ; Solomon, I. ; Mott, N. F.: Explanation of Large Spin-Dependent Recombination Effect in Semiconductors. In: *J. Phys. (Paris), Lett.* 39 (1978), p. L51–L54

[41] Le Comber, P. G. ; Spear, W. E.: Electronic Transport in Amorphous Silicon Films. In: *Phys. Rev. Lett.* 25 (1970), p. 509–511

[42] Street, R. A.: *Hydrogenated amorphous silicon*. Cambridge ; New York : Cambridge University Press, 1991

[43] Zhou, J. H. ; Baranovskii, S. D. ; Yamasaki, S. ; Ikuta, K. ; Kondo, M. ; Matsuda, A. ; Tanaka, K.: Transport properties of microcrystalline silicon at low temperatures. In: *Semiconductors* 32 (1998), p. 807–811

[44] Stutzmann, M. ; Street, R. A.: Donor States in Hydrogenated Amorphous-Silicon and Germanium. In: *Phys. Rev. Lett.* 54 (1985), p. 1836–1839

[45] Finger, F. ; Müller, J. ; Malten, C. ; Carius, R. ; Wagner, H.: Electronic properties of microcrystalline silicon investigated by electron spin resonance and transport measurements. In: *J. Non-Cryst. Solids* 266-269 (2000), p. 511–518

[46] Stutzmann, M. ; Brandt, M. S. ; Bayerl, M. W.: Spin-dependent processes in amorphous and microcrystalline silicon: a survey. In: *J. Non-Cryst. Solids* 266-269 (2000), p. 1–22

[47] Eickelkamp, T. ; Roth, S. ; Mehring, M.: Electrically detected magnetic resonance in photoexcited fullerenes. In: *Mol. Phys.* 95 (1998), p. 967–972

[48] Sorensen, O. W. ; Eich, G. W. ; Levitt, M. H. ; Bodenhausen, G. ; Ernst, R. R.: Product Operator Formalism for the Description of NMR Pulse Experiments. In: *Prog. Nucl. Magn. Reson. Spectrosc.* 16 (1983), p. 163–192

[49] Boehme, C. ; Lips, K.: The investigation of charge carrier recombination and hopping transport with pulsed electrically detected magnetic resonance techniques. In: *Charge transport in disordered solids with applications in electronics*. Wiley, 2006

[50] Behrends, J. ; Schnegg, A. ; Fehr, M. ; Lambertz, A. ; Haas, S. ; Finger, F. ; Rech, B. ; Lips, K.: Electrical Detection of Electron Spin Resonance in Microcrystalline Silicon pin Solar Cells. In: *Philos. Mag.* 89 (2009), p. 2655–2676

[51] Herring, T. W. ; Lee, S. Y. ; McCamey, D. R. ; Taylor, P. C. ; Lips, K. ; Hu, J. ; Zhu, F. ; Madan, A. ; Boehme, C.: Experimental discrimination of geminate and non-geminate recombination in a-Si:H. In: *Phys. Rev. B* 79 (2009), p. 195205

[52] Schropp, R. E. I. ; Zeman, M.: *Amorphous and Microcrystalline Silicon Solar Cells: Modeling, Materials and Device Technology*. Berlin; New York : Springer, 1998

[53] Rech, B. ; Wagner, H.: Potential of amorphous silicon for solar cells. In: *Appl. Phys. A* 69 (1999), p. 155–167

[54] Astakhov, O. ; Carius, R. ; Finger, F. ; Petrusenko, Y. ; Borysenko, V. ; Barankov, D.: Relationship between defect density and charge carrier transport in amorphous and microcrystalline silicon. In: *Phys. Rev. B* 79 (2009), p. 104205

[55] Alpuim, P. ; Chu, V. ; Conde, J. P.: Amorphous and microcrystalline silicon films grown at low temperatures by radio-frequency and hot-wire chemical vapor deposition. In: *J. Appl. Phys.* 86 (1999), p. 3812–3821

[56] Simon, P.: *Quantitative Defektdichtemessungen mittels Elektronenspinresonanz (ESR) an polykristallinen Silizium-Dünnschichtsolarzellen*, Rheinisch-Westfälische Technische Hochschule Aachen, Diplomarbeit, 2010

[57] Rech, B. ; Roschek, T. ; Repmann, T. ; Müller, J. ; Schmitz, R. ; Appenzeller, W.: Microcrystalline silicon for large area thin film solar cells. In: *Thin Solid Films* 427 (2003), p. 157–165

[58] Vetterl, O. ; Finger, F. ; Carius, R. ; Hapke, P. ; Houben, L. ; Kluth, O. ; Lambertz, A. ; Mück, A. ; Rech, B. ; Wagner, H.: Intrinsic microcrystalline silicon: A new material for photovoltaics. In: *Sol. Energy Mat. Sol. Cells* 62 (2000), p. 97–108

[59] Stoll, S. ; Kasumaj, B.: Phase Cycling in Electron Spin Echo Envelope Modulation. In: *Appl. Magn. Res.* 35 (2008), p. 15–32

[60] Brüggemann, W. ; Niklas, J. R.: Stochastic ENDOR. In: *J. Magn. Reson. A* 108 (1994), p. 25–29

[61] Epel, B. ; Arieli, D. ; Baute, D. ; Goldfarb, D.: Improving W-band pulsed ENDOR sensitivity - random acquisition and pulsed special TRIPLE. In: *J. Magn. Res.* 164 (2003), p. 78–83

[62] Giannozzi, P. ; Baroni, S. ; Bonini, N. ; Calandra, M. ; Car, R. ; Cavazzoni, C. ; Ceresoli, D. ; Chiarotti, G. L. ; Cococcioni, M. ; Dabo, I. ; Dal Corso, A. ; De Gironcoli, S. ; Fabris, S. ; Fratesi, G. ; Gebauer, R. ; Gerstmann, U. ; Gougoussis, C. ; Kokalj, A. ; Lazzeri, M. ; Martin-Samos, L. ; Marzari, N. ; Mauri, F. ; Mazzarello, R. ; Paolini, S. ; Pasquarello, A. ; Paulatto, L. ; Sbraccia, C. ; Scandolo, S. ; Sclauzero, G. ; Seitsonen, A. P. ; Smogunov, A. ; Umari, P. ; Wentzcovitch, R. M.: QUANTUM ESPRESSO: a modular and open-source software project for quantum simulations of materials. In: *J. Phys.: Condens. Matter* 21 (2009), p. 395502

[63] Van De Walle, C. G. ; Blöchl, P. E.: First-Principles Calculations of Hyperfine Parameters. In: *Phys. Rev. B* 47 (1993), p. 4244–4255

[64] Pickard, C. J. ; Mauri, F.: First-principles theory of the EPR g tensor in solids: Defects in quartz. In: *Phys. Rev. Lett.* 88 (2002), p. 086403

[65] Biswas, P. ; Tafen, D. N. ; Inam, F. ; Cai, B. ; Drabold, D. A.: Materials modeling by design: applications to amorphous solids. In: *J. Phys.: Condens. Matter* 21 (2009), p. 084207

[66] Jarolimek, K. ; De Groot, R. A. ; De Wijs, G. A. ; Zeman, M.: First-principles study of hydrogenated amorphous silicon. In: *Phys. Rev. B* 79 (2009), p. 155206

[67] Stutzmann, M.: The defect density in amorphous silicon. In: *Philos. Mag. B* 60 (1989), p. 531–546

[68] Pantelides, S. T.: Defects in Amorphous Silicon: A New Perspective. In: *Phys. Rev. Lett.* 57 (1986), p. 2979–2982

[69] Poindexter, E. H. ; Caplan, P. J. ; Deal, B. E. ; Razouk, R. R.: Interface states and electron spin resonance centers in thermally oxidized (111) and (100) silicon wafers. In: *J. Appl. Phys.* 52 (1981), p. 879–884

[70] Cook, M. ; White, C. T.: Hyperfine interactions in cluster models of the P_b defect center. In: *Phys. Rev. B* 38 (1988), p. 9674–9685

[71] Umeda, T. ; Yamasaki, S. ; Isoya, J. ; Tanaka, K.: Electron-spin-resonance center of dangling bonds in undoped a-Si:H. In: *Phys. Rev. B* 59 (1999), p. 4849–4857

[72] Watkins, G. D. ; Corbett, J. W.: Defects in Irradiated Silicon: Electron Paramagnetic Resonance and Electron-Nuclear Double Resonance of Si-E Center. In: *Phys. Rev.* 134 (1964), p. A1359–A1377

[73] Biegelsen, D. K. ; Stutzmann, M.: Hyperfine Studies of Dangling Bonds in Amorphous Silicon. In: *Phys. Rev. B* 33 (1986), p. 3006–3011

[74] Brower, K. L.: ^{29}Si hyperfine structure of unpaired spins at the Si/SiO_2 interface. In: *Appl. Phys. Lett.* 43 (1983), p. 1111–1113

[75] Gerstmann, U. ; Rohrmüller, M. ; Mauri, F. ; Schmidt, W. G.: *Ab initio g*-tensor calculation for paramagnetic surface states: hydrogen adsorption at Si surfaces. In: *phys. stat. sol. (c)* 7 (2010), p. 157–160

[76] Wu, Y. ; Stesmans, A.: Nature of paramagnetic centers in a-Si and a-Si:H. In: *Phys. Rev. B* 38 (1988), p. 2779–2786

[77] Brandt, M. S. ; Bayerl, M. W. ; Stutzmann, M. ; Graeff, C. F. O.: Electrically detected magnetic resonance of a-Si:H at low magnetic fields: the influence of hydrogen on the dangling bond resonance. In: *J. Non-Cryst. Solids* 227-230 (1998), p. 343–347

[78] Weil, J. A.: The simulation of EPR spectra: A mini-review. In: *Mol. Phys. Rep.* 26 (1999), p. 11–24

[79] Van Vleck, J. H.: The Dipolar Broadening of Magnetic Resonance Lines in Crystals. In: *Phys. Rev.* 74 (1948), p. 1168–1183

[80] Kittel, C. ; Abrahams, E.: Dipolar Broadening of Magnetic Resonance Lines in Magnetically Diluted Crystals. In: *Phys. Rev.* 90 (1953), p. 238–239

[81] Wyard, S. J.: The Dipolar Broadening of Electron Spin Resonance Lines in Irradiated Solids. In: *Proc. Phys. Soc. London* 86 (1965), p. 587–593

[82] Stutzmann, M. ; Biegelsen, D. K.: Electron-spin-lattice relaxation in amorphous silicon and germanium. In: *Phys. Rev. B* 28 (1983), p. 6256–6261

[83] Fedders, P. A. ; Carlsson, A. E.: Defect States at Floating and Dangling Bonds in Amorphous Si. In: *Phys. Rev. B* 37 (1988), p. 8506–8508

[84] Biswas, R. ; Wang, C. Z. ; Chan, C. T. ; Ho, K. M. ; Soukoulis, C. M.: Electronic structure of dangling and floating bonds in amorphous silicon. In: *Phys. Rev. Lett.* 63 (1989), p. 1491

[85] Fedders, P. A. ; Carlsson, A. E.: Energy Levels and Charge Distributions of Nonideal Dangling and Floating Bonds in Amorphous Si. In: *Phys. Rev. B* 39 (1989), p. 1134–1139

[86] Ishii, N. ; Shimizu, T.: Origin of the ESR signal with $g = 2.0055$ in amorphous silicon. In: *Phys. Rev. B* 42 (1990), p. 9697–9700

[87] Kamei, T. ; Hata, N. ; Matsuda, A. ; Uchiyama, T. ; Amano, S. ; Tsukamoto, K. ; Yoshioka, Y. ; Hirao, T.: Deposition and extensive light soaking of highly pure hydrogenated amorphous silicon. In: *Appl. Phys. Lett.* 68 (1996), p. 2380–2382

[88] Stutzmann, M. ; Jackson, W. B. ; Tsai, C. C.: Annealing of metastable defects in hydrogenated amorphous silicon. In: *Phys. Rev. B* 34 (1986), p. 63–72

[89] Bachus, R. ; Movaghar, B. ; Schweitzer, L. ; Voget-Grote, U.: The influence of the exchange interaction on the E.S.R. linewidth in amorphous silicon. In: *Philos. Mag. B* 39 (1979), p. 27–37

[90] Yamasaki, S. ; Kaneiwa, M. ; Kuroda, S. ; Okushi, H. ; Tanaka, K.: ^{1}H electron-nuclear-double-resonance-detected ESR of light-soaked undoped a-Si:H. In: *Phys. Rev. B* 35 (1987), p. 6471–6474

[91] Morigaki, K.: Microscopic Mechanism for the Photo-Creation of Dangling Bonds in a-Si:H. In: *Jpn. J. Appl. Phys.* 27 (1988), p. 163–168

[92] Jackson, W. B.: Role of hydrogen complexes in the metastability of hydrogenated amorphous silicon. In: *Phys. Rev. B* 41 (1990), p. 10257–10260

[93] Zhang, S. B. ; Jackson, W. B. ; Chadi, D. J.: Diatomic-Hydrogen-Complex Dissociation: A Microscopic Model for Metastable Defect Generation in Si. In: *Phys. Rev. Lett.* 65 (1990), p. 2575–2578

[94] Powell, M. J. ; Deane, S. C. ; Wehrspohn, R. B.: Microscopic mechanisms for creation and removal of metastable dangling bonds in hydrogenated amorphous silicon. In: *Phys. Rev. B* 66 (2002), p. 155212

[95] Stutzmann, M. ; Jackson, W. B. ; Smith, A. J. ; Thompson, R.: Light-induced metastable defects in amorphous silicon: The role of hydrogen. In: *Appl. Phys. Lett.* 48 (1986), p. 62–64

[96] Branz, H. M.: Hydrogen collision model: Quantitative description of metastability in amorphous silicon. In: *Phys. Rev. B* 59 (1999), p. 5498–5512

[97] Adler, D.: Origin of the Photo-Induced Changes in Hydrogenated Amorphous Silicon. In: *Sol. Cells* 9 (1983), p. 133–148

[98] Stutzmann, M.: Metastable changes of the electronic spin-lattice relaxation-time in hydrogenated amorphous silicon. In: *Phys. Rev. B* 33 (1986), p. 7379–7382

[99] Isoya, J. ; Yamasaki, S. ; Matsuda, A. ; Tanaka, K.: Time-domain measurements of spin relaxation processes of dangling-bond defects in hydrogenated amorphous silicon. In: *Philos. Mag. B* 69 (1994), p. 263–275

[100] Millhauser, G. L. ; Freed, J. H.: Two-dimensional electron spin echo spectroscopy and slow motions. In: *J. Chem. Phys.* 81 (1984), p. 37–48

[101] Konda, R. ; Du, J.-L. ; Eaton, S. S. ; Eaton, G. R.: Electron Spin Relaxation Rates for Nitridochromium(V) Tetratolylporphyrin and Nitridochromium(V) Octaethylporphyrin in Frozen Solution. In: *Appl. Magn. Res.* 7 (1994), p. 185–193

[102] Kirilina, E. P. ; Prisner, T. F. ; Bennati, M. ; Endeward, B. ; Dzuba, S. A. ; Fuchs, M. R. ; Möbius, K. ; Schnegg, A.: Molecular dynamics of nitroxides in glasses as studied by multi-frequency EPR. In: *Magn. Reson. Chem.* 43 (2005), p. S119–S129

[103] Ferretti, A. ; Fanciulli, M. ; Ponti, A. ; Schweiger, A.: Electron spin-echo relaxation and envelope modulation of shallow phosphorus donors in silicon. In: *Phys. Rev. B* 72 (2005), p. 235201

[104] Yamasaki, S. ; Isoya, J.: Microscopic Structure of Dangling Bonds in Undoped Hydrogenated Amorphous Silicon Investigated by Pulsed ESR. In: *Optoelectron. Dev. Technol.* 9 (1994), p. 345–354

[105] Raitsimring, A. M. ; Salikhov, K. M. ; Umanskii, B. A. ; Tsvetkov, Y. D.: Instantaneous Diffusion in Electron-Spin Echo of Paramagnetic Centers Stabilized in Solid Matrices. In: *Fiz. Tverd. Tela* 16 (1974), p. 756–766

[106] Nonomura, S. ; Yoshida, N. ; Gotoh, T. ; Sakamoto, T. ; Matsuda, A. ; Nitta, S.: The light-induced metastable lattice expansion in hydrogenated amorphous silicon. In: *J. Non-Cryst. Solids* 266-269 (2000), p. 474–480

[107] Hudgens, S. J.: Low-temperature magnetic properties of amorphous germanium and silicon. In: *Phys. Rev. B* 14 (1976), p. 1547–1556

[108] Höfer, P.: Distortion-Free Electron-Spin-Echo Envelope-Modulation Spectra of Disordered Solids Obtained from Two- and Three-Dimensional HYSCORE Experiments. In: *J. Magn. Reson. A* 111 (1994), p. 77–86

[109] Höfer, P. ; Grupp, A. ; Nebenführ, H. ; Mehring, M.: Hyperfine Sublevel Correlation (HYSCORE) Spectroscopy: A 2D ESR Investigation of the Squaric Acid Radical. In: *Chem. Phys. Lett.* 132 (1986), p. 279–282

[110] Hyde, J. S. ; Rist, G. H. ; Eriksson, L. E.: ENDOR of Methyl, Matrix, and α Protons in Amorphous and Polycrystalline Matrices. In: *J. Phys. Chem.* 72 (1968), p. 4269–4276

[111] Stutzmann, M. ; Biegelsen, D. K.: Electron-nuclear double-resonance experiments in hydrogenated amorphous silicon. In: *Phys. Rev. B* 34 (1986), p. 3093–3107

[112] Yokomichi, H. ; Morigaki, K.: Electron-Nuclear Double Resonance of Dangling-Bond Centres Associated with Hydrogen Incorporation in a-Si:H. In: *Solid State Commun.* 63 (1987), p. 629–632

[113] Fan, C. ; Doan, P. E. ; Davoust, C. E. ; Hoffman, B. M.: Quantitative Studies of Davies Pulsed ENDOR. In: *J. Magn. Res.* 98 (1992), p. 62–72

[114] Gemperle, C. ; Schweiger, A.: Pulsed Electron-Nuclear Double Resonance Methodology. In: *Chem. Rev.* 91 (1991), p. 1481–1505

[115] Astashkin, A. V. ; Kawamori, A.: Matrix line in pulsed electron-nuclear double resonance spectra. In: *J. Magn. Res.* 135 (1998), p. 406–417

[116] Van Zee, R. J. ; Ferrante, R. F. ; Weltner, W.: Si_2, SiH_3, and HSiO molecules: ESR at 4 K. In: *J. Chem. Phys.* 83 (1985), p. 6181–6187

[117] Ishii, N. ; Kumeda, M. ; Shimizu, T.: The Effects of H and F on the ESR Signals in a-Si. In: *Jpn. J. Appl. Phys.* 21 (1982), p. L92–L94

[118] Lepine, D. J.: Spin-Dependent Recombination on Silicon Surface. In: *Phys. Rev. B* 6 (1972), p. 436–441

[119] Boehme, C. ; Lips, K.: Theory of time-domain measurement of spin-dependent recombination with pulsed electrically detected magnetic resonance. In: *Phys. Rev. B* 68 (2003), p. 245105

[120] Hoehne, F. ; Huebl, H. ; Galler, B. ; Stutzmann, M. ; Brandt, M. S.: Spin-Dependent Recombination between Phosphorus Donors in Silicon and Si/SiO_2 Interface States Investigated with Pulsed Electrically Detected Electron Double Resonance. In: *Phys. Rev. Lett.* 104 (2010), p. 046402

[121] Boehme, C. ; Lips, K.: Electrical detection of spin coherence in silicon. In: *Phys. Rev. Lett.* 91 (2003), p. 246603

[122] Huebl, H. ; Hoehne, F. ; Grolik, B. ; Stegner, A. R. ; Stutzmann, M. ; Brandt, M. S.: Spin echoes in the charge transport through phosphorus donors in silicon. In: *Phys. Rev. Lett.* 100 (2008), p. 177602

[123] Paik, S.-Y. ; Lee, S.-Y. ; Baker, W. J. ; McCamey, D. R. ; Boehme, C.: T_1 and T_2 spin relaxation time limitations of phosphorous donor electrons near crystalline silicon to silicon dioxide interface defects. In: *Phys. Rev. B* 81 (2010), p. 075214

[124] McCamey, D. R. ; Van Tol, J. ; Morley, G. W. ; Boehme, C.: Electronic Spin Storage in an Electrically Readable Nuclear Spin Memory with a Lifetime > 100 Seconds. In: *Science* 330 (2010), p. 1652–1656

[125] Hoehne, F. ; Dreher, L. ; Huebl, H. ; Stutzmann, M. ; Brandt, M. S.: Electrical Detection of Coherent Nuclear Spin Oscillations in Phosphorus-Doped Silicon using Pulsed ENDOR. In: *Phys. Rev. Lett.* 106 (2011), p. 187601

[126] Behrends, J. ; Schnegg, A. ; Boehme, C. ; Haas, S. ; Stiebig, H. ; Finger, F. ; Rech, B. ; Lips, K.: Recombination and transport in microcrystalline pin solar cells studied with pulsed electrically detected magnetic resonance. In: *J. Non-Cryst. Solids* 354 (2008), p. 2411–2415

[127] Lips, K. ; Fuhs, W.: Transport and recombination in amorphous *p-i-n*-type solar cells studied by electrically detected magnetic resonance. In: *J. Appl. Phys.* 74 (1993), p. 3993–3999

[128] Spaeth, J.-M. ; Overhof, H.: *Point defects in semiconductors and insulators*. Berlin ; New York : Springer, 2003

[129] Stich, B. ; Greulich-Weber, S. ; Spaeth, J.-M.: Electrical detection of electron nuclear double resonance in silicon. In: *Appl. Phys. Lett.* 68 (1996), p. 1102–1104

[130] Haberkorn, R. ; Dietz, W.: Theory of Spin-Dependent Recombination in Semiconductors. In: *Solid State Commun.* 35 (1980), p. 505–508

[131] Maudsley, A. A. ; Wokaun, A. ; Ernst, R. R.: Coherence Transfer Echoes. In: *Chem. Phys. Lett.* 55 (1978), p. 9–14

[132] Ponti, A. ; Schweiger, A.: Nuclear coherence-transfer echoes in pulsed EPR. In: *J. Chem. Phys.* 102 (1995), p. 5207–5219

[133] Mims, W. B.: Envelope Modulation in Spin-Echo Experiments. In: *Phys. Rev. B* 5 (1972), p. 2409–2419

[134] Ponti, A. ; Schweiger, A.: Echo Phenomena in Electron Paramagnetic Resonance Spectroscopy. In: *Appl. Magn. Res.* 7 (1994), p. 363–403

[135] Schweiger, A. ; Gemperle, C. ; Ernst, R. R.: Soft Pulse Electron-Spin-Echo-Envelope Modulation Spectroscopy (Soft ESEEM). In: *J. Magn. Res.* 86 (1990), p. 70–81

[136] Yamasaki, S. ; Lee, J. ; Umeda, T. ; Isoya, J. ; Tanaka, K.: Spatial distribution of phosphorus atoms surrounding spin centers of P-doped hydrogenated amorphous silicon elucidated by pulsed ESR. In: *J. Non-Cryst. Solids* 198-200 (1996), p. 330–333

[137] Kawachi, G. ; Graeff, C. F. O. ; Brandt, M. S. ; Stutzmann, M.: Carrier transport in amorphous silicon-based thin-film transistors studied by spin-dependent transport. In: *Phys. Rev. B* 54 (1996), p. 7957–7964

[138] McCamey, D. R. ; Seipel, H. A. ; Paik, S.-Y. ; Walter, M. J. ; Borys, N. J. ; Lupton, J. M. ; Boehme, C.: Spin Rabi flopping in the photocurrent of a polymer light-emitting diode. In: *Nature Mater.* 7 (2008), p. 723–728

[139] Behrends, J. ; Schnegg, A. ; Lips, K. ; Thomsen, E. A. ; Pandey, A. K. ; Samuel, I. D. W. ; Keeble, D. J.: Bipolaron Formation in Organic Solar Cells Observed by Pulsed Electrically Detected Magnetic Resonance. In: *Phys. Rev. Lett.* 105 (2010), p. 176601

[140] Oh, D. K. ; Lee, C. E. ; Lee, J.-H. ; Rhie, K.: Evidence of electron-spin wave coupling in Co_xNb_y magnetic metal thin film. In: *J. Magn. Magn. Mater.* 293 (2005), p. 880–884

[141] Pantelides, S. T.: Defect dynamics and the Staebler-Wronski effect in hydrogenated amorphous silicon. In: *Phys. Rev. B* 36 (1987), p. 3479–3482

List of publications

1. Behrends, J. ; Schnegg, A. ; Fehr, M. ; Lambertz, A. ; Haas, S. ; Finger, F. ; Rech, B. ; Lips, K.: Electrical Detection of Electron Spin Resonance in Microcrystalline Silicon pin Solar Cells. In: Philos. Mag. 89 (2009), p. 2655 - 2676

2. Fehr, M. ; Schnegg, A. ; Rech, B. ; Lips, K. ; Finger, F. ; Astakhov, O. ; Teutloff, C. ; Bittl, R.: Hydrogen distribution in the vicinity of dangling bonds in hydrogenated amorphous silicon (a-Si:H). In: phys. stat. sol. (a) 207 (2010), p. 552 - 555

3. Lips, K. ; Fehr, M. ; Behrends, J.: Electron-Spin Resonance (ESR) in Hydrogenated Amorphous Silicon (a-Si:H). In: Advanced Characterization Techniques for Thin-Film Solar Cells, Wiley-VCH, Berlin, (2011)

4. Fehr, M. ; Schnegg, A. ; Rech, B. ; Lips, K. ; Finger, F. ; Astakhov, O. ; Pfanner, G. ; Freysoldt, C. ; Neugebauer, J. ; Bittl, R. ; Teutloff, C.: Dangling bonds in a-Si:H revisited: A combined Multifrequency EPR and DFT Study. submitted to Physical Review B

5. Fehr, M. ; Behrends, J. ; Haas, S. ; Rech, B. ; Lips, K. ; Schnegg, A.: Electrical detection of electron-spin-echo envelope modulations in thin-film silicon solar cells. submitted to Physical Review B

Acknowledgments

Zu guter Letzt, möchte ich mich bei allen bedanken die beim Anfertigen der Arbeit auf die vielfältigste Weise mitgeholfen haben:

Dr. Klaus Lips für die Einladung zu dieser Arbeit nach Berlin, die großzügige Investition seiner Zeit in die Betreuung und Verbesserung meines Vortragsstils und sein Vertrauen in mich welches es mir ermöglichte manche Angelegenheiten selbstständig anzugehen.

Dr. Alexander Schnegg für die intensive Betreuung meiner Arbeit und seine unendliche Geduld bei der Korrektur meiner Manuskripte. Vielen Dank für die nette und unkomplizierte Zusammenarbeit.

Dr. Christian Teutloff für so viel! Du hast einen sehr großen Anteil an dieser Arbeit, von der Einführung in die komplizierteren EPR Techniken über die Reparatur und Wartung von Resonatoren und Spektrometern bis hin zu eigenständigen EPR Messungen und zähen Verhandlung mit Koautoren.

Prof. Dr. Robert Bittl für die vielen Diskussionen, Grillpartys und die Möglichkeit EPR Experimente in der AG Bittl durchzuführen sowie die Chance an der FU Berlin zu promovieren

Prof. Dr. Bernd Rech für viele Diskussionen, seine Unterstützung und Offenheit und für Einblicke in die Details der Depositionstechniken von Dünnschichtsolarzellen.

Dr. Jan Behrends für so viele Dinge, das würde hier den Rahmen sprengen. Unsere Zusammenarbeit hat mir den Einstieg in die EPR und EDMR Messungen sehr erleichtert. Dein Beitrag zur Weiterentwicklung der EDMR Techniken in Adlershof hat die Messungen dieser Arbeit erst ermöglicht.

Dr. Friedhelm Finger, Dr. Oleksandr Astakhov, Andreas Lambertz und Stefan Haas vom Forschungszentrum Jülich für die Herstellung der a-Si:H Pulverproben und μc-Si:H Solarzellen für EPR- und EDMR-Untersuchungen.

Dr. Christoph Freysoldt und Gernot Pfanner für viele Diskussionen, die Bereitstellung von DFT Rechnungen und die Zusammenarbeit bei der Analyse von Defektzentren in a-Si:H

Dr. Fakhar Inam and Prof. Dave Drabold as well as Karol Jarolimek for providing atomistic DB model structures used in the theoretical calculations

Prof. Dr. Martin Brandt und Prof. Dr. Martin Stutzmann, Konrad Klein und Felix Hoehne vom Walter Schottky Institut für viele spannende Diskussionen, Anregungen und die Zusammenarbeit innerhalb des EPR-Solar Projekts.

Prof. Dr. Christian Jäger und Alexandra Huber von der BAM für MAS ^{1}H-NMR Messungen an a-Si:H

Allen Mitarbeitern und Doktoranden der AG Bittl für die kollegiale Atmosphäre und die Unterstützung bei der Durchführung von EPR Experimenten

Allen Mitarbeitern des Instituts für Silizium-Photovoltaik für die nette Arbeitsatmosphäre. Meinen ehemaligen Bürokollegen und Mitdoktoranden Benjamin George, Peter Simon, Dr. Marc-Andy Gluba, Dr. Felice Friedrich, Lars-Peter Scheller, Tim Schulze, Caspar Leendertz, Mark Wimmer, Dr. Jerome Tribollet, Dr. Yuri Ryabchikov, Ivan Pentegov und Dr. Benjamin Gorka für die tolle Zeit auch außerhalb des Instituts

Dr. Franke (Elektronik-Manufaktur Mahlsdorf) für seine hochentwickelten Messgeräte, die wesentlich zur Verbesserung unserer EDMR Techniken beigetragen haben.

Marion Krusche für die Hilfe bei bürokratischen Problemen. Dr. Bernhard Namaschk, Thomas Lußky, Thorsten Seefeldt und Andreas von Kozierowski für Hilfe in technischen Dingen.

Peter Höfer, Antoine Wolff und Igor Gromov von der Firma Bruker für Unterstützung und Beratung bei der Wartung und beim Neuaufbau von EPR Spektrometern

Dr. Jens Törring für die Installation und Wartung seines Steuerprogramms für EPR Spektrometer

Dr. Evgeniya Kirilina für Diskussionen zu Details der Spinrelaxation.

Dr. Friedhelm Lendzian für die Entwicklung eines Q-Band Probenkopfes für Puls-EPR und Puls-ENDOR Anwendungen

Meinen Eltern und meinen Geschwistern für ihre Unterstützung und die liebevolle Aufbauarbeit.

Erklärung

„Ich erkläre ehrenwörtlich, dass ich die dem Fachbereich Physik der Freien Universität Berlin zur Promotionsprüfung eingereichte Arbeit ohne sonstige Hilfe selbst durchgeführt und bei der Abfassung der Arbeit keine anderen als die in der Dissertation aufgeführten Hilfsmittel benutzt habe."

_____

Ort, Datum, Unterschrift